Universitat Politècnica de València

Electrical and Anatomical Modeling of the Specialized Cardiac Conduction System. A Simulation Study.

PREDOCTORAL RESEARCH THESIS

Biomedical Engineering

PhD Program in Health and Welfare

LYDIA DUX-SANTOY HURTADO

Director:

Dr. Jose M. Ferrero de Loma-Osorio

Co-director:

Dr. Rafael Sebastián Aguilar

Grupo de Bioelectrónica-I3BH

Universitat Politècnica de València

March 2011

“Ego quid sciam quaero, non quid credam”

Yo investigo para saber algo, no para pensarlo

San Agustín, *Soliloquia, I, III., 8*

TABLE OF CONTENTS

TABLE OF FIGURES

ACRONYMS

AP	Action potential
APD	Action potential duration
AVN	Atrio-ventricular node
BCL	Basic Cycle length
CCS	Cardiac conduction system
D	Dofetilide concentration
ECG	Electrocardiogram
HB	Bundle of His
LBB	Left bundle branch
LBBB	Left bundle branch block
LV	Left ventricle
PK	Purkinje
PMJ	Purkinje-myocardial junction
RBB	Right bundle branch
RV	Right ventricle
SAN	Sino-atrial node

1. INTRODUCTION

A- MOTIVATION AND AIMS

The specialized electrical cardiac conduction system orchestrates and initiates the excitation-contraction process of the heart ventricles. The impulse originates in the SAN, the natural pacemaker, located in the right atrium of the heart. From the SAN it propagates to the AVN, which electrically connects atrial and ventricular chambers. The AVN delays impulses. This is extremely important since it ensures that the atria have ejected their blood into the ventricles before the ventricles contract. The electrical impulse continues through the HB, which is a collection of heart muscle cells specialized for electrical conduction that transmits the impulses from the AVN to the fascicular branches. The fascicular branches then lead to the PK fibers which innervate the ventricles, causing the cardiac muscle of the ventricles to contract at a paced interval. The bulk myocardium is electrically activated at PMJ, which are scattered over the endocardial surface. Figure 1 shows a simplified representation of the electrical conduction system of the heart.

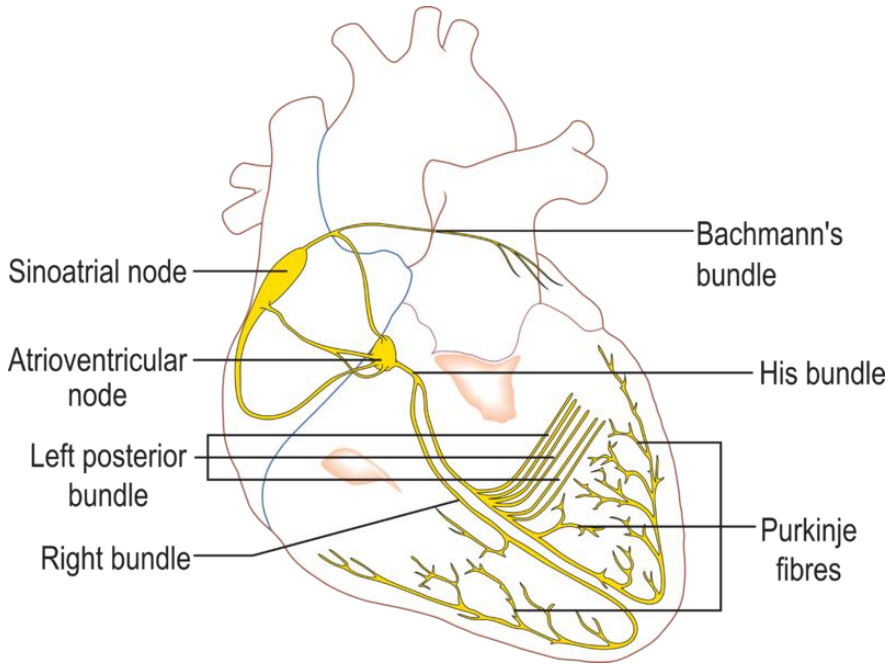

Figure 1. A graphical representation of the electrical conduction system of the heart showing the Sinoatrial node, Atrioventricular node, HB, PK fibers, and Bachmann's bundle.

The distal regions of the CCS and in particular the PK network structure are fundamental to ensure a normal sequence of cardiac activation and subsequent contraction. Nonetheless, there are many cardiac disorders and pathologies such as arrhythmias, fibrillation, or tachycardia which might result from abnormalities in one of the sections of the CCS. One important example is LBBB, a cardiac conduction abnormality seen on the ECG. In this condition, activation of the LV is delayed, which results in the LV contracting

after the RV, and a decrease the cardiac ejection. Other important negative effects of abnormal activation of the CCS are the generation of electrical macro or micro re-entries. This type of reentry is due to a unidirectional block in the CCS and can give rise to ventricular tachycardia. Another source of problems might originate from the PK system itself, which has been reported to produce subendocardial focal activity i.e. early after-depolarizations (EADs) and delayed after-depolarizations (DADs), or microreentry under certain conditions.

Although the role of the CCS in the normal electrical sequence of activation is well known, its functioning in abnormal conditions, or its interaction with electrical disorders which have their origin in other pathologies, such as infarctions, is not well understood yet. In order to better understand the underlying mechanisms that lead to certain types of arrhythmia, it is crucial to look for new tools that allow studying in detail the electrical coupling of the CCS and the myocardium under normal and pathological conditions in an easy way.

ICT tools and integrative multi-scale computational models of the heart may help to improve understanding, diagnosis, treatment planning and interventions for cardio vascular disease. Biophysical models of cardiac electrophysiology are available at different scales and are able to reproduce the electrical activation and propagation in cardiac soft tissues. The opportunity of multi-scale modeling spanning multiple anatomical levels (sub-cellular level up to whole heart) is to provide a consistent, biophysically-based framework for the integration of the huge amount of fragmented and inhomogeneous data currently available. The combination of biophysical and patient-specific anatomical models of atria and ventricles allows simulating cardiac electrical activations for a given patient and has the potential for helping in decision taking processes for electrical therapies such as cardiac resynchronization therapy or radio-frequency ablation.

One of the main drawbacks of current cardiac models is the impossibility of obtaining patient-specific data for all the anatomical components that take part in the electrical activation of the heart. Among them the CCS has remained largely elusive due to the difficulty to observe it *in-vivo* and the little amount of information available in the literature. As a result, the CCS is often not modeled in computational models or is oversimplified. Among the most common approaches followed to avoid explicitly modeling the PK system, though still synchronously activating the ventricles, is the use of excitation points. In this approach, a set of discrete scattered excitation points is placed all over the endocardium. Following the measurements from *ex-vivo* electrical mapping studies, such as Durrer [1] the points are activated, as small pacemakers, creating a virtual activation map. More sophisticated approaches build simplistic PK trees that define the locations of the PMJs based on electrical landmarks [2, 3]. Although simple geometrical models allow including specific PK cellular models and PMJs, none of them tried to reproduce the pattern or structure of the PK system, or its complexity.

In this study we present a framework that allows generating the peripheral section of the CCS for a given ventricular anatomy. The most distal section of the CCS, the PK network, is constructed automatically by an algorithm that generates a full biventricular PK tree from the bundle branches, which is defined together with the ventricular model. The algorithm first selects the nodes that will be used as PMJs, together with intermediate tree nodes. Following, the algorithm establishes the connectivity to form a full network. The construction of the network is governed by global parameters that give rise to a particular structure. The procedure requires a segmented 3D model of the endocardial surface and a few initial branches that correspond to the HB and bundle branches. The resulting models can improve simulations of the electrical activation sequence in the ventricles. Using our algorithm we study differences in activation between models that incorporate the CCS and those that use only discrete stimulation points. In addition, we analyze the resulting pseudo-ECGs for a number of configurations to determine the effect of the PK network parameters in the electrical simulations. The model is tested under normal physiological conditions as well as after a given dose of dofetilide released.

In the following sections the state-of-the-art regarding anatomical and computational models for the CCS is reviewed. Information of the CCS obtained from *ex-vivo* histological or microscopy studies in animals and human cadavers are discussed. Computational models developed in the past for cardiac electrophysiology simulation are presented.

Anatomy of the heart is briefly described in Appendix A-.

B- Anatomy and electrophysiology of the Specialized Cardiac Conduction System

The electrical sequence of activation

The heart is known to beat because an automatic electrical impulse is generated by a set of specialized cells. The full CCS consists of different types of those specialized cells which initiate and coordinate the contraction of the heart chambers. This system became understood within the 20th century. Knowledge of the time course and instantaneous distribution of the excitatory process of the normal human heart are of value for a better understanding of the QRS complex for certain pathologies. To obtain information concerning the time course and instantaneous distribution of the excitatory process in the normal human heart, studies have been made on isolated human hearts and animals using techniques based on electro-anatomical and microelectrode mappings [1, 4].

The overall activation sequence in healthy subjects is well understood in proximal sections. Electrical activation begins in the SAN, located at the junction of the left atrium with the superior vena cava. The electrical impulse spreads to the surrounding atrial muscle through the intercellular junctions and reaches right and left atria. Generally, fibers of the

atrial muscle participate in the impulse propagation from the SAN to the AVN. The AVN is placed between the endocardium and the low-posterior face of the interatrial septum, and is the only electrical connection between atria and ventricles, because fibrous tissue surrounds the AV valves. The electrical impulse reaches the AVN with a delay of about 0.1 s. This delay is due to the little diameter of fibers and allows atria to contract and have time to pump the blood across the atrioventricular valves prior to ventricular systole. After AVN, AP spreads to the HB and the PK network that conduct the electrical impulse to the ventricular muscle. Impulses of the CCS are transmitted first to the papillary muscles and then through the ventricular wall. At first, interventricular septum is activated, then the RV and the anterior wall of the LV, following the lateral wall of the LV and, finally, the posterior wall of the LV. Figure 2 shows with yellow arrows the path followed by the activation signal from the SAN to the ventricles.

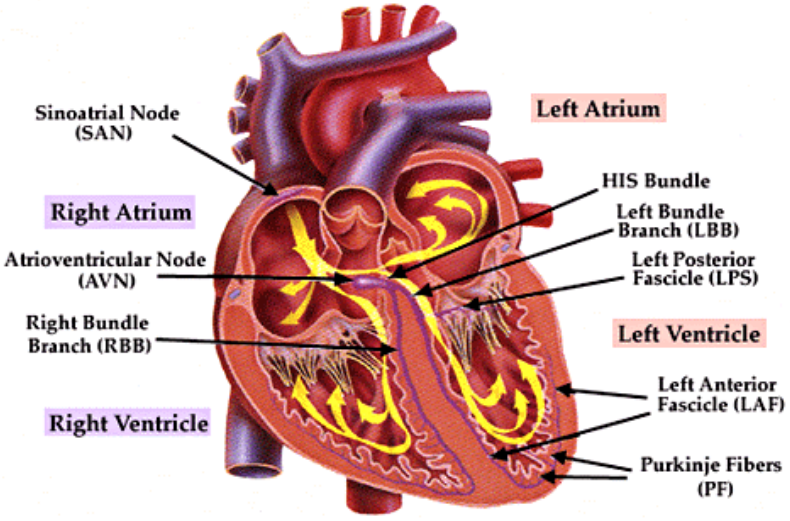

Figure 2. Specialized electrical conduction system of the heart. Yellow arrows indicate the path followed by the electrical impulses from the SAN to the PK fibers.

Due to the complexity of the PK network, the distal section of the CCS, the sequence of activation in the ventricles is not fully understood, and only microelectrode mapping has been able to bring some light into this complex process.

Using 870 intramural microelectrodes Durrer [1] was able to determine three endocardial areas that were synchronously excited 0 to 5 ms after the start of the left ventricular activity potential. These areas increased rapidly in size during the next 5 to 10 ms and became confluent in 15 to 20 ms. The order of activation of the left ventricular areas observed by Durrer were (1) high on the anterior paraseptal wall just below the attachment of the mitral valve; (2) central on the left surface of the interventricular septum and (3) posterior paraseptal about one third of the distance from apex to base. The last part of the LV to be activated usually was the posterobasal area. Endocardial activation of the RV was found to start near the insertion of the anterior papillary muscle 5 to 10 ms after

onset of the LV cavity potential. Septal activation starts in the middle third of the left side of the interventricular septum, somewhat anteriorly, and at the lower third at the junction of the septum and posterior wall. The epicardial excitation pattern reflected the movements of the intramural excitation wave. A nearly completely closed front is present after 30 ms, except at the posterobasal area. At this time, excitation has already reached the epicardial surface of those sites overlying the areas of earliest endocardial excitation. Figure 3 depicts the activation sequence obtained for a human subject.

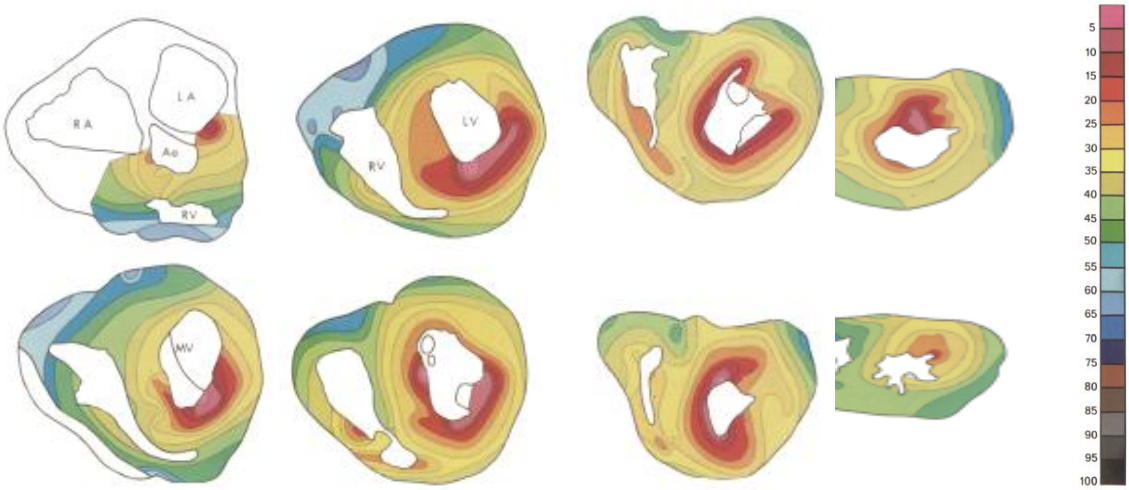

Figure 3. Representation of activation sequence by means of isochronal maps at different horizontal cuts of a human isolated heart obtained by Durrer using microelectrodes. Scale is in milliseconds.

In the different hearts the latest moments of activation were: 71 ms (QRS, 0.08 s), 62 ms (QRS, 0.07 s), 65 ms (QRS, 0.07 s), 80 ms (QRS, 0.08 s), and 74 ms (QRS, 0.08 s).

Detailed studies by Myerburg [4] helped to understand the activation sequence of the interventricular septum. This area is especially important since it is one of the first been activated and its activation has a great influence due to the disposition of the bundle branches. They found that most of the endocardium of the RV free wall is activated simultaneously whereas the LV muscle is activated in an apex-to-base sequence. Right septal activation is from apex to base, and the left septum is activated first at the junction of the middle and lower thirds of the septum and then as a bidirectional wave front toward the apex and the base.

In particular, The RV sequence of activation of the conducting tissue is from the bundle branch, to false tendon, to subendocardial PK network on the free wall of the ventricle. The major ramifications of the bundle branch are a group of false tendons spreading throughout the free wall endocardium as a network of interconnecting tract of conducting tissue (see Figure 4 (a)). These major tracts were activated 10-15 ms and the RBB at the base of the papillary muscle 8 ms after the stimulus. The white numbers on black backgrounds

represent intervals from stimuli to PMJ depolarization. The black numbers on white backgrounds are stimulus-to-muscle depolarization times. The earliest PMJ and muscle activated on the free wall is in the apex, but most of the free wall is activated a few milliseconds later. Only the most basal portion of the free wall is activated later (30-36 ms). In the LV septum (see Figure 4 (b)) the general pattern of activation of the upper two thirds of septum is from the bundle branch, along the major divisions and subendocardial PK fibers, to the junction of the middle and lower thirds of the septum, at which point muscle activation begins and travels back toward the base through ordinary muscle.

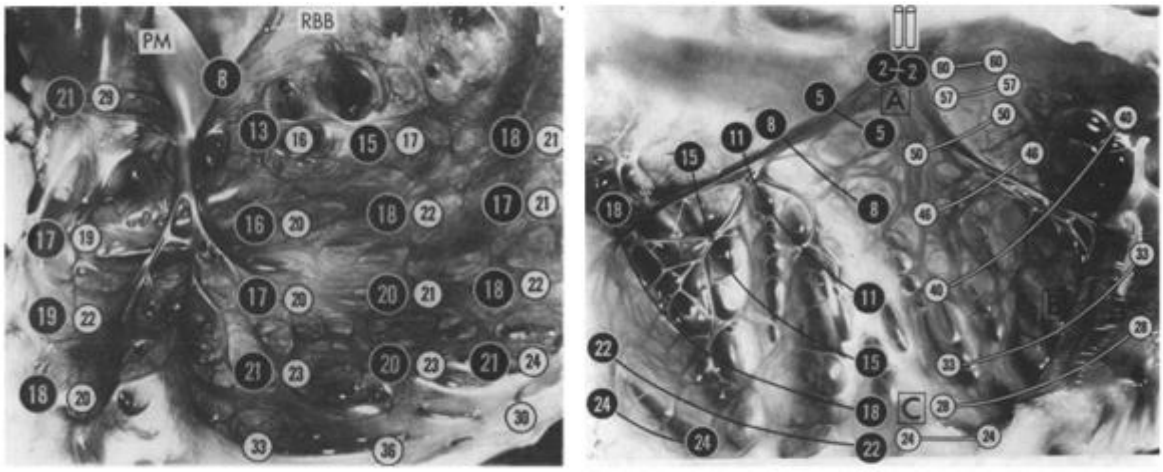

(a) (b)

Figure 4. Activation of (a) the right ventricular free wall and (b) the left ventricular septum.

More recently, ECGI (Electrocardiographic imaging) has been used to image normal human cardiac activation and repolarization in vivo in seven intact healthy adults under completely normal physiological conditions [5]. The first breakthrough occurs in RV anterior–paraseptal region during early QRS and is termed RV breakthrough (RVB). Its timing and location are salient features of normal RV activation. After RVB, additional breakthrough minima appear on RV and LV epicardium. During mid-QRS, more breakthroughs appear in the left-anterior paraseptal region, right-inferior RV, and apical RV region.

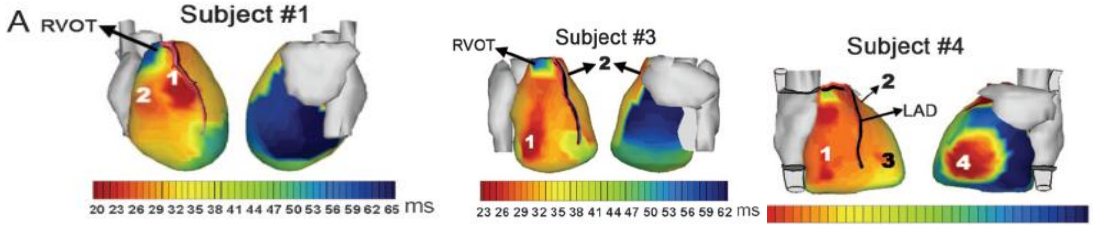

Figure 5. Ventricular and atrial isochrones. Ventricular epicardial isochrones from subjects nos. 1 (A), 3 (B), and 4 (C). Numbers indicate location of early activation sites.

ANATOMY AND HISTOLOGY

Because of the difficulty in identifying conduction tissue, there has been considerable wheel spinning over the last century. People thought they saw things, others did not, and controversy abounded. This is partly because of the lack of markers for this specific tissue. The understanding of the PK pattern was delayed for a long time. In 1845 Jan Evangelista Purkinje published his discovery of a part of the heart conduction system that we call PK fibers [6]. He observed these fibers in sheep's hearts.

In 1906, Sunao Tawara published the results of his two and a half year research. In his publication he described anatomy and histology of the electrical conduction system in several animal specimens and in humans and emphasized the morphological unit of transfer of the AVN to the atrioventricular bundle, bundle branches and PK network [7]. His research was really important for the knowledge of the CCS and PK fibers. Two years later, Einthoven used Tawara's research in the interpretation of the ECG [8].

In 1910, Aschoff [9] and Mönckeberg [10] defined the three conditions to identify a structure as a part of the CCS: 1) the cells of the tract needed to be histologically discrete when compared to their neighbors, 2) the cells should be able to be traced from section to section in the histological series, 3) the cells of the tract should be insulated from their neighbors by a sheath of fibrous tissue. The cells of the SAN and of the AVN satisfied the first two criteria, whereas the pathways for ventricular conduction system satisfy all the three.

Several studies describe the anatomy of the HB and its branches [1, 7, 11-14]. To observe the net structure it is necessary to apply subendocardial injections of ink or stains. It is very difficult to observe the Purkinje-net system in humans, because these fibers do not stain well. Ex-vivo histological and microscopy animal data of the PK network is available thanks to the use of specific stains such as Indian Ink [15], Goldner Trichrome Stain [16] or immunolabeling markers [17], which can be analyzed afterwards from histological and microscopy images.

The HB is one of the easiest parts to observe. It extends from the atrioventricular bundle and has a non-branching bundle, that is usually very short, and branches after perforating the septum in several fibers that form the LBB and in a compact group of fibers that form the RBB, as shown in Figure 6 and Figure 8.

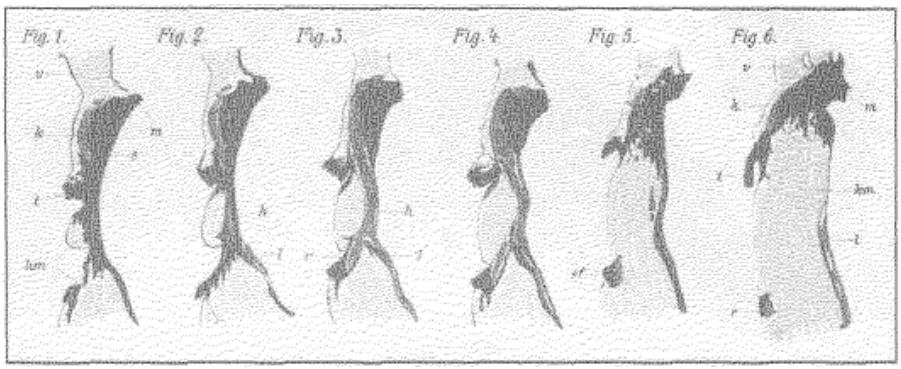

Figure 6. Serial examination of section of HB and initial branches from a human heart.

The most proximal portion of the RBB is identified at the top of the interventricular septum. The bundle branch passes down the septum to the base of the anterior papillary muscle, and after crossing it fans out into multiple free running false tendons terminating on the free wall of the ventricle as a profuse subendocardial PK network. Fibers to the septum from the portion of the bundle branch proximal to the anterior papillary muscle are generally not visualized. However, there are consistently tracts of conducting fibers which reflect back from the base of the anterior papillary muscle and the apical free wall to the lower portion of the septum. The RBB is anatomically separated from the right septal muscle by fibrous tissue.

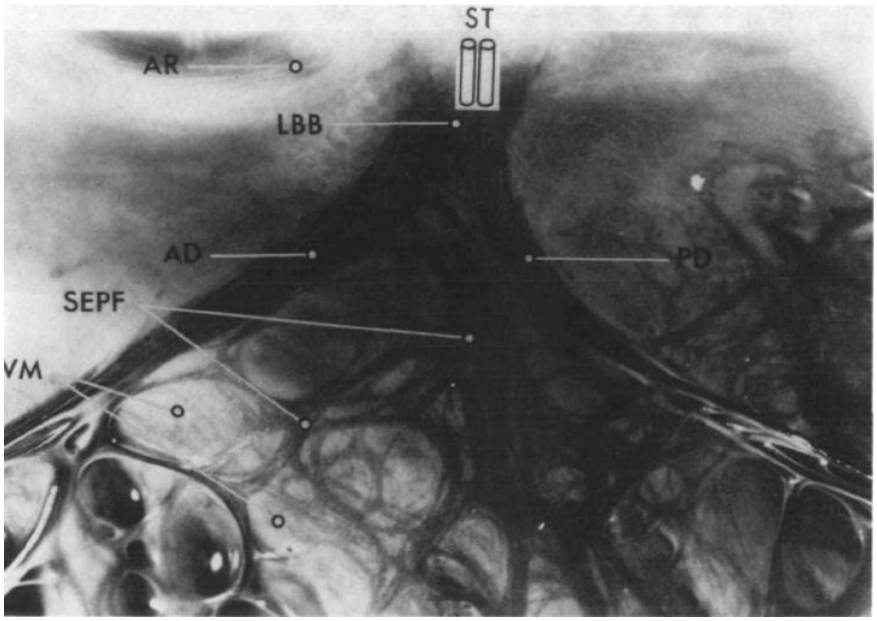

Figure 7. Pertinent anatomic features of the proximal left ventricular conducting system shown by Myerburg.

The LBB is buried deep in the muscle of the interventricular septum and continues to the apex. The gross anatomy of the LBB system is much more complex than that of the

right system. The short main LBB divides into two or three divisions high on the left side of the interventricular septum. Large portions of the anterior (superior) division and the posterior (inferior) division course directly toward the two papillary muscles. A profuse subendocardial network of interlacing PK fibers courses through the septal endocardium bordered by the two major divisions and the papillary muscles. Figure 7 depicts the main LBB and how it bifurcates into an anterior division (AD) and a posterior division (PD) which course toward the apical portions of both papillary muscles (out of picture). A network of subendocardial PK fibers (SEPF) is present between the two divisions. The endocardial true ventricular muscle tissue (VM) can be seen between the tracts of conducting tissue. In humans, it usually forks into three divisions: anterior, medial and posterior. The anterior bundle continues to the apex and forms a subendocardial plexus in the area of the anterior papillary muscle. The posterior bundle goes to the area of the posterior papillary muscle, divides into a subendocardial plexus and extends to the rest of the LV. All divisions pass to PK network of the ventricle [18].

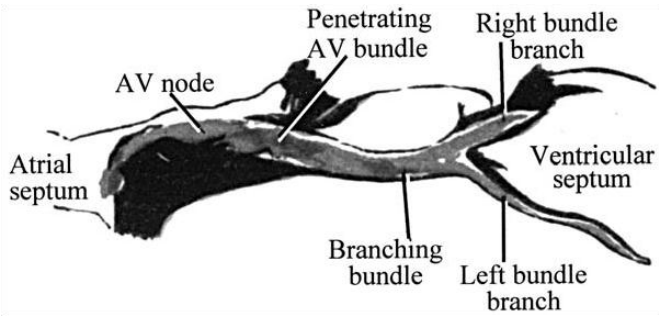

Figure 8. HB described by Tawara [7]. Figure taken from [11].

The RBB becomes subendocardial and forks near the junction between the interventricular septum and the anterior wall of the RV. It passes under the septal endocardium to the papillary muscle and fragments to the network of PK for the walls of the RV.

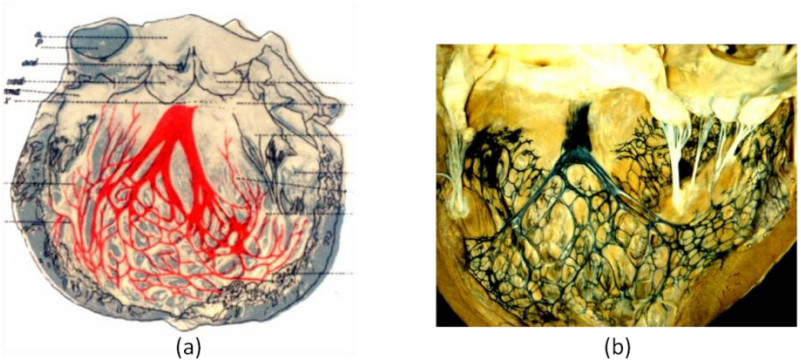

Figure 9. PK network in the LV. Tawara's illustration is very similar to the real network in the photograph. (a) Tawara's illustration, showing the three divisions in human LBB. (b) PK network of a calf heart.

PK network is, as mentioned, the terminal part of the CCS (see Figure 9). In general, the subendocardial PK network has an elliptical disposition in both ventricles, as shown in Figure 9 (b). In the human, PK fibers only reach the endocardial layer and are connected to the working myocardial cells by intercalated disks. In some species, especially in large mammals, it has been reported the existence of intramural fibers that penetrate the ventricular wall and create new branches or anastomosis, forming a complex three-dimensional network in the ventricular muscle. Ryu *et al* found PK cells within the mural myocardium of sheep ventricles, whereas no intramural Purkinje-type cells were detected within the human ventricles (see Figure 10) [16]. In the sheep septum, every intramural PK cell composes a three-dimensional network throughout the mural myocardium, which proximally connects to the subendocardial extension of the bundle branches and distally forms an occasional junction with ordinary working myocytes. Anatomical characteristics of the intramural PK or Purkinje-type myocytes are yet to be fully clarified in mammalian hearts.

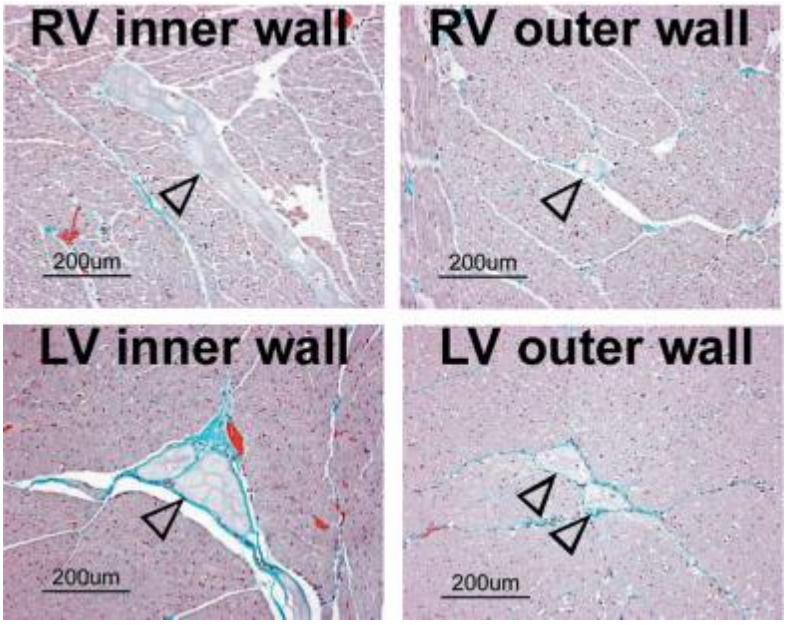

Figure 10. PK cells within the right and left ventricular free walls of a sheep heart. The specialized myocyte with distinctive morphologies (open arrows) are found in both the inner and the outer layers of the ventricular walls.

The junctions between the PK network and the subjacent ventricular myocytes (PMJ) are electrophysiologically defined components of the CCS, where the electrical impulse is delivered to the subendocardial tissue after a certain delay of around 5ms. PMJs are distributed along the course of the PK network which contact to the ventricular fibers. In several studies there has been shown the existence of transitional cells between the terminal PK fibers and the ventricular fibers. Transitional cells have been observed in pig, rabbit, dog and goat, but not in human or bovine where PK fibers gradually become smaller and eventually similar to ventricular myocytes.

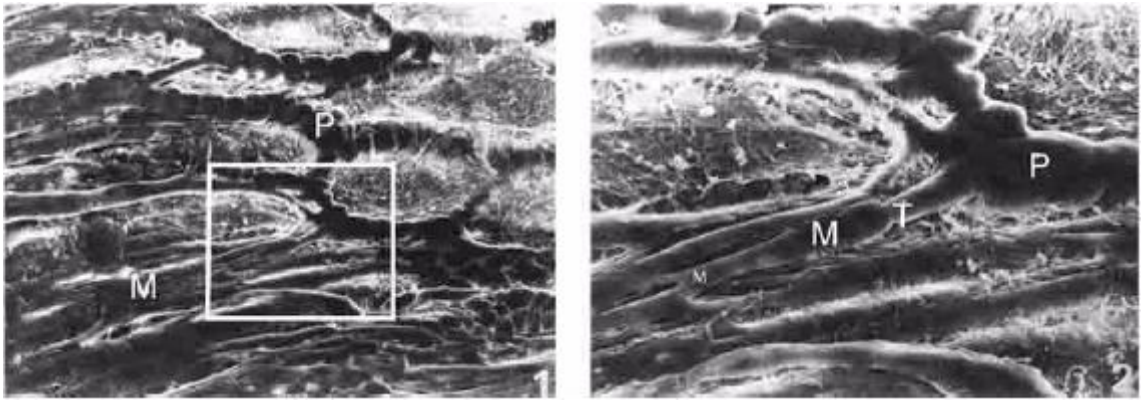

Figure 11. Scanning electron micrograph of the transitional cells of the sheep subendocardial network (a) and a close-up view of the ruled area(b). P (Purkinje), M (Myocardium), T (Transitional).

Using rabbit RV, Cates *et al.* [19] successfully detected around 170 PMJ by recording unipolar electrograms from 528 electrodes, and studying fast electrical deflections (Purkinje) followed by >2 ms slow deflections (ventricular) (see Figure 12). They suggested a more continuous PMJ coupling where antegrade and retrograde conduction are mixed, which is in line with new findings that show a high electrical propagation velocity through trabeculae [20]. This hypothesis is supported by observations of ventricular deflections closely preceding PK deflections in endocardial electrograms in sinus rhythm [19], meaning that the PK and myocardial electrical wavefronts advance in parallel in some regions. More recent, studies of activation of PK fibers in pigs [21] and dogs [22] under fibrillation have also shown an intense activity of the PK fibers both antegrade and retrograde. Assuming a homogenous distribution of PMJs and considering the density of electrodes and size and properties of the endocardial rabbit RV [19], the mean number of PMJ can be estimated in the order of hundreds to thousands.

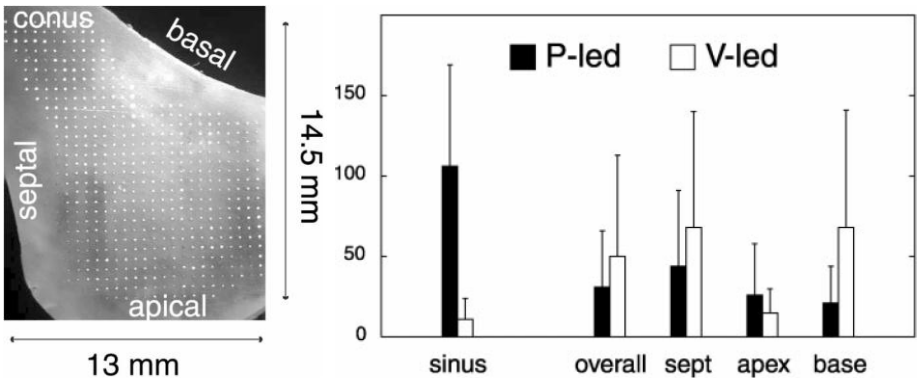

Figure 12. Schematic of the preparation including the position for the recording array (a) and (b) means ±SD for the number of sites with P deflections during sinus mapping and endocardial pacing experiments.

CELLULAR ELECTROPHYSIOLOGY

Action potential

Cardiac excitation involves generation of the AP by individual cells and its conduction from cell-to-cell through intercellular gap junctions. The combination of a locally regenerative process (AP generation) with the transmission of this process through flow of electric charge is common to a broad class of reaction-diffusion processes. AP generation is accomplished through a complex interplay between nonlinear membrane ionic currents and the ionic milieu of the cell.

The discovery by Hodgkin and Huxley (principles of nerve excitation), made it possible to relate important properties of membrane ion channels to the generation of the AP. Later, evidence for electric coupling of cardiac cells through low-resistance gap junctions was established. This property is crucial for the propagation of the cardiac impulse. Over the past three decades, researchers have employed reductionist approaches to define the multitude of ion channels that contribute to transmembrane currents that generate the cardiac AP.

For a single cardiac cell under space-clamp conditions, the following equation relates the transmembrane potential (V_m) to the total transmembrane ionic current (I_{ion})

$$\frac{dV_m}{dt} = -\frac{I_{ion} + I_{stim}}{C_m} \qquad (1.1)$$

where C_m is the membrane capacitance (1 μF/cm^2) provided by the charge separation across the lipid bilayer and I_{stim} is the externally applied stimulus current.

There have been reported differences between AP in PK cells and the rest of myocardial cells. APD is longer in PK fibers than in ventricular cells [23-25]. The AP morphology observed in rabbit and kid, exhibit a prominent phase 1 of repolarization, a more negative plateau and a significantly longer APD_{90} compared to ventricular cells [26]. The prolongation of the APD in PK cells compared to ventricular cells also has also been observed in canine fibers [27-29] (Figure 13). The total amplitude of the AP and the maximal rate of rise of the AP upstroke (V_{max}) are much larger in PK fibers than in ventricular cells.

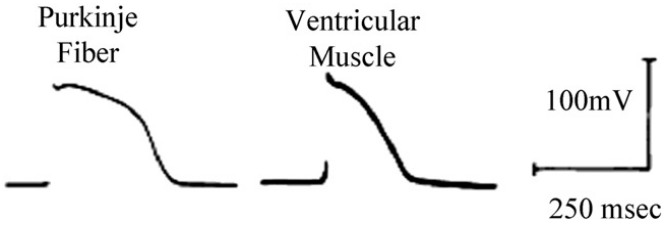

Figure 13. AP from a canine PK fiber strand and ventricular muscle fine electrode recording, paced at BCL=500 ms and $[K]_o$=4 mM. Figure taken from [30].

Gender differences in APs have been reported in canine PK fibers. APD of PK fibers from female hearts have been found to be longer than their male counterparts. No differences in AP amplitude and V_{max} have been reported [31].

Resting potential

No difference in resting potential has been observed between canine PK cells and ventricular cells. Gender differences have not been reported either.

Inward rectifier K^+ (I_{K1}, I_{KATP}, I_{KAch}) channels play an important role in setting the resting potential close to the equilibrium potential for K^+ in cardiac cells. PK fibers display two levels of resting potential, unlike the ventricular cells [30].

Pacemaker current

PK cells have automaticity, although overdrive suppression is the common outcome. Under overdrive suppression PK cells do not show automaticity because their rhythm is overdriven by excitatory waves from the sinus node [31, 32].

During pacemaker activity there is a slow diastolic depolarization during phase 4 of the AP followed by a nondriven AP. Several currents in the PK myocyte could play an important role in generating phase 4 depolarization and therefore in normal automaticity. I_f is usually considered to be the main current [33], although its role in normal automaticity is less clear in other PK fiber studies [34]. In 2007, it was defined a new K^+ current that deactivates at more positive potentials than the PK I_f current, suggesting a role in pacemaker activity [35].

C- Structural models of the Purkinje system

Mathematical models of cardiac electrophysiology can be divided in biophysical models, which try to reproduce the physics of the electrical phenomena at different levels and structural models. The structural models account for the anatomical properties of each tissue or part, e.g. cardiac geometry, the tissue heterogeneity or their structure. The distal section of the CCS shows a very complicated structure, but still it is important to define models which resemble as much as possible to the patterns observed in histological studies.

The simplest CCS models used to stimulate the ventricles lacked of any structure, and only aimed at reproducing the electrical activation patterns described in other electrophysiology studies by means of early activated sites. This is still the technique used by many researchers that use phenomenological electrical models or fast endocardial conductivities to simulate an infinite dense PK system.

CCS models that included some structure date from the late eighties and incorporated the HB and a few branches. Aoki *et al*. [36] model was composed of approximately 50000 cell units (spatial resolution of 1.5 mm.) arranged in a cubic close-packed structure according to anatomical data. The conduction system was composed of the bundle branches and PK fibers, consisting of a few hundred elements.

Abboud *et al.* [37, 38] developed a finite-element three-dimensional model of the ventricles with a fractal conducting system. The two ventricles were modeled as prolate spheroids with a resolution of 0.3-0.4 m, containing around half a million elements. The PK system was modeled like a self-similar fractal tree, assuming that the shortening factor and the bifurcation angle are the same for each generation, as depicted in Figure 14. The model was used to simulate the high-resolution QRS complex of the ECG under normal conditions and ischemia.

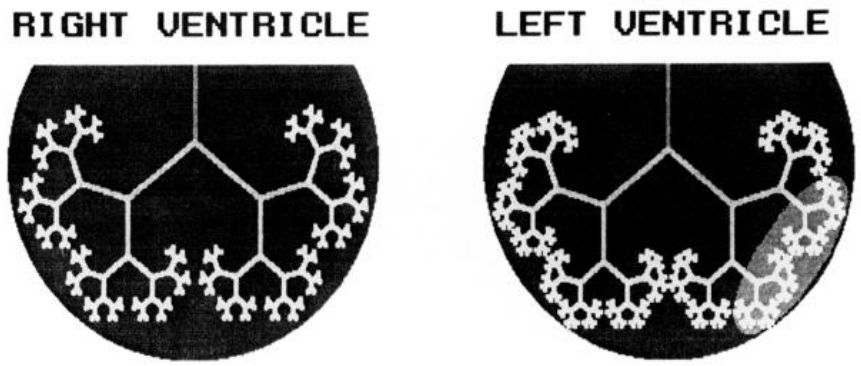

Figure 14. Two-dimensional representation of the model with a damaged region in the LV represented by the light gray area. Image from [37].

Pollard and Barr [39] developed an anatomically based model of the human conduction system with almost 35000 cylindrical elements, although it was not incorporated in a ventricular model. The model was validated with activation time data. In their model, they defined a set of 35 endocardial points from which only 4 were extracted from studies of cardiac activation and draw a set of cables to connect them. The cables were highly refined to form small elements suitable for cardiac electrical simulation, and all the PMJ in the model were fully connected forming a closed network. The model did not show a high correlation with experiments, probably due to the little coupling and the scattered and low number of PMJ used.

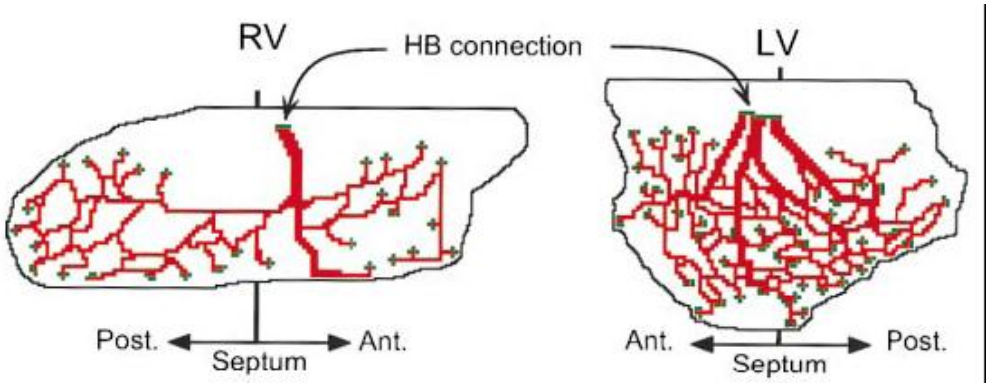

Figure 15. A 2-D representation of the left and right PK network superimposed on the flattened left and right endocardial surfaces. Post. Indicates posterior wall; Ant., anterior wall. From [40]

Berenfeld and Jalife [40] proposed a CCS that also included 214 PMJs, based on the procedure of [39], to study Purkinje-muscle reentries. The model tried to mimic the geometry of main PK strands visualized using stains [7]. Figure 15 shows the sites of interaction where the PMJs are indicated in green and the sites of interaction with the HB by arrows.

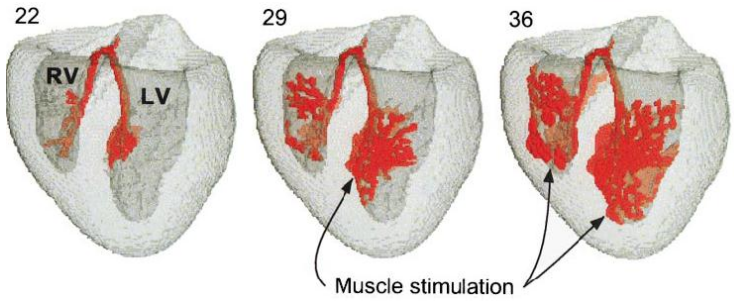

Figure 16. Normal excitation with propagation from the HB downstream past the bundle branches and into the right and left septum, and finally into the myocardium. Numbers indicate milliseconds. From [40]

Figure 16 shows snapshots of the excitation process following an external stimulation of the HB obtained in [40]. Excitation spreads rapidly from the HB (red) to the right and left bundle branches and their subdivisions.

More recently, Simelius *et al.* [41] delineated a PK model for human ventricle by minimizing the difference between simulated isochrones and measurements by Durrer [1] (see Figure 17 (a)). Similarly, Ten-Tusscher and Panfilov [3] built the peripheral conduction system using a similar structure, which included 214 PMJs and followed descriptions available in the literature to place the main bundles (see Figure 17 (b)). Vigmond and Clements [42] developed a PK model by manually drawing the 2D tree structure in an unfolded rabbit ventricle that was afterwards adapted to the corresponding

3D ventricular heart to study sawtooth effects in the PK system. The model had a high spatial resolution and was made of cubic Hermite elements on the endocardial layer.

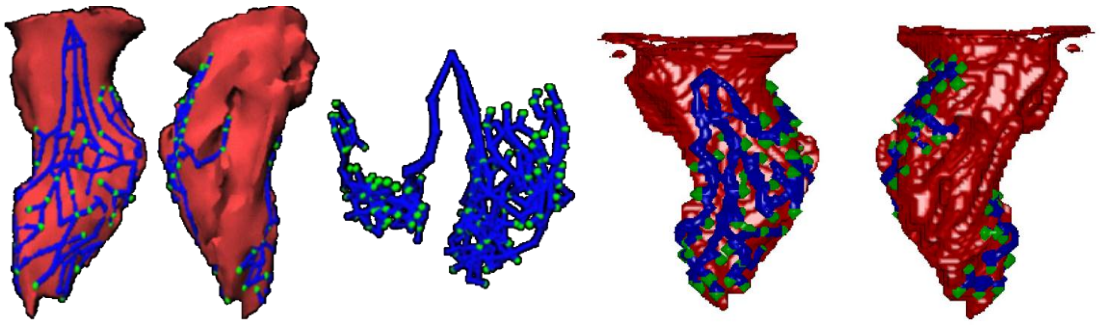

(a) (b)

Figure 17. The geometry of the conduction system observed from different angles. (a) Model from Simelius [41] and (b) Model from Ten-Tusscher [3]. The PMJs are shown as light green spheres.

D- PSEUDO-ECG

Electrocardiology is an almost unique non-invasive diagnostic method for disturbances in cardiac rhythm. According to the laws of electrodynamics, ECG-curves reflect the integral picture of the electrophysiological state of the whole heart at successive instants of time. ECG generation depends on four physiological processes: i) generation of the electrical impulse in the sinoatrial node, ii) transmission of this impulse throw the cells of the conduction system, iii) depolarization, activation of myocardial walls, iv) repolarization, inactivation of myocardial walls. Figure 18 describes these processes.

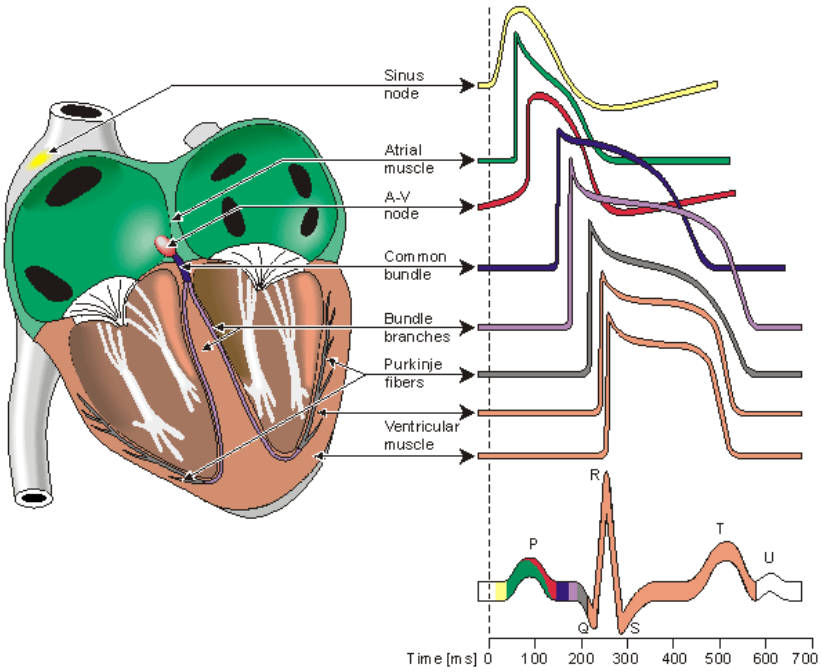

Figure 18. CCS and its relation to ECG. Figure taken from [43]

Pseudo-ECG are a rough approximation calculation of the gradient of the potential field and, performed for the whole surface of electrically activated myocardium, simulates to some degree one of the first hypotheses of ECG genesis in accordance with which the ECG-curve is considered as the “difference of two monophasic curves”, in this case it is the average cell transmembrane activity potentials from two areas of the epicardial surface of the heart.

The simulated pseudo-ECGs in the precordial leads will be compared to those describe by Guyton in his textbook of Medical Physiology [44] (Figure 19):

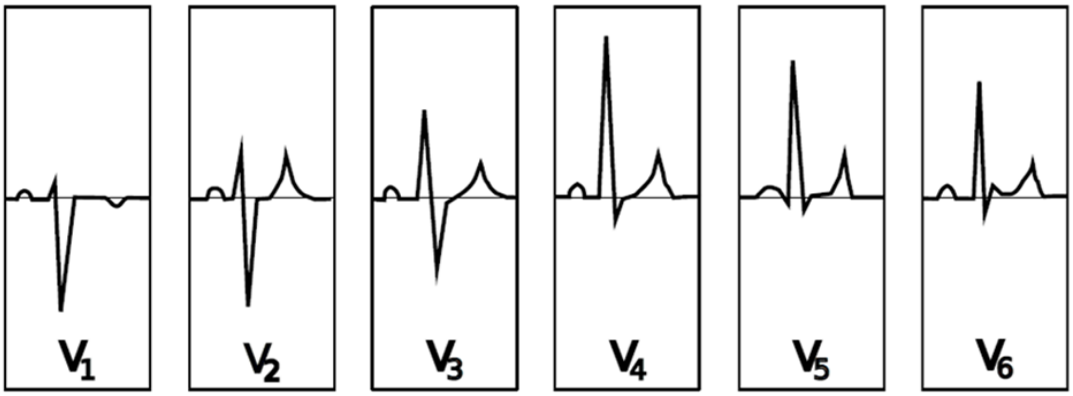

Figure 19. Normal ECG in precordial leads

E- ARRHYTHMIAS AND DRUGS. CASE STUDY: DOFETILIDE

Anti-arrhythmic drugs (classes I, III and IV) are routinely used to treat heart rhythm disorders by directly interfering with cardiac ion channel activity. Some anti-arrhythmic drugs try to prevent arrhythmias by prolonging APD. However, excessive AP prolongation caused by a high dosage of class III anti-arrhythmic drugs is suspected to be the cause of a variety of forms of triggered activity at the cellular level -including early after depolarizations (EAD)- that may degenerate into life-threatening forms of arrhythmia.

Improvements in the assessment of safety pharmacology are therefore urgent to aid in identifying cardiotoxic compounds as early as possible in the drug development process. Regulatory agencies point at the prolongation of the interval between the Q wave and the T wave (QT interval) as the main clinically proven electrocardiogram biomarker for drug safety. It has also been extensively documented that AP prolongation or hERG block are not necessarily related to increased arrhythmic risk. Identification of new and efficient biomarkers of drug cardiotoxicity requires a deep understanding of the mechanisms of drug-induced cardiac arrhythmias. These mechanisms are often multi-scale, spanning from multiple drug-induced alterations in ion channels to whole organ.

The delayed rectifier K^+ channels are responsible for the repolarization phase of the cardiac AP. During a cardiac AP, I_{Kr} current is activated during the plateau phase and is responsible for the repolarization of the transmembrane potential. I_{Kr} is considered to be the most widely targeted K+ channel linked to potential arrhythmogeneity. Many I_{Kr} blockers, which prolong APD, are known to have a negative correlation between their potency and heart frequency, i.e. they do not work as well at higher frequencies (which is exactly when they are needed) and are more potent at lower frequencies, exposing the heart to extremely prolonged APD and risk of Torsade de Pointes (TdP) after episodes of bradycardia.

Cases of TdP have been reported during administration of a drug known as dofetilide. Interestingly, the ability of dofetilide to increase effective refractory period (ERP) was found to be decreased at higher heart rates and increased at low heart rates, which could be related to drug-induced increased pro-arrhythmic risk as described. Dofetilide prolongs QT duration, and its effect is influenced by heart rate. Although dofetilide-induced QT prolongation decreases when the R-R cycle shortens, this reverse rate dependence is only partial because marked QT prolongation persists at an R-R cycle of 600 ms. Results of some studies indicated that dynamic ECG techniques can be useful in detection of subtle, drug-induced changes in the duration of ventricular repolarization [45].

2. OBJECTIVES

This research work has been carried out within the Cardiac Modeling Group (CMG) of the Bioelectronics Group (GBIO) in the I3BH. The CMG has been working in the development of a realistic computational heart model for electrophysiology studies over the last sixteen years. The 3D ventricular model used today has been built from a diffusion tensor magnetic resonance dataset (DTMRI) which includes the fiber anisotropy, an important feature with great influence in the activation sequence of the heart. It also takes into account the different cell populations of endocardial, mid-myocardial and epicardial cells. However, it presents an important limitation: it does not integrate the CCS of the heart (HB and PK fibers).

The general objective of this work is to demonstrate the need of incorporating the CCS in a heart model meant to perform electrophysiology simulations. Furthermore, the inclusion of the system will improve the electrical activation sequence and will allow studying different heart conditions and diseases that we cannot model at the moment, such as bundle branch block.

Several partial objectives are posed in order to reach the general objective. First of all, a literature review of the HB and the PK system. In this study we consider histological, anatomical and electrical data in order to obtain a good description of the CCS of the heart. We define several models of the anatomy of the HB based on this bibliographic review.

Before designing the algorithm that generates the PK network, an in-depth review of the state of the art was done. We analyzed approaches of several researchers and then designed a new algorithm to create the PK network. The implementation of this algorithm is made in several steps, leading at each step to a model which describes more accurately the real anatomical structure of the system. It allows generating randomly different PK networks that we include in the whole ventricular model.

To prove the effect of the CCS, we carry out a simulation study comparing simulations with and without this system. In addition, we show an application of the model to study the global effect of a drug called dofetilide in the heart. Three different scenarios are evaluated and compared: i) control case; and drug cases with ii) 10 nM of dofetilide and iii) 100 nM of dofetilide (a drug that blocks I_{Kr} current). Activation sequence, activation time, repolarization time, isochrones maps and APD maps, and pseudo-ECGs in precordial leads are analyzed for each scenario.

3. MATERIAL AND METHODS

A- ANATOMICAL MODEL OF THE VENTRICLES

In order to perform realistic electrical simulations and study cardiac function it is important to build an anatomical model that take into account both the geometry of the heart chambers and their architecture. Several studies have pointed out the importance of factors such as the anisotropy, due to the shape of cardiac cells, in the cardiac activations, as well as the rotation of the fiber directions from the epicardium to the endocardium or the conduction system [46-49]. Henriquez *et al.* [50] consider that among the most important characteristics of any model of cardiac tissue, there are the ability to reproduce effects due to anisotropy in both intracellular and extracellular regions, the presence of adjacent volume conductors, fiber curvature and fiber rotation.

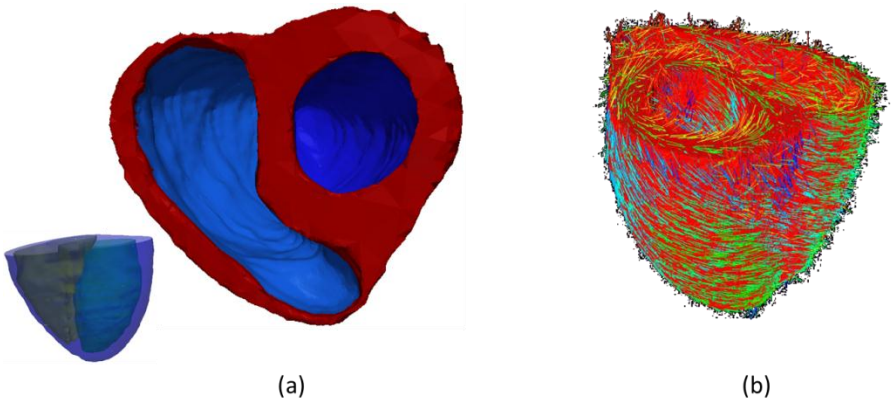

Figure 20. Ventricular human heart model built from a DTMRI stack. (a) Right and left ventricles were segmented and meshed with hexahedral elements. (b) Myocardial fiber orientation represented by small vectors.

In our study the geometry of the ventricular model has been segmented from a DTMRI data set acquired at John Hopkins University [51]. The DTMRI volume stack had a resolution of 0.4297 x 0.4297 x 1.0 mm^3 (256×256×144 voxels). The heart volume has been extracted directly from myocardial segmentation, using a simple threshold and allowed reconstruction of whole ventricular geometry and fiber structure.

The fiber orientation was integrated in the model from DTMRI data. Diffusion Tensor Magnetic Resonance Imaging (DTMRI) has proven to be an effective technique for measuring the diffusion tensor of water within tissue. Water, which is abundant in tissue, diffuses naturally within the tissue microstructure. In cardiac tissue, anisotropic diffusion occurs since there are preferred directions of diffusion due to the tissue microstructure. This information was incorporated into the finite element model by defining an average fiber direction for each element (more information in Appendix B-).

The heart was considered transversely isotropic. Transmurally fiber angles rotated from -60º on the epicardial surface to [+40º, +60º] on the endocardium. Figure 20 (a) shows the ventricular model and Figure 20 (b) the myocardial fiber orientation estimated from DTMRI for this particular geometry.

From the segmented volume, a regular volumetric mesh was constructed with hexahedral elements and a resolution of 0.5 x 0.5 x 0.5 mm^3, which gave rise to 1.43 million nodes and 1.29 million hexahedra [52] (see Figure 21 (b)). With this resolution together with multi-resolution mesh techniques, electrophysiological simulations show stability and accuracy.

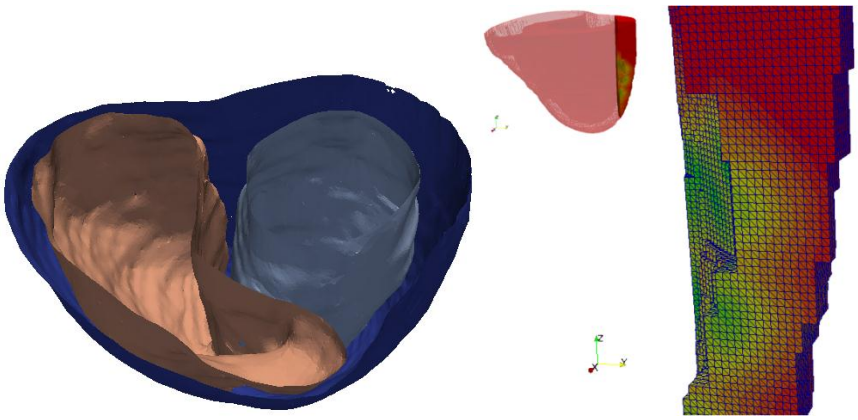

(a) (b)

Figure 21. Biventricular geometry. (a) Labeled regions, LV endocardium and epicardium and RV endocardium and epicardium. (b) Detail of the lateral wall mesh showing the hexahedral elements.

Several studies have shown that ventricular myocardium is formed by three types of cells: epicardial, mid-myocardial and endocardial [53-55]. We modeled the myocardium with the following distributions for each cell population, 17% endocardium, 41% mid-myocardium and 42% epicardium.

These cells differ in the morphology of the AP, especially in the spike-and-dome APs of mid-myocardial and epicardial cells due to the transient outward current, I_{to}. Mid-myocardial cells can be distinguished from other types of cells because they have a short and slow delayed rectifier current, I_{Ks}, a strong I_{to} current and a relatively large Na-Ca exchange current, I_{NaCa}. Rapid I_{Kr} activation and inward rectifying currents, I_{K1}, are similar in the three types of cells. Ionic differences are responsible of the enlargement of APD and of the high speed in AP depolarization.

Histological characteristics of mid-myocardial cells are similar to epicardial and endocardial cells. The mid-myocardial cells have larger APD. They can be found deep in the anterior wall between subendocardium and mid-myocardium, in the lateral wall between subendocardium and mid-myocardium, and across the wall in the outflow tract of

the RV. Mid-myocardial cells are also present in papillary muscles, trabeculae and interventricular septum.

B- ACTION POTENTIAL MODELS

PURKINJE FIBER CELL MODEL BY STEWART ET AL.

In many species PK fiber cell APs have unique features, including a larger upstroke velocity, lower plateau and longer AP duration, and also they can present automaticity due to slow spontaneous diastolic depolarization. These differences are associated with different kinetics and current densities in a number of major ion channels. It is necessary to use a biophysically detailed model for the electrical APs of PK, since they have an important role in ensuring normal ventricular excitation.

We have used the AP model for PK cells developed by Stewart *et al.* [56]. This model is based on the Ten-Tusscher *et al.* [57] and Ten-Tusscher & Panfilov [58] model of human ventricular myocytes, and incorporates experimental voltage-clamp data recorded from human PK cells [59].

The model updates conductance, steady-state activation and inactivation curves and time constants for I_{to}, I_{Kr}, I_{Ks} and I_{K1} and incorporates two additional ionic currents: a hyperpolarization-activated pacemaker current, I_f, and sustained potassium current, I_{sus}, absent in the ventricular cell models but present in PK cells. The resultant model reproduces AP characteristics and is consistent with experimental recordings. The included pacemaker current, I_f, produces auto-rhythmic APs with a cycle length that is consistent with experimental data. The model also reproduces the all-or-nothing repolarization phenomenon observed in PK tissues and the overdrive suppression phenomenon. A schematic diagram describing the ion movement across the cell surface membrane and the sarcoplasmic reticulum in the model is presented below (Figure 22). For a detailed description of the model see [56].

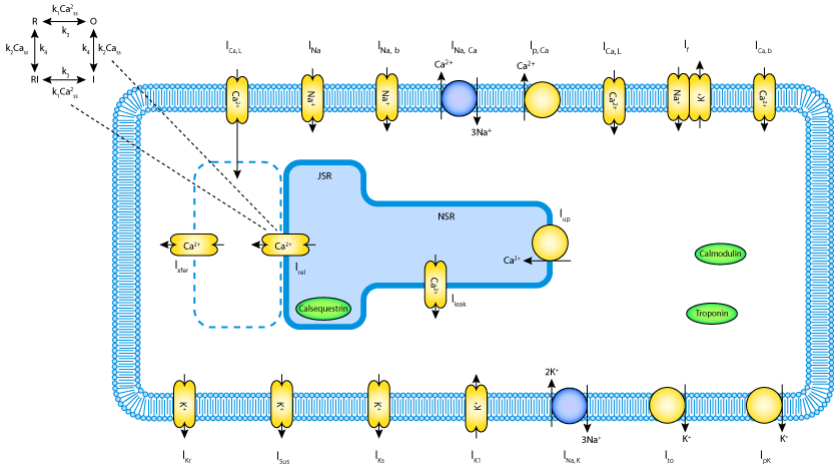

Figure 22. Schematic diagram of the PK cell model of Stewart

VENTRICULAR CELLS MODEL BY TEN-TUSSCHER ET AL.

We have used the model developed by Ten-Tusscher and Panfilov [58], which modifies the model of Ten-Tusscher [57], to describe AP of ventricular cells (Figure 23). An important feature of this model is that all major ionic currents are fitted to recent data on human ventricular myocytes and expression experiments of human cardiac channels. It allows obtaining some important characteristics that are not present in previous models: slower recovery of the fast sodium current differentiated formulations for epicardial and endocardial transient outward current $I_{to,}$ and L-type calcium current with a fast, dominant and stable calcium inactivation and slow voltage inactivation dynamics.

The model reproduces different AP shapes corresponding to endocardial, mid-myocardial and epicardial cells in their lower I_{to} density and their slowly recovery from inactivation, while M cells differ from epicardial and endocardial cells by having an I_{Ks} density four times less than them.

The sum of all transmembrane ionic currents, I_{ion}, is given by the following equation:

$$I_{ion} = I_{Na} + I_{K1} + I_{to} + I_{Kr} + I_{Ks} + I_{CaL} + I_{NaCa} + I_{NaK} + I_{pCa} + I_{pK} + I_{bCa} + I_{bNa}$$

where I_{NaCa} is Na^+/Ca^{2+} exchanger current, I_{NaK} is Na^+/K^+ pump current, I_{pCa} and I_{pK} are plateau Ca^{2+} and K^+ currents, and I_{bCa} and I_{bK} are background Ca^{2+} and K^+ currents.

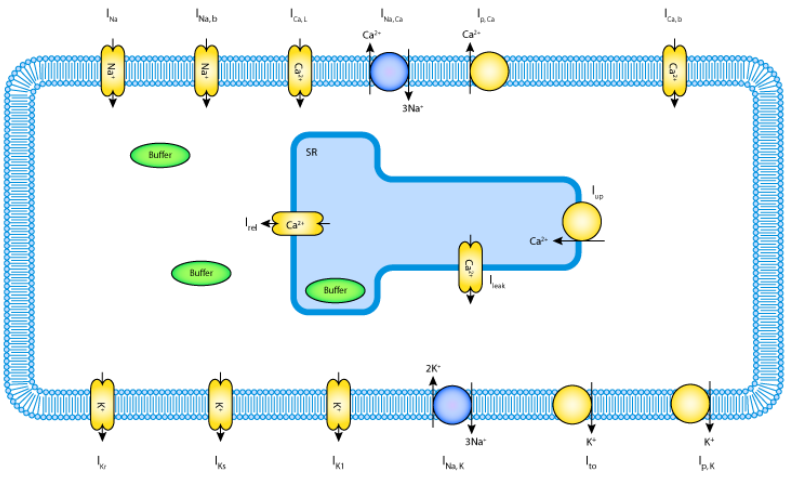

Figure 23. Schematic diagram of ventricular cell model of Ten-Tusscher

Some of the limitations of this model are that differences in APD rate dependence between M cells and epicardial or endocardial cells are smaller than those experimentally observed. In addition, there are further limitations imposed by i) the limited availability of data, ii) the variability of data and experimental conditions, and iii) the potential

deleterious effects of cell isolation. Furthermore, formulation of I_{CaL} time constants is taken from a model based on animal experimental data, since there were no data available.

C- DRUG MODELING: DOFETILIDE

Dofetilide is a class III drug that inhibits the rapid component of the delayed potassium current (I_{Kr}). Therefore, this drug causes a prolongation of the APD without any effect on the resting membrane potential, AP amplitude or maximum rate of depolarization (Figure 24). The APD prolongation increases as a function of the drug dose. Dofetilide also induces an increase in ERP.

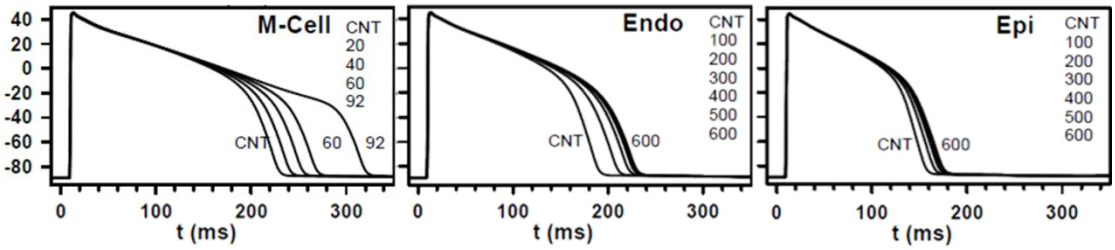

Figure 24. Time courses of APs for M, endocardial and epicardial guinea pig cellular models for 100 nM of dofetilide at a BCL=1000 ms, from the application of dofetilide (CNT, t=0) until steady-state is achieved). Figure modified from [60]

In the ECG, the effects of I_{Kr} block are shown by an increase on the QT segment (Figure 25):

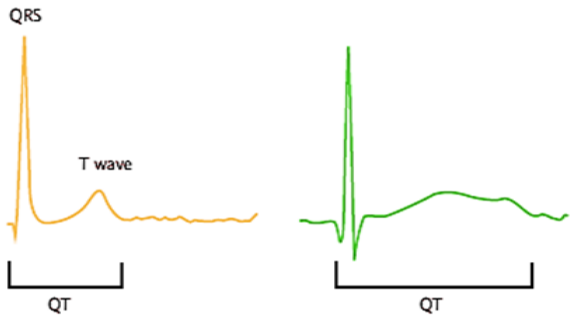

Figure 25. Normal ECG and ECG with I_{Kr} block (long QT).

The effect of dofetilide was modeled by introducing the steady-state factor (1-b) in the I_{Kr} formulation, where b is the fraction of channels blocked by the drug. Thus, the new formulation of the rapid component of the delayed rectifier K^+ current taking into account the effect of dofetilide is:

$$I_{Kr}(D) = I_{Kr0}(1-b) \tag{3.1}$$

$$\frac{I_{Kr}(D)}{I_{Kr0}} = \frac{1}{1+\frac{[D]}{IC_{50}}} = 1-b \tag{3.2}$$

where IC_{50}=7 nmol/l.

D- MATHEMATICAL FORMULATION OF THE ELECTRICAL ACTIVITY OF THE HEART

PROPAGATION EQUATIONS. MONODOMAIN MODEL

The mathematical formulation of the electrical activity of the heart was first described by means of the bidomain model [51, 52], in which the cardiac tissue is represented as two continuous domains (intracellular and extracellular) that share the same space and have unequal anisotropy ratios. The mathematical formulation of the bidomain model consists of an elliptic and a parabolic partial differential equation coupled to a system of stiff nonlinear ordinary differential equations describing the ionic current through the cellular membrane.

Since the bidomain model has a high numerical complexity and it is very computational demanding, it is common to use a simplified tissue model known as the anisotropic monodomain model [52, 61]. In this model conductivity ratios (longitudinal versus traversal) of the intracellular and extracellular domains have the same variation in the anisotropy, i.e. equal anisotropy. This model is widely used for three- dimensional simulations.

Let us derive the monodomain formulation. The electrical current in the intracellular and extracellular domains is expressed by the Ohm's Law:

$$\mathbf{J_i} = -\boldsymbol{M_i}\nabla \mathrm{V_i} \tag{3.3}$$

$$\mathbf{J_e} = -\boldsymbol{M_e}\nabla \mathrm{V_e} \tag{3.4}$$

where $\mathbf{J_i}$ is the intracellular current, $\mathbf{J_e}$ is the extracellular current, $\mathbf{M_i}$ and $\mathbf{M_e}$ are the conductivity tensors and V_i and V_e are potentials in both domains.

The cell membrane acts as a capacitor and due to its small thickness the electrical charge in both sides of the membrane is compensated immediately. Therefore, the accumulation of charge in any point is zero:

$$\frac{\partial}{\partial t}(\mathrm{q_i} + \mathrm{q_e}) = 0 \tag{3.5}$$

where q_i and q_e are the electrical charge in both sides of the cell membrane.

The electrical current in each point is equal to the ratio of the accumulation of charge in both domains

$$-\nabla \mathbf{J_i} = \frac{\delta q_i}{\delta t} + \chi I_{ion} \quad (3.6)$$

$$-\nabla \mathbf{J_e} = \frac{\delta q_e}{\delta t} + \chi I_{ion} \quad (3.7)$$

where I_{ion} is the current through the membrane and χ is the relation of membrane area for unit of volume. The sign of the ionic current is positive when it goes from the intracellular to the extracellular space.

Combining equations (3.6) and (3.7) in (3.5) we have the current conservation equation,

$$\nabla \mathbf{J_i} + \nabla \mathbf{J_e} = 0 \quad (3.8)$$

and substituting (3.3) and (3.4) in (3.8) we obtain:

$$\nabla(\boldsymbol{M_i} \nabla V_i) + \nabla(\boldsymbol{M_e} \nabla V_e) = 0 \quad (3.9)$$

The charge in the cell membrane directly depends on the difference of membrane potential $V=V_i-V_e$ and the membrane capacitance

$$V = \frac{q}{\chi C_m} \quad (3.10)$$

where C_m is the membrane capacitance and

$$q = \frac{q_i - q_e}{2} \quad (3.11)$$

Combining the last two equations and deriving with respect to the time we have,

$$\chi C_m \frac{\partial V}{\partial t} = \frac{1}{2} \frac{\partial (q_i - q_e)}{\partial t}$$

which combined with (3.5) leads to:

$$\frac{\partial q_i}{\partial t} = -\frac{\partial q_e}{\partial t} = \chi C_m \frac{\partial V}{\partial t}$$

And substituting this expression in (3.4) and using (3.1) and $Di=Mi/\chi$ we obtain:

$$\nabla(\boldsymbol{D_i} \nabla V_i) = C_m \frac{\partial V}{\partial t} + I_{ion} \quad (3.12)$$

If we eliminate V_i (V_i=V+V_e) in (3.9) and (3.12), apply the monodomain assumption $\mathbf{D_e}=\lambda\mathbf{D_i}$ and combine the two resulting equations we obtain the monodomain standard formulation:

$$\nabla(\mathbf{D}\nabla \mathrm{V}) = \mathrm{C_m}\frac{\partial \mathrm{V}}{\partial \mathrm{t}} + \mathrm{I_{ion}}(\mathrm{V}, \mathbf{u}) \quad (3.13)$$

with

$$\frac{\partial \boldsymbol{u}}{\partial t} = \boldsymbol{f}(\boldsymbol{u}, V, t) \quad (3.14)$$

where $\boldsymbol{D} = \frac{\lambda}{1+\lambda}\boldsymbol{D_i}$ is the second order symmetric and positive defined conductivity tensor, I_{ion}(V, **u**) the transmembrane ionic current, and **u**(**x**, t) is a vector of gating variables and concentrations, **f** is a vector valued function, and t refers to the time. I_{ion} and **f** depend on the cellular model used.

Equation (3.13) is subjected to the following boundary conditions

$$\boldsymbol{n}\nabla(\boldsymbol{D}\nabla V) = 0 \quad (3.15)$$

where **n** is the outward pointing unit normal to the computational domain.

Therefore, the monodomain model consists of a parabolic reaction-diffusion equation describing the propagation of the transmembrane potential coupled to a system of ordinary differential equations describing the cellular ionic model. This equation has been solved applying an adaptive macro finite element [52].

E- STIMULATION PROTOCOL

WITHOUT PURKINJE SYSTEM: VENTRICLES STIMULATION

In order to obtain physiological activation sequences without explicitly including the rapid conduction system, an alternative stimulation protocol for the ventricles was designed. A total of 100 stimulation points in the RV and 150 in the LV were added, according to depolarization maps and descriptions from Durrer [1]. Those currents are injected into the model as I_{stim} using the equation (1.1), and trigger the depolarization of their surrounding tissue. The stimulus applied to these activation points had duration of 2 ms and intensity of 1200 nA.

The stimulation time of each point was determined according to its distance to the apex, limiting the larger stimulation instant to 50 ms for the farthest point respect to the apex. Therefore the activation time followed an apex-to-base and epicardium-to-endocardium sequence. Figure 26 shows the points chosen for the stimulation protocol.

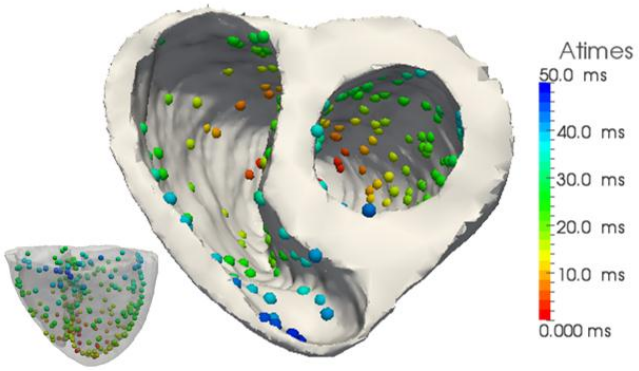

Figure 26. Points of the stimulation protocol. The color of each point represents the activation time.

In order to stabilize the ionic models several heart beats (5000 ms, 5 heart beats) where simulated and only the last one was used to study the electrical activation sequence. This is particularly important for the simulations that include drug models since the initial conditions of the model are affected.

WITH PURKINJE SYSTEM

The stimulation protocol used to activate the ventricles that included a CCS, consisted in the application of a current stimulus in the first node of the atrioventricular bundle model, common to left bundle and right bundle branch. The stimulus applied to this node had duration of 2 ms and intensity of 850 nA. After the stimulus was propagated, each of the terminal nodes of the PK network transmitted the electrical impulse to the heart tissue. The timing and location of those impulses depends fully on the PK network structure and varied as a function of the model.

F- PSEUDO-ECG CALCULATION

According to the bidomain model, in the myocardial coexist two different regions, the intracellular and the extracellular domain, separated by the cellular membrane. Therefore, the myocardium can be considered as a unique cell in which the AP propagates three-dimensionally. Then, the results obtained for the monodomain model can be applied to approximate the extracellular field. Since the total volume occupied by the muscle is larger than the intracellular volume of real fibers, the extracellular potential for a cell has to be multiplied by a scale factor γ (γ<1). Hence, the equation used to calculate the pseudo-ECG signal is:

$$V_e(r) = -\frac{\gamma}{4\pi}\frac{\sigma_i}{\sigma_e}\int_{\Omega} \nabla V(r') \cdot \nabla\left[\frac{1}{|r-r'|}\right] d\Omega \qquad (3.16)$$

where σ_i and σ_e are intracellular and extracellular conductivities, V is the membrane potential, r is the position where the pseudo-ECG is calculated and the integral is extended to the whole myocardial volume. Pseudo-ECGs are calculated considering a homogeneous volume between the heart and the leads where it is obtained.

Pseudo-ECG calculation was performed with a solver postprocessor, after obtaining the membrane potential in each node of the domain as a function of time. Firstly, the gradient of potential is calculated in the centre of each element of the mesh from time-dependent potential data. Secondly the radius vector between the centre of each element and the point in which we want to obtain the pseudo-ECG is measured. This radius vector is used to obtain $\nabla\left[\frac{1}{|r-r'|}\right]$. Finally, V_e is calculated as the sum of the product of the gradient of potential and the inverse of the radius vector and the volume of the element, obtaining the potential of the pseudo-ECG in a time instant at that specific point. This process is repeated for each time step over the duration of a beat, which results in the reconstruction of the pseudo-ECG for a given point.

For measuring potentials close to the heart, standard precordial lead positions were used to calculate the pseudo-ECGs. These leads (V1-V6) are located over the left chest. V1 and V2 are located at the fourth intercostal space on the right and left side of the sternum; V4 is located in the fifth intercostal space at the midclavicular line; V3 is located between the points V2 and V4; V5 is at the same horizontal level as V4 but on the anterior axillary line; V6 is at the same horizontal level as V4 but at the midline. Figure 27 shows the location of precordial leads.

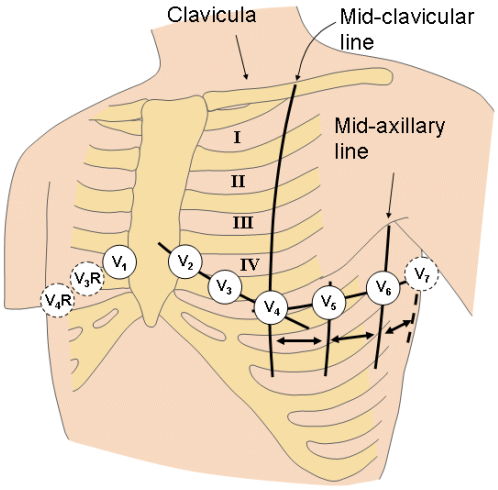

Figure 27. Location of precordial leads (V1-V6). Figure taken from [43]

G- COMPUTATIONAL SIMULATIONS

PRE-PROCESSING. INCLUSION OF PURKINJE MODEL

The pre-processing step is implemented in MATLAB, and it is necessary to include a PK structural model in the cardiac model and format it for the simulator.

First, the nodes from the endocardium of the cardiac model are extracted. Following, we specify the HB configuration that is going to be used from a pre-defined set, and a matrix of endocardial nodes that will be potential nodes of the PK network. Several options are available to ensure anatomical observations such as areas with reduced amount of PMJs (whole endocardial, not nodes in the basal region…). Finally, we can run the algorithm to create the PK network.

The construction algorithm is controlled by the following parameters:

1. index of nodes: points where the net starts its growing,
2. searching radius distance: to define branch growing and PMJs,
3. regions with predefined terminals: index of the central node, radius of the region and percentage of predefined terminals,
4. probability of an intermediate node to be the origin of a little bundle ended in a terminal,
5. probability of forming "elliptical structures": it is related to the probability of connect again a node that is already connected with a neighbor).

After running the algorithm to construct the PK network, this network is processed giving the following outputs:

1) .dat intermediate outputs:

- PKpoints_RV, PKpoints_LV: candidate node that form the PK network (its number is set by the user).
- endoRV, endoLV: final nodes of the PK network in each ventricle. Composed of PKpoints plus the additional nodes that the algorithm may define as terminals.
- conneRV, conneLV: connectivity between the nodes of the PK network (endoRV, endoLV) in each ventricle.
- hisnodes: nodes that form the HB.
- conneHis: connectivity between the nodes that form the HB.
- termiRV, termiLV: indices of terminal nodes (PMJs) in each ventricle.

2) .dat final outputs (inputs for ELVIRA processed):

- CS2H05_nod_PK: specifies the PK network nodes.
- CS2H05_elm_PK: specifies the PK network elements.
- nodesPK_vsim: nodes for the whole ventricular simulation, including the CCS.

- elemPK_vsim: elements for the whole ventricular simulation, including the CCS.
- elemPKTer_vsim: elements indicating PK network terminals (PMJs).

The final PK model that will be used in the simulations can be refined to establish a maximum element size. In addition, a radius needs to be defined to connect PMJs with ventricular endocardial elements within a given distance. All those elements will be excited by a single PMJ.

PROCESSING SIMULATIONS (EMOS)

To compute the results of simulation of the CCS in the ventricular model we used EMOS [52]. EMOS is a finite element solver to compute the resolution of the monodomain equation based in the technique of operator splitting. It allows parallelization for computational. Integration of temporal equations is computed semi-implicitly (implicit for the parabolic equation and explicit for ionic currents) or explicitly. Several types of elements can be used (linear, triangular, quadrilateral, tetrahedrons and hexahedrons) and it is possible to work with meshes with of mixed elements.

Figure 28 shows a file that contains specifications of the model geometry and the simulation analysis that is performed using EMOS.

GEOMETRY

```
!------------------------------------------------------------------------
#TITLE
VOXELIZED HEART H = 0.05 cm
!------------------------------------------------------------------------
#ANALISYSTYPE
1
!------------------------------------------------------------------------
#MATERIAL  (nr; nro of srf; nr of hist.; type; nr of data; data(:))
  3
  1  0  0  0  3  0.0016  0.375  1.0    !. MYOCARDIAL
  2  0  0  0  3  0.180  0.275  1.0     !. PURKINJE
  3  0  0  0  1  0.0005                !. PMJ
#PROP_NOD (nr prop, pointer mat., nr dat_i,  nr dat_r, dat_i,  dat_r)
  4
  1   1   1   0   1
  2   1   1   0   2
  3   1   1   0   3
  4   1   1   0   11
!------------------------------------------------------------------------
#PROP_ELEM,         FILE:"CS2H05_pel_PK.dat"
!------------------------------------------------------------------------
#NODES,             FILE:"CS2H05_nod_PK.dat"
!------------------------------------------------------------------------
#ELEMENTS,          FILE:"CS2H05_elm_PK.dat"
!------------------------------------------------------------------------
```

ANALYSIS

```
#STEP
Tissue preconditioning
!------------------------------------------------------------------------------------------
*RESTART,  -1
!*PARAM_NODE,  FILE:"Circunf_Isq_28prmn.dat"
!*PARAM_ELEM,  FILE:"Circunf_Isq_28prme.dat"
!temporal integration scheme (= 0, exp. s/opt temp; = 1, exp. c/opt temp;
!= 2, imp. s/opt temp; = 3, imp. c/opt temp;)
*INTEG_SCH,         !.Temporal integration scheme
 3
*SOLVER             !.Solver types
 1
*TIME_INC     !.dtini, dtmin, tmax, dtmax, max_inc
0.02   0.02   600.00  0.02  0.02
*STIMULUS,          FILE:"CS2H05_stm_PK.dat"
!*NODEOUTPUT !group of nodes, frequency (in temporal steps), "WHAT WE WANT"
!*ELEMOUTPUT !group of elements, frequency (in temporal steps),  "WHAT WE WANT"
!
*G_OUTPUT {frequency, nr of var., var. 1, var. 2 var. 3}
 1
 2  50
!------------------------------------------------------------------------------------------
#ENDSTEP
#ENDPROBLEM
```

Figure 28. CS2H05_PK.dat file

In the geometry specifications, we indicate the type of analysis that is going to be performed (electrophysiological analysis), the different materials that are taken into account and their electrical properties (conductivity and capacitance), the cellular models, fiber direction defining tissue anisotropy, and the nodal coordinates and elements connectivity that describe the whole model.

The second part of this file describes the characteristics of the analysis. The scheme of temporal integration is indicated (in the example, type 3 corresponds to explicit integration

with temporal optimization). We also specify the type of solver (1 for conjugate gradient method), the time steps and time of simulation and the stimuli sequence to apply. G_output parameter is used to indicate the variables that are written for the model and the frequency in which results are saved. Param_node and Param_elem allow defining masks to change some nodal and elemental properties for simulating pathologies as ischemia, channel blocking, etc.

POST-PROCESSING OF CARDIAC SIMULATIONS

EMOSpost is a FORTRAN code for postprocessing the binary output generated by EMOS during execution. It generates output files in Ensight format that can be visualized with the free visualization software ParaView.

EMOSpost allows obtaining transmembrane potential maps, isochronal maps, APD maps and electrograms or pseudo-ECGs. All these capabilities have been used in our study.

Appendix C- contains a more detailed description of Computational Simulation.

4. PURKINJE NETWORK GENERATION ALGORITHM

A- SEGMENTATION OF ENDOCARDIAL NODES

The human PK network reaches only the inner face of the endocardium. To avoid that the network penetrates deep in the endocardium a thin layer of one hexahedral element of thickness is extracted from the RV and LV.

The endocardial layer extraction is done separately in each ventricle. The algorithm starts with an index that identifies a node of this layer (manually selected) and identifies its neighbor elements that has not connections in one side (because they form the inner endocardial surface). These neighbors are marked as part of the internal thin layer and the process is repeated for them until there are no more internal elements to identify.

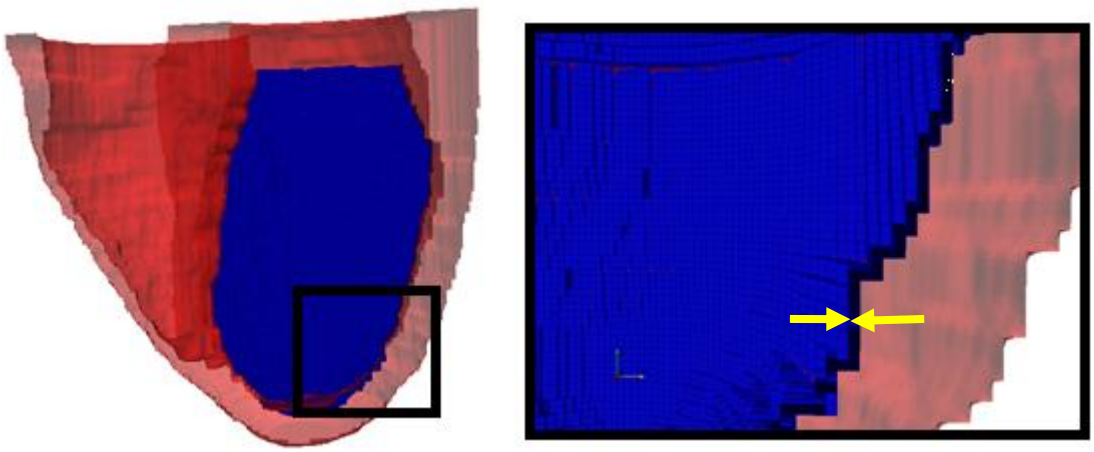

Figure 29. Extraction of endocardial hexahedra. One element thick hexahedra shown in blue inside heart volume in red.

Endocardial nodes resulting of this selection are 51517 in the RV and 44492 in the LV.

B- PURKINJE NETWORK LAYOUT

The PK network nodes are picked from those nodes conforming the inner endocardial face of each ventricle, following a uniform distribution in the ventricles. In this step number of nodes required in each ventricle is set. Selected nodes are saved in a matrix which contains the information indicated below:

4.1. PK network information matrix

$$\begin{bmatrix} Label_1, x_1, y_1, z_1, neighbour_{1,1}, neighbour_{1,2}, is\ connected, is\ terminal\ node, especial\ terminal \\ Label_2, x_2, y_2, z_2, neighbour_{2,1}, neighbour_{2,2}, is\ connected, is\ terminal\ node, especial\ terminal \\ \dots \\ Label_{N-1}, x_{N-1}, y_{N-1}, z_{N-1}, neighbour_{N-1,1}, neighbour_{N-1,2}, is\ connected, is\ terminal\ node, especial\ terminal \\ Label_N, x_N, y_N, z_N, neighbour_{N,1}, neighbour_{N,2}, is\ connected, is\ terminal\ node, especial\ terminal \end{bmatrix}$$

This matrix has a row per node, including the nodes of the HB and the PK network nodes of each ventricle. Each node is described by,

- *Label*, indicating if the node belongs to the HB, to the RV or to the left one;
- *x*, *y*, *z* node coordinates;
- *Is connected*, that indicates if the node has already been connected to the PK network;
- *Is terminal node*, the node is a PK network terminal;
- *Especial terminal*, a terminal node has to be connected to this node. The matrix is initialized with labels and nodal coordinates, while the rest of parameters are set to -1.

C- Definition of the Bundle of His

The HB is the initial part of the CCS. It originates in the AVN. In our model the AVN has been placed approximately 2 millimeters over the most basal part of the ventricular model, in the division between atria and ventricles, as shown in Figure 30.

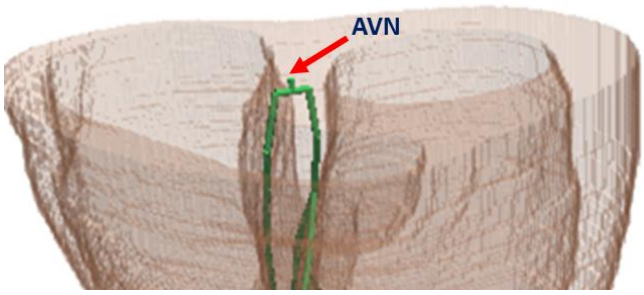

Figure 30. Location of the AVN in the ventricular model

HB definition has been done considering both anatomical and electrical data. In order to study the influence of the anatomy of the HB, several anatomical configurations have been considered (see Table 1). These geometrical structures were generated manually.

Table 1. Summary of the different HB configurations of the model

His Bundle Version	Branches		Ref
	RV	LV	
HB1	2 branches (posteriomedial, anteroapical)	4 branches (anterobasal, anterior and posterior midseptal, anteroapical)	Simelius [41, 62], Ten-Tusscher [3], Durrer [1]
HB2	1 branch (anteroapical)	2 branches (posterobasal, posteroapical)	Durrer isochrones maps [1]
HB3	1 branch (anteroapical)	3 branches (anterobasal, posterobasal, apical)	Massing [12]
HB4	1 branch (anteroapical)	3 branches (anteroapical, posteroapical, apical)	Massing [12]
HB5	1 branch (anteroapical)	3 branches (anteromedial, posteroapical, apical)	Massing [12]
HB6	1 branch (anteroapical)	2 branches (posterobasal, apical)	Damián Sánchez-Quintanta [13]

The first HB configuration (HB1) was based in the models described by Simelius [41, 62] and Ten-Tusscher [3], adding new left mid-septal branches in order to obtain a activation sequence according to Durrer's work [1]. This configuration was defined with two branches for the RV, but after studying the anatomical descriptions of Massing [12] we decided to define just one antero-apical branch for RV.

The second HB configuration (HB2) is simpler. It has just two posterior branches originated in the LBB, one in the basal region and the other one in the apical region. This configuration was based on Durrer isochrones maps [1].

An anatomical study of the HB and the BB in the human heart [12] shows a high variability in this system, especially in the LBB. Massing describes both anterior and posterior divisions of the LBB in different positions. Combining Massing descriptions and isochrones maps obtained by Durrer, we defined three configurations for the LBB (HB3, HB4, HB5) varying the position of the anterior and posterior divisions. See Figure 31 and Figure 32.

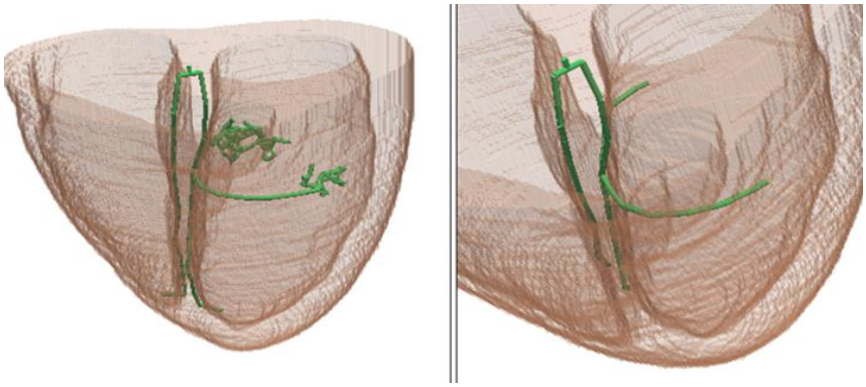

Figure 31. Configuration HB4 of the HB

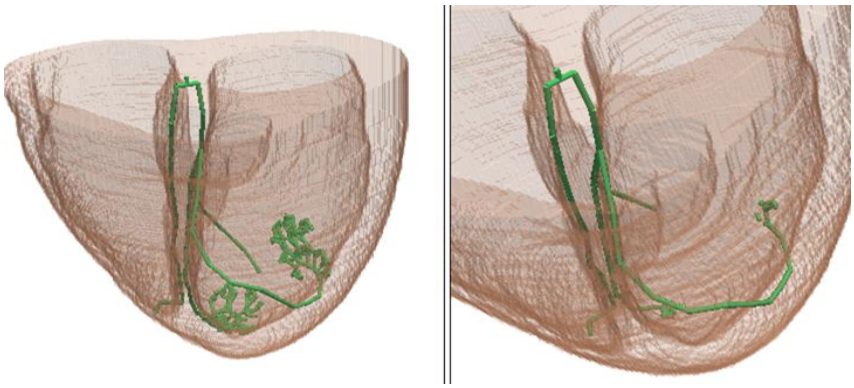

Figure 32. Configuration HB5 of the HB

Finally, a simple configuration of the bundle (HB6) was created, taking into account the information given by the anatomist Damián Sánchez-Quintana. This configuration has just two divisions for the LBB: a posterior division in the basal region and one that continues directly to the apex, as Figure 33 shows.

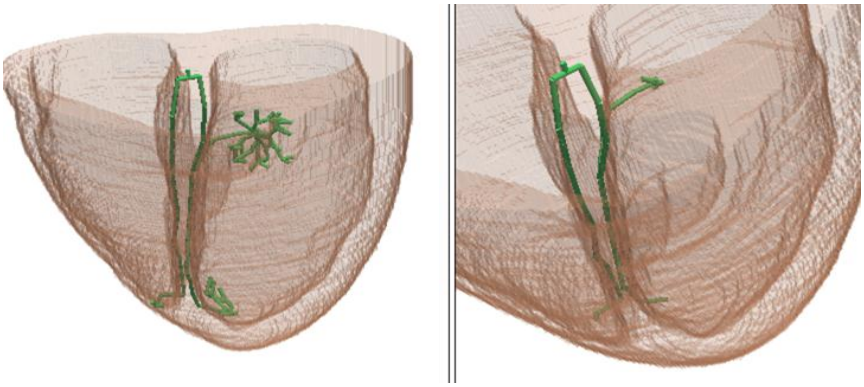

Figure 33. Configuration HB6 of the HB

D- ALGORITHMS TO CREATE THE CORE PURKINJE NETWORK

In order to build an anatomical CCS, we summarized overall properties collecting all the data available from anatomical studies, and created a number of rules that guaranteed them.

Table 2. Overall properties of the constructed PK network obtained from anatomical data

Subpart	Branches	Terminals	Generation	Ref
His Bundle	1 branch from AVN	No	Manual	See Table 1
LBB	See Table 1	No	Manual	
RBB		No	Manual	
Septal PK	# Variable and loops	Yes/ Yes (lower 2 thirds)	Random selection and Radius of search	Tawara [7], Sanchez-Quintana [13], Myerburg [4]
Lateral PK	# Variable and loops	Yes	Random selection and Radius of search	Myerburg [4]
Anterior PK	# Variable and loops	Yes	Random selection and Radius of search	
Posterior PK	# Variable and loops	Yes	Random selection and Radius of search	
Basal PK	# Variable and loops	Yes	Random selection and Radius of search	

The algorithm used to generate the PK network was implemented in several steps, introducing in each step a new characteristic to the resulting network, in order to obtain a net structure that resemble anatomical descriptions.

Some input parameters are common to the algorithms implemented in each step: an array for each ventricle that contains the indices of the nodes where the PK network starts growing, and a distance that is used to set the searching radius to establish neighbor connections. In addition, the HB configuration used to create a PK network has to be indicated.

A general description of the algorithm is presented in this diagram (Figure 34):

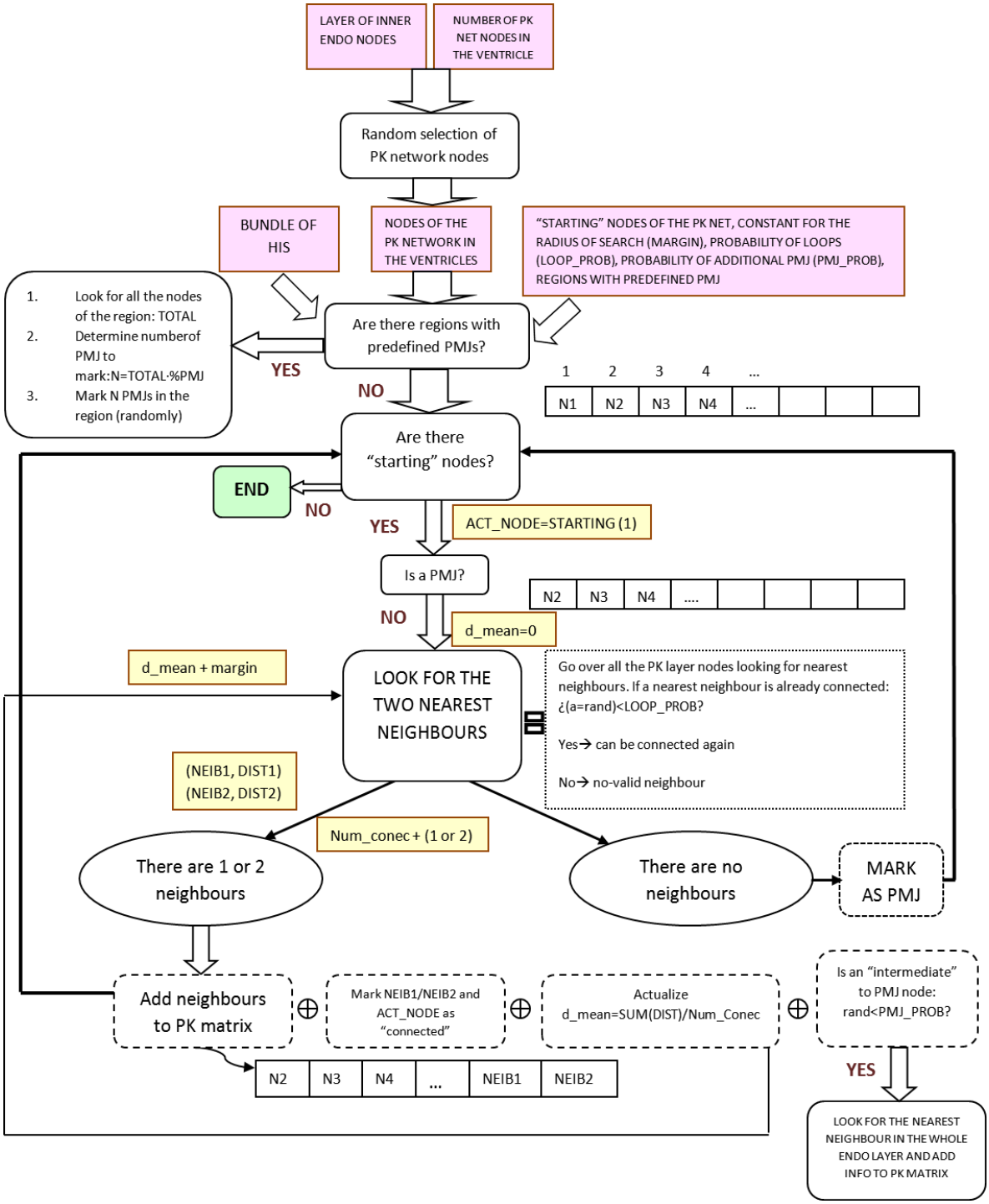

Figure 34. Diagram of the algorithm to create PK networks

The following sections describe the different steps that have been implemented to improve the algorithm.

NEAREST NEIGHBOR

The first implementation of the algorithm connected the nodes of the network following a nearest neighbor algorithm.

Starting nodes of the PK network in each ventricle have to be indicated. The network grows independently in each ventricle from these starting nodes. The algorithm takes the first element of the array and looks for its two nearest neighbors with the same label (RV or LV) in a searching radius. Connections to nodes of the HB are not allowed at this stage. The array is then shifted to the left and this element is deleted. If neighbors are found, they are added at the end of the array and the matrix with the PK network connectivity (4.1) is updated with the neighbors. In the next step the algorithm takes the first element of this array again and repeats the same sequence. This loop is repeated while the array is not empty. The algorithm does not allow a node that is already connected to reconnect again. When the PK network is created, single nodes (those that have not been connected to the net) are deleted and nodes and connections are renumbered.

The searching radius is updated every iteration by adding a constant distance given by the user (input parameter) to the mean distance of the nearest neighbors. The mean distance is obtained adding all distances of the connected nodes and dividing it by the amount of established connections.

This algorithm defines as terminal nodes (PMJs) those that do not have neighbors in their searching area.

PMJ INHOMOGENEITY AND ADDITIONAL "INTERMEDIATE" TERMINALS

The second extension of the algorithm allows indicating regions where there will be a higher density of PMJs and increase the number of terminals in each ventricle.

The regions with a higher number of terminals are identified by the index of the central node, a radius to limit the region and a percentage that determines the number of net nodes of the region that will be set as PMJs. The radius is an absolute distance and it is not measured on the surface of the ventricular model. Terminal nodes defined in each region are decided randomly by the algorithm and marked as PMJs before creating the PK network.

This algorithm also allows forcing a larger number of terminals in the net indicating a probability for each ventricle. In this case, an intermediate node (a node that is connected to other neighbor nodes) can be the origin of a very short branch that ends in a PMJ. In this case, the algorithm looks for the nearest node to this intermediate node in the whole inner endocardial surface of the corresponding ventricle (not just in the nodes previously selected as part of the PK network). This neighbor node is added to the matrix of the PK network (4.1) and is labeled in matrix in the field "especial terminal" of the intermediate

node. Note that in this case, the intermediate node can have up to three neighbors, being one of them a PMJ.

At the end, PMJs nodes can be generated due to i) requirements to increase the number of terminal density; ii) necessity of intermediate nodes and iii) the absence of neighbors in the searching area. Figure 35 shows the PMJs in one of the created PK networks.

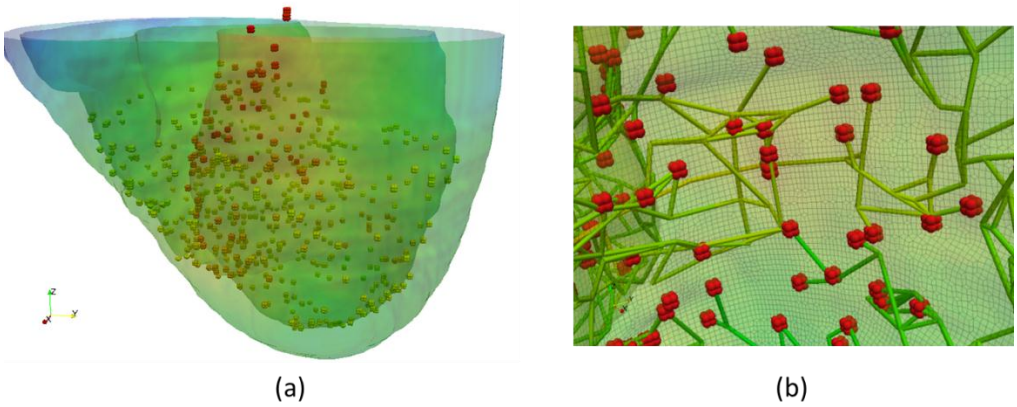

Figure 35. Terminal nodes. (a) Distribution of terminal nodes in the ventricular model. (b) Detail of terminal nodes and their connections

"LOOPING" STRUCTURES IN THE NETWORK

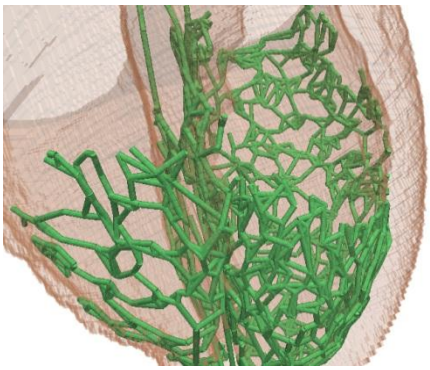

This option allows the creation of structures to imitate the anatomical elliptical structures formed by PK fibers. To implement this feature, two new parameters have been included, indicating the probability that a connected node can be defined as a neighbor of another node. This means that a node that has already been connected can be reached by another branch, forming a "looping" (close) structure with other branches, as Figure 36 shows.

Figure 36. View of a modeled PK network showing "looping" structures

5. RESULTS

A simulation study has been carried out to find out which is the effect of the HB, proximal bundles and the PK network morphology in the sequence of activation of the ventricles. In particular, we study the sequence of activation in the presence of an antiarrhythmic drug known as dofetilide.

Information is analyzed locally, looking at the local activation times (LATs) and APD, and globally by means of pseudo-ECGs. After assessing which are the most suitable parameters that produce realistic activation patterns as described in the literature, a drug called dofetilide is modeled and released into the model in different concentrations. Again, the main effects of the drug are tested in the model and compared with known effects from empirical studies. Finally, we look at the importance of explicitly modeling the PK network and compare it with a model in which the activation is triggered from a set of scattered electrodes placed in the endocardium.

A- CHARACTERISTICS OF THE GENERATED PURKINJE NETWORKS

Several networks were created with different configurations of the HB and varying the input parameters (see Figure 37). These networks were included in the ventricular model and used to launch test simulations in normal conditions (BCL=1000 ms, D=0 nM), comparing the results at tissue level and organ level in order to decide the final network for the complete set of simulations.

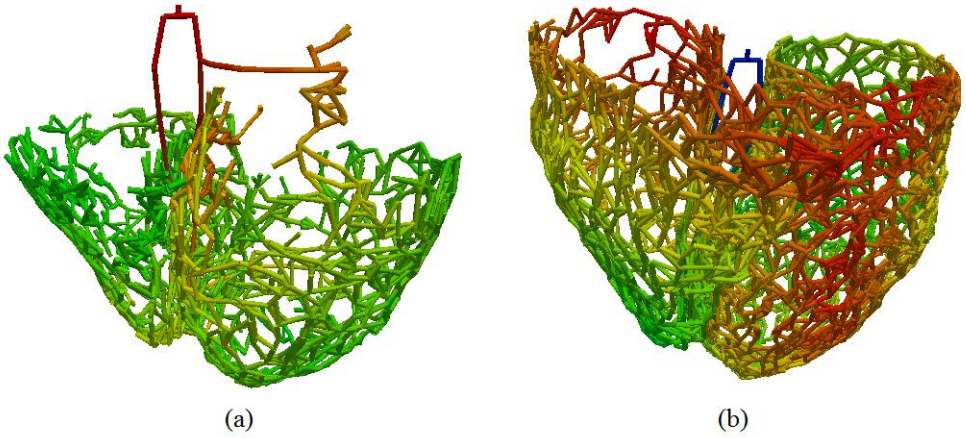

Figure 37. Examples of generated PK networks (a) Uncovering the superior basal third and (b) Covering the whole endocardium in the model.

The final PK network (Figure 37 (b)) used in these simulations was obtained with HB6 configuration of the HB. Several networks were created using parameters shown in Table

3, with different initial number of nodes for the PK network. Finally, we chose the network with 1500 initial nodes in the RV and 3000 in the LV since it gave rise to the more realistic pseudo-ECGs. Nevertheless, pseudo-ECGs obtained with a given set of parameters and HB configuration, in which only the number of nodes was varied do not show significant differences. There is a number of PMJs from which activation sequence does not change.

The PK network grows independently in each ventricle starting at the final nodes of the RBB (anteroapical node) and the LBB (posterobasal and apical nodes). A searching radius was selected to avoid long branches between neighbor nodes and adapted, as the probability of forming "looping" structures and extra intermediate PMJs, to ensure the continuous growing of the PK network.

Table 3. Parameters used in the creation of the final PK network for simulations

Input parameters for network creation		
	RV	**LV**
Initial number of nodes of the PK network	1500	3000
Starting nodes (of growing)	1 (anteroapical)	2 (posterobasal, apical)
Major PMJ density regions	-	Surrounding the starting nodes (1.5 cm radius)
Searching radius of neighbors (cm)	0.3	0.6
Probability of "looping" structures	0.15	0.25
Probability of extra intermediate PMJs	0.15	0.30

The resulting network has a total of 263 PMJs in the RV and 939 in the LV, distributed homogenously except for the region surrounding the starting nodes in the LV, where there is a slightly higher density of PMJs.

The conduction velocity in the PK network was adjusted varying the longitudinal conductivity of this material in order to fit the experimental conduction velocity of 2-3 m/s. In particular, the conduction velocity in our CCS was 2.68 m/s.

B- THE SIMULATION STUDY

In the simulation study we compare results obtained with a biventricular model before and after including an anatomical model of the CCS. The first set of simulations was launched with a ventricular model and programming an activation pattern with several activation nodes distributed randomly over the internal surface of the endocardium, while the second set was launched with the same ventricular model including the anatomical model of the CCS.

Each set of simulations was run in three scenarios, one for normal conditions and the others for different doses of dofetilide (D=10 nM and D=100 nM).

Details about the stimulation protocol can be found in Section 3E-. Five consecutive stimulus of 2 ms were given with a frequency of 1 Hz (BCL=1000 ms) to stabilize the ionic channels and reach a steady state. We only took into account results obtained in the last pulse.

C- Effects of the His and proximal bundles

Several configurations of the HB and its proximal bundles were analyzed (see Section 4C- Table 1). Different input parameters were tested for a particular HB configuration. Finally, in order to perform a sensibility analysis of the different HB configurations, we established a fix set of parameters for the construction of all the PK networks, which are summarized in Table 3. These networks were included in the ventricular model and simulated in physiological conditions (BCL=1000 ms, dofetilide dose D=0 nM), obtaining the activation sequence, isochrone maps, APD maps and pseudo-ECGs.

As an example, Figure 38 shows pseudo-ECGs obtained with a given HB and set of parameters but varying the number of nodes of the network. In particular, the number of nodes in the creation of these networks was 750 nodes in the RV and 1500 nodes in the LV for one of them, and 1500 in the RV and 3000 in the LV for the other. We observed that in this case, the morphology and the amplitude of the pseudo-ECGs do not show significant differences between these simulations, but we would obtain differences in the pseudo-ECGs if the nodes of the network were below a certain threshold of PMJs. In the future, we will study the minimum number of PMJs from which the activation sequence and pseudo-ECGs do not show significant changes.

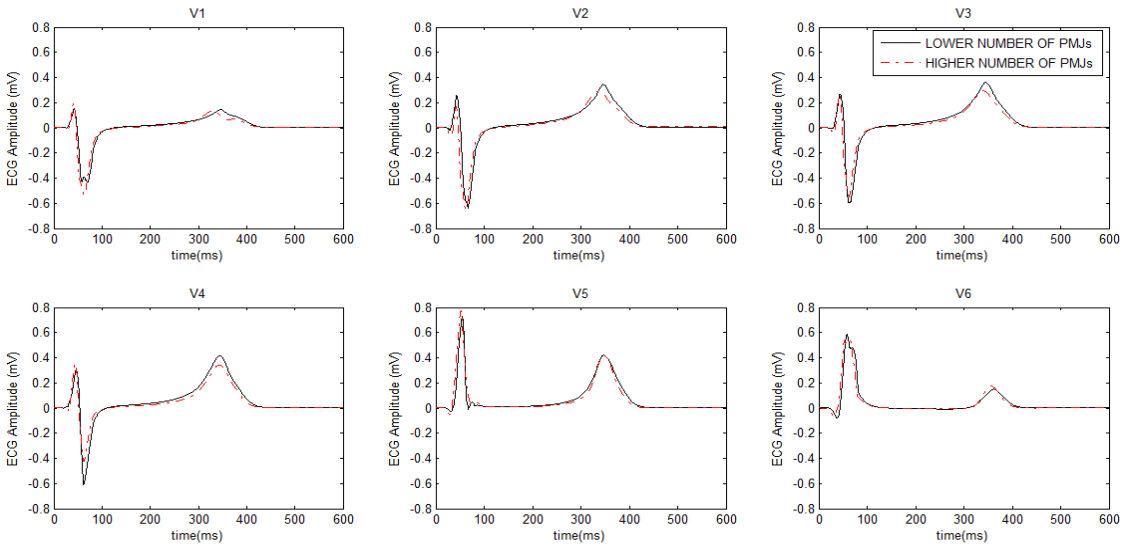

Figure 38. Pseudo-ECGs obtained in precordial leads in two different CCS created with the same algorithm parameters but with different number of net-nodes in each ventricle (and different number of PMJ)

The HB configuration had a remarkable effect on the LATs and the pseudo-ECGs. The morphology of the QRS complex on the pseudo-ECG and the amplitude was the most sensible sensitive indicator. The most simple HB configurations tend to give better results from the point of view of the pseudo-ECG morphology, which were configurations HB4 and HB6 (see Figure 40). To select the final HB configuration we choose the best electrophysiology response instead of the most anatomically realistic one.

Although HB5 configuration was obtained from a more anatomically detailed analysis, simulated pseudo-ECGs obtained with this configuration show an odd morphology (see Figure 39) due to the improper synchronization of ventricles activation.

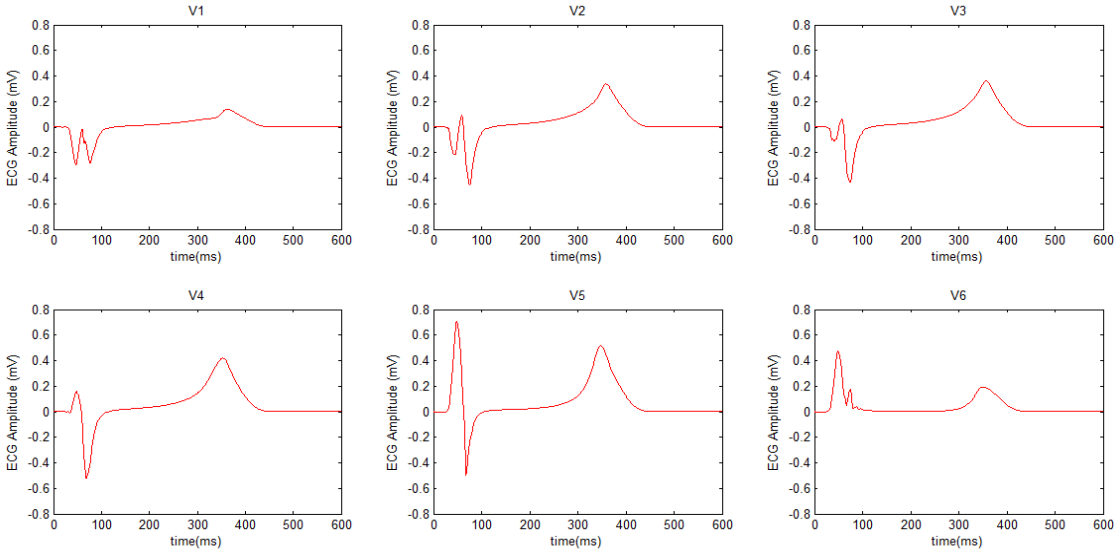

Figure 39. Simulated pseudo-ECGs for configuration HB5 of the HB

We finally choose to perform simulations with configuration HB6 of the HB, because it shows the best morphology in the pseudo-ECG (see Figure 40 (b)) especially in the evolution of the QRS complex (comparing with Figure 19). The QRS complex starts with a positive peak (r-wave) that increase from leads V1 to V3. We do not observe the expected decreasing in the S-wave. T-wave morphology was also similar to the one observed clinically.

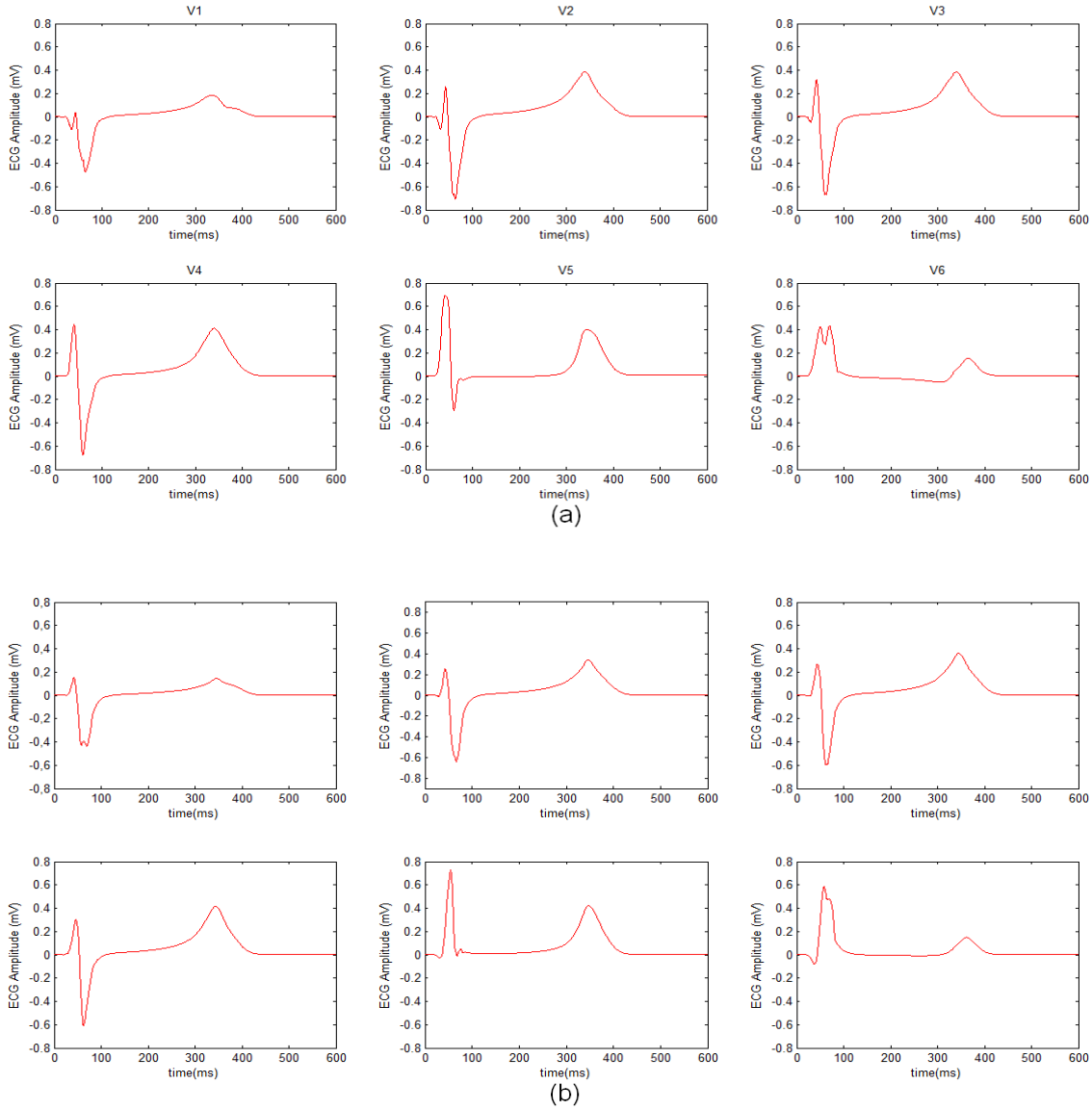

Figure 40. Simulated pseudo-ECGs for (a) configurations HB4 and (b) HB6 of the HB

D- CELLULAR AND TISSUE LEVEL

Our simulation study compares simulation results using a 3D ventricular model without the CCS to results obtained after automatically building and including a model of the CCS in the ventricular model.

We studied the convergence of the APD to establish the number of stimulations required to obtain meaningful simulation results Figure 41 shows the APD dispersion obtained for a dose of D=100 nM (with the CCS) in all the simulated stimuli (5 stimuli, BCL=1000 ms). APDs tend to converge from the second stimulus, but there are subtle differences in APD dispersion for each stimulus. The last two APD dispersion plots,

corresponding to the 4th and the 5th stimulus are quite similar, although not the same, so that five stimuli were considered enough to stabilize the ventricular cell model. Note that main differences (with exception of the 1st stimulus, t0) are observed at highest APD90 values, which corresponds to PK cells APs. This fact could indicate that the model of PK cells developed by Stewart [56] needs more stimulus for its stabilization than the Ten-Tusscher model for ventricular cells.

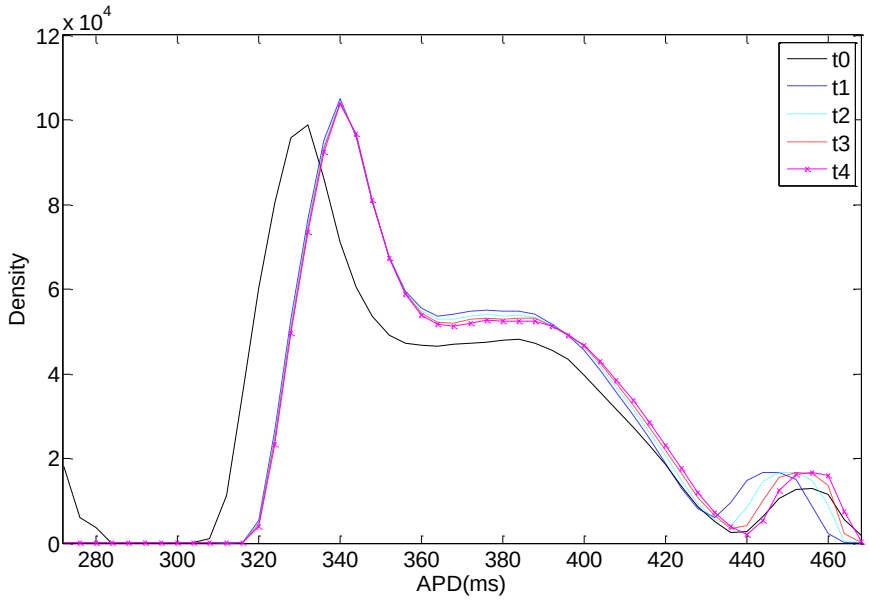

Figure 41. Evolution of APD dispersion for several consecutive heart beats (5 pulses, BCL=1000 ms) for simulations including the CCS with D=100 nM of dofetilide.

To perform the comparison between models at cellular level we calculated APD90 mean values for all cell type and for each scenario (see Table 4), and analyzed APD trends (see Figure 42). We observe that APD90 mean values undergo variations when cells are coupled, i.e. mean values obtained in simulations without PK network in physiological conditions were 320.83 ms in endocardial, 337.04 ms in mid-myocardial and 301.78 ms in epicardial cells, whereas they were 282 ms in endocardial cells, 336 ms in mid-myocardial and 306 ms in epicardial of Ten-Tusscher cellular model [58]. APD90 values that we obtained for ventricular cells for D=0 nM are in the order of the experimental measurements [54, 63-65]. In case of PK cells, mean APD90 in the simulation in physiological conditions was 306.71 ms, which is higher than the value of 293 ms computed by Stewart [56]. This APD90 mean is in the experimental range measured for PK cells, 319±23 ms [66]. The inclusion of the PK network in simulations shortened the mean APD90 in every cell type, although it increased the APD90 prolongation after drug release compare to stimuli-based activation (see Table 4).

APD prolongation is clearly observed in AP plots when we applied an I_{Kr} block. Firstly, we plot APs obtained in physiological conditions for each cell of each type (endocardial, mid-myocardial and epicardial) (see Figure 42 (a)). It is remarkable that, although the morphology of the PK cell agrees with experimental measures, M and EPI cells APs do not show their characteristic spike-and-dome morphology. Figure 42 (b) and (d) show AP variation for different doses of dofetilide in PK cells and M cells, respectively, obtained for a simulation including the CCS. It is remarkable that I_{Kr} block prolongs dramatically APD in PK cells, which is coherent with experimental findings of Gwilt [67]. Finally, Figure 42 (c) and (d) compare APs for an M cell in simulations without and with the CCS.

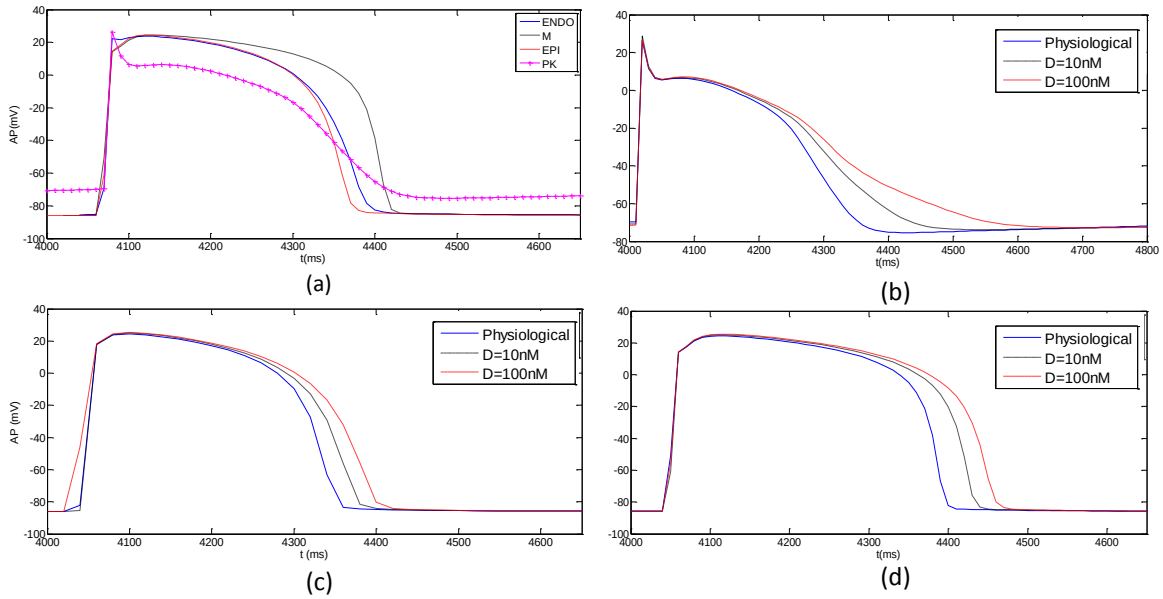

Figure 42. Simulated AP for (a) different cell types in physiological conditions and for physiological conditions and different doses of dofetilide in (b) PK fiber. (c) M cell AP in simulations without the CCS. (d) M cell AP in simulations including the CCS.

I_{Kr} block has a higher impact on mean APD90 prolongation, for simulations including the CCS than those without it, especially for high doses of dofetilide. The APD90 variation compared between simulations with and without PK is greater for the ENDO cells, followed by M cells and, EPI cells. In EPI cells the difference in the increment between these simulations is not significant. APD90 prolongation of ventricular cells (see Table 4) has a mean value of 9.31% for D=10 nM and 16.16% for D=100 nM in simulations without PK network, while its value in simulations with PK is 10.25% for D=10nM and 18.07% for D=100 nM. These results are in agreement with experimental values reported for APD90 prolongation, which are for total I_{Kr} block: 11% by Iost *et al.* [68] and 26.19% by Li *et al.* [64]. Furthermore, results show that PK cells APD90 increments notoriously with I_{Kr} block, (20.37% for D=10 nM and 48.79% for D=100 nM), and suggest that there is a direct effect of the PK cells in the APD90 prolongation of the other cell types, mainly for those layers that are closer to the PMJs, i.e. ENDO.

At tissue level we obtained and analyzed isochrone activation time maps, isochrone APD maps and APD dispersion plots.

Firstly, we briefly mention the time delay in PMJs. As it is visible in Figure 43, this delay was around 5 to 8 ms.

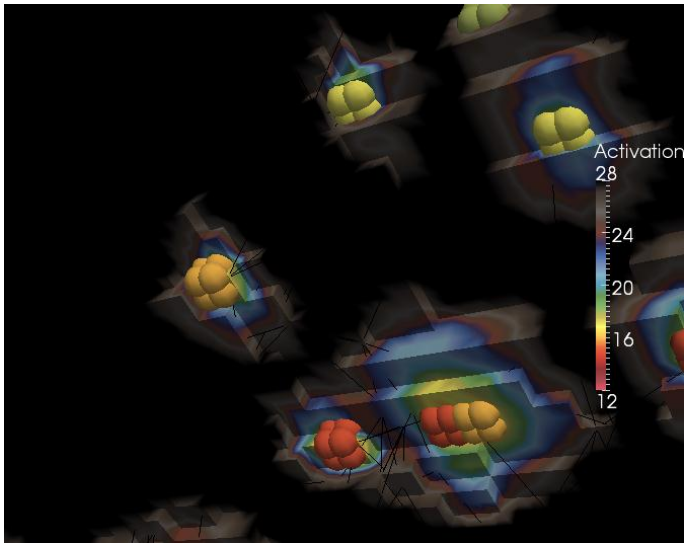

Figure 43. Activation of the ventricular wall in contact with PMJs in the neighboring region of PMJs. Color indicates the time of the activation in ms.

Experimental maps obtained by Durrer show a high variability in epicardial activation (see Figure 45) and Durrer's work shows just one map corresponding to endocardial activation (see Figure 44). Therefore, it is not possible to compare directly his electrical activation maps with the results of our simulations.

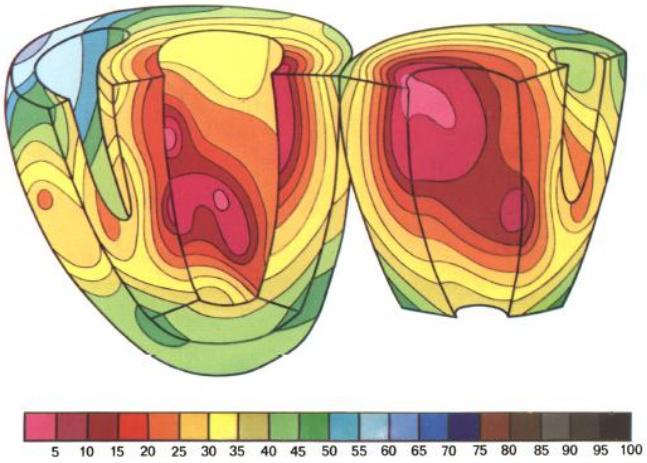

Figure 44. Three dimensional isochronic representation of the activation reported by Durrer. Color indicates time of activation in ms. Figure from [1]

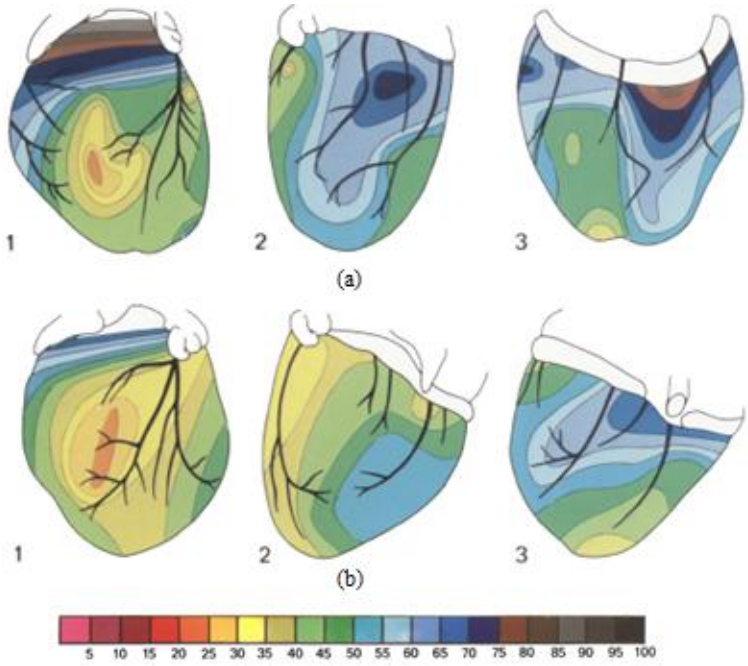

Figure 45. Two examples of epicardial excitation maps in human hearts. Hearts (a) and (b) are presented showing (1) an anterior view, (2) a left lateral view and (3) a posterior view. Color indicates time of activation in ms. Figure from [1]

As an example, we show in Figure 46 similar epicardial excitation map views obtained for a simulation which includes the CCS. The activation pattern in the simulation is different from the experimental maps of Figure 45, although, a direct comparison between them will have no sense due to the high variability between individuals. Nevertheless, looking at the general trends, it is visible that the time of epicardial activation is similar in all the activation maps (experimental and simulated).

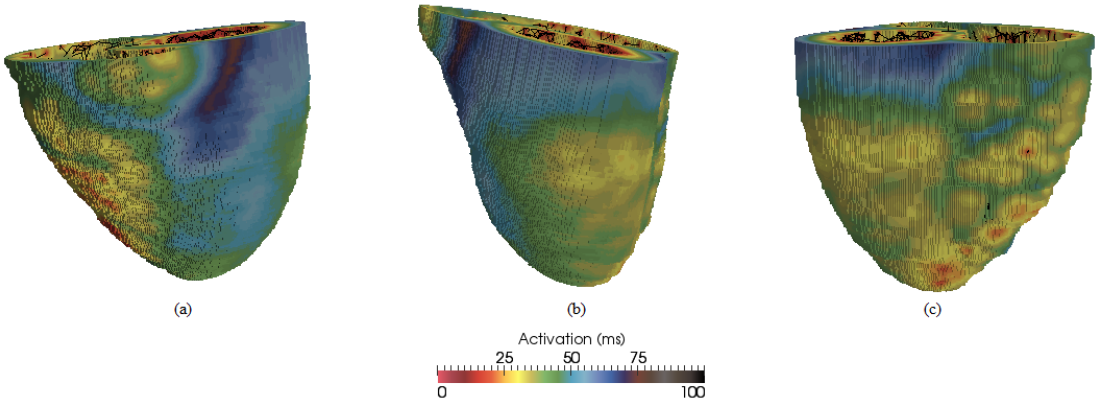

Figure 46. Epicardial excitation maps in simulation including CCS for control case. The heart model is presented showing (a) an anterior view, (b) a left lateral view and (c) a posterior view. Color indicates time of activation in ms.

The total activation time measured by Durrer in his experiments varied between 62 and 80 ms, with a mean value of 70.11 ms (measurements in 5 hearts). The activation time in our simulations is in the range given by Durrer for simulations with the complete ventricular model (which includes a CCS). In this case the total activation time in normal conditions is 76 ms, while in simulations using discrete stimulation points without a PK network, the total activation time was significantly longer (88 ms).

Activation times were also measured in simulations with I_{Kr} block produced by dofetilide. No significant changes in the activation sequence were observed between simulations with and without I_{Kr} block as expected, since this current does not contribute to the activation phase.

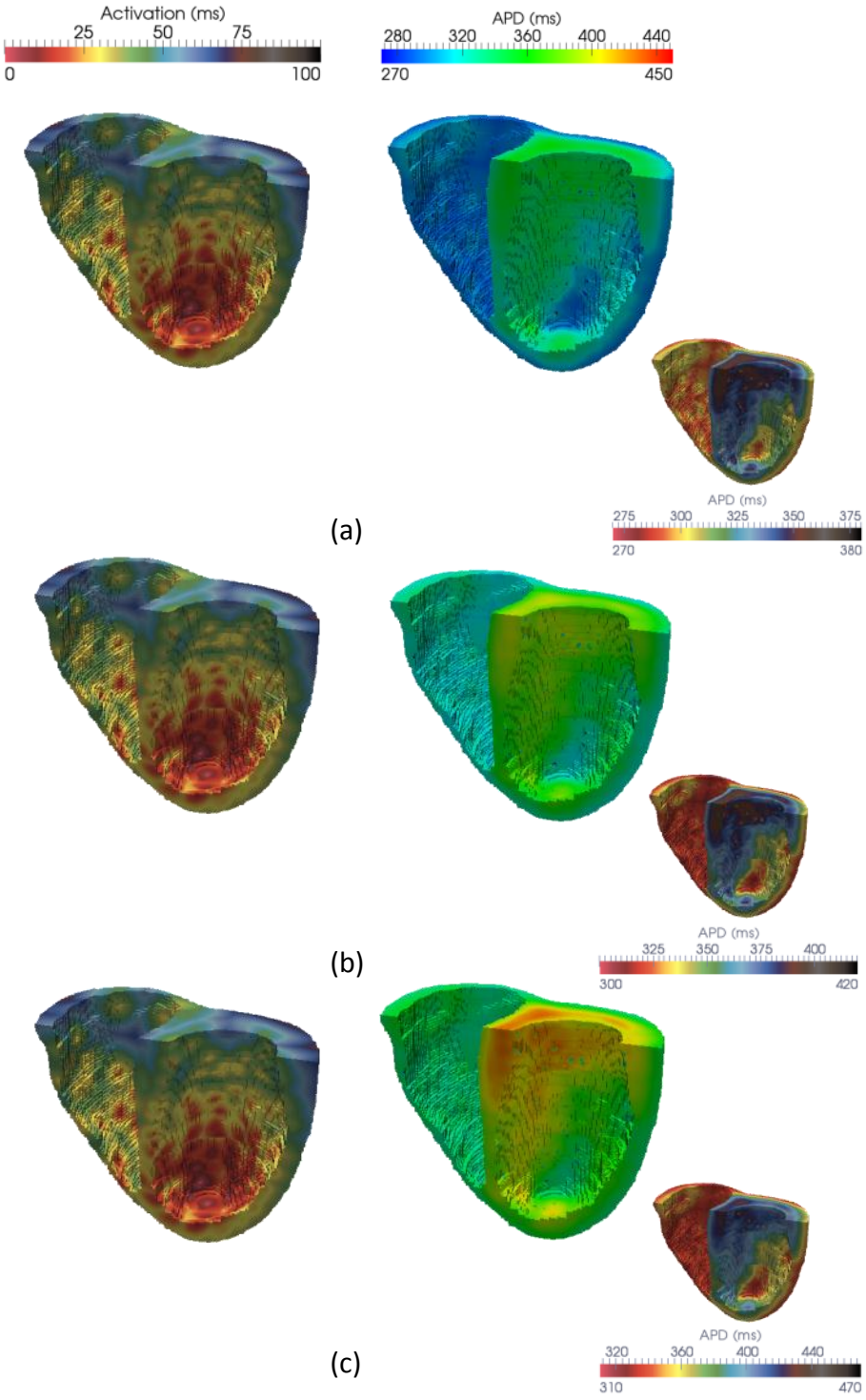

Figure 47. Isochrone maps (left) and APD maps (right) of posterior view in simulations without the CCS for different doses of dofetilide. Isochrone maps show that I_{kr} has no effect in the activation time, while APD maps show that I_{kr} block increases the duration of the AP. Larger APD maps figures have a common APD colormap range, while others APD maps figures have their own colormap range. Dofetilide doses applied were (a) D=0 nM, (b) D=10 nM, (c) D=100 nM. Color indicates time of activation in ms in the isochrone maps and APD in ms in APD maps.

Comparison between isochrone activation maps of simulations without (see Figure 47) and with the CCS (see Figure 49) show significant differences in the activation pattern. The apex-to-base activation pattern is clearly visible in simulations without the CCS model, because the activation points were programmed with this sequence, while simulations including the CCS do not reproduce clearly this apex-to-base pattern, because PMJs are distributed randomly over the whole inner endocardial surface and there is no direct control on their activation times. However, the endo-to-epi activation pattern reported by Durrer (Figure 48) is clearly visible in activation maps with the ventricular model including the CCS (see Figure 49), due to the high number of PMJs. This is not the case in the other set of simulations because the low number of distributed activation points does not activate the whole endocardium before the propagation reaches the mid-myocardium and the epicardium.

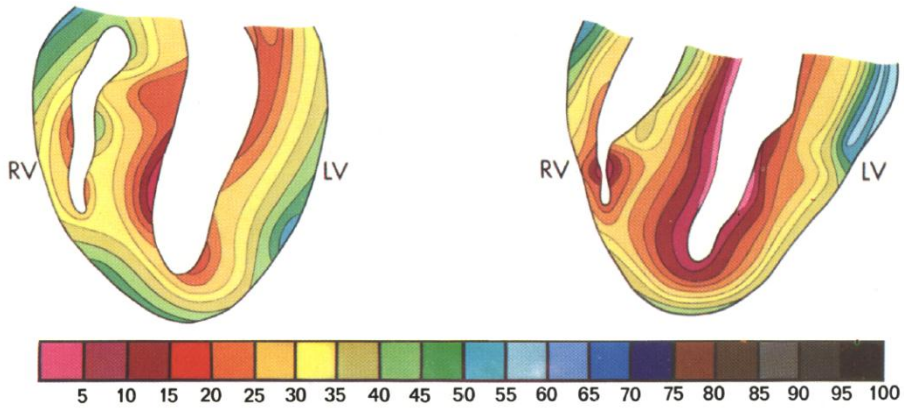

Figure 48. Section in two different human hearts showing the endo-to-epi activation pattern. Color indicates activation time in ms. Figure from [1]

We have also obtained the activation maps inside the CCS for physiological conditions and each drug dose (D=10 nM, D=100 nM) (Figure 49 right).

We observe that total activation time of the CCS is lower than whole ventricle activation because stimulation starts in the PK network which in addition has a higher conduction velocity. The first parts of the LV PK network to activate are the posterobasal LV and the apical regions, since the network starts its growing in these regions. In the RV PK network, activation starts in the apex. As we noted for the ventricular activation isochronal maps, blocking I_{Kr} current has no effect on the overall activation.

We have analyzed isochronal APD maps in each set of simulations. Comparison between APD maps in simulations with and without the CCS for each drug dose (physiological conditions, D=10 nM, D=100 nM) show clear trends depending on the drug dose and cell type. Not surprisingly there are variations in the APD intervals due to the

coupling with the CCS. Nevertheless, APD trends between different types of cells are still kept in the APD maps (see Figure 47 and Figure 50, small figures on the right), with independence of the drug doses. The reason is that the ventricular model is the same in both cases, with a cell population distribution of 17% endocardium, 41% mid-myocardium and 42% epicardium. Coupling the CCS modifies the APD range in the endocardial and mid-myocardial cell types but do not affect its pattern.

We observe differences in APD inside the CCS, although the cell model is the same, probably due to the coupling of the fibers and the interaction with the ventricle at the PMJs, but these differences are limited to a narrow range.

APD maps in Figure 47 (left) and Figure 50 (left) have the same colormap scale for (a) D=0 nM, (b) D=10 nM and (c) D=100 nM. APD prolongation produced by I_{Kr} block when adding dofetilide is clearly visible in these plots. APD maps with common colormap of the PK network (Figure 50) show a pronounced APD prolongation in PK cells when blocking I_{Kr}.

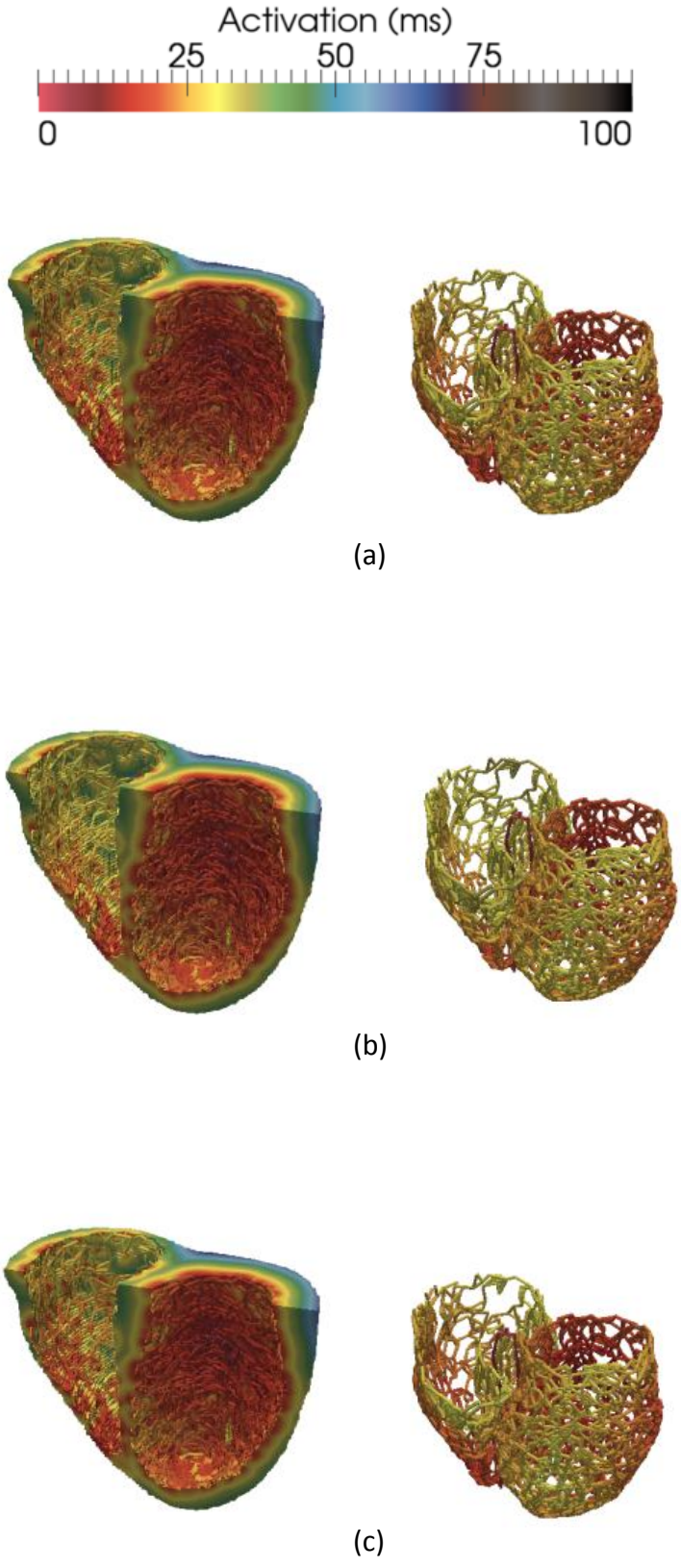

Figure 49. Isochrone maps of posterior view along with the CCS for different doses of dofetilide showing that I_{kr} block has no effect in the activation time. Dofetilide doses applied were (a) D=0 nM, (b) D=10 nM, (c) D=100 nM. Color indicates time of activation in ms.

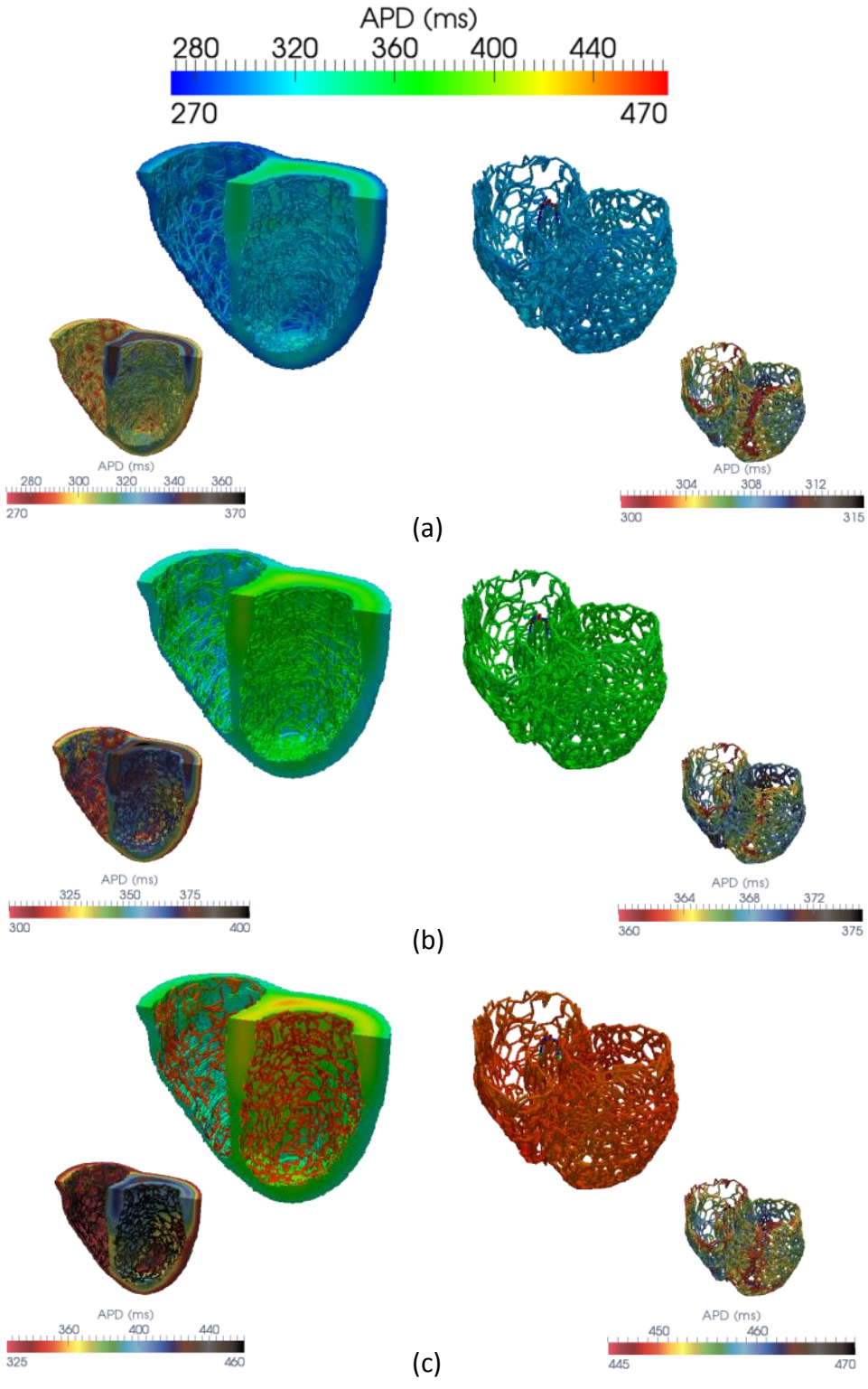

Figure 50. APD maps of posterior view along with the CCS for different doses of dofetilide showing that I_{kr} block increases the duration of the AP. Larger size figures have a common APD colormap range, while others have their own colormap range. Dofetilide doses applied were (a) D=0 nM, (b) D=10 nM, (c) D=100 nM. Color indicates the duration of the AP in ms.

E- ORGAN LEVEL

In order to analyze results at organ level, we obtained APD dispersion plots and pseudo-ECGs in the precordial leads for each simulation. APD dispersion is expected due to the different electrical properties of endocardial, mid-myocardial and epicardial cells that have been modeled. These measurements integrate information of the whole organ, which due to the multi-scale effect should correlate with data obtained at cellular and tissue level.

Figure 51 (a) and (b) present changes in dispersion of APD for different I_{Kr} block scenarios in simulations with and without the PK network. Main differences are observed in normal case and D=100 nM. A two-peak morphology in the APD dispersion is observed in all cases without PK (see Figure 51 (a)), and only in D=10 nM with PK (Figure 51 (b)). This morphology correlates to the mean values of APD90 obtained for each cell type (see Table 4) and the percentage of each cell type population in the ventricular model. The first peak is attributed to EPI cells, which have the lower APD90 mean and a presence of 42% in the ventricular model, while the second peak corresponds to M cells, which has the largest mean value of APD90 and accounts for 41% of the ventricular model. Intermediate values are associated with ENDO cells. When there is presence of PK cells (see Figure 51(b)) the APD dispersion undergoes considerable changes in normal case and D=100 nM. In normal case we observed one-peak morphology where most APD90 values are concentrated near 300 ms, since there are no large differences between APD90 mean values of EPI and, even less between ENDO and PK cells. We observed a slight increase about 325 ms that corresponds to the presence of M cells, but this peak is smoothed due to the similarities in APD90 between the rest of cell types and their percentage in the model. For D=100 nM, the main difference is the third peak that appears at the end of the plot (highest APD90 values), which is explained by the larger APD prolongation in PK cells when blocking I_{Kr}. The APD dispersion morphology for D=10 nM shows only two-peaks since mean APD90 value for PK cells in this case is similar to the one measured for M cells.

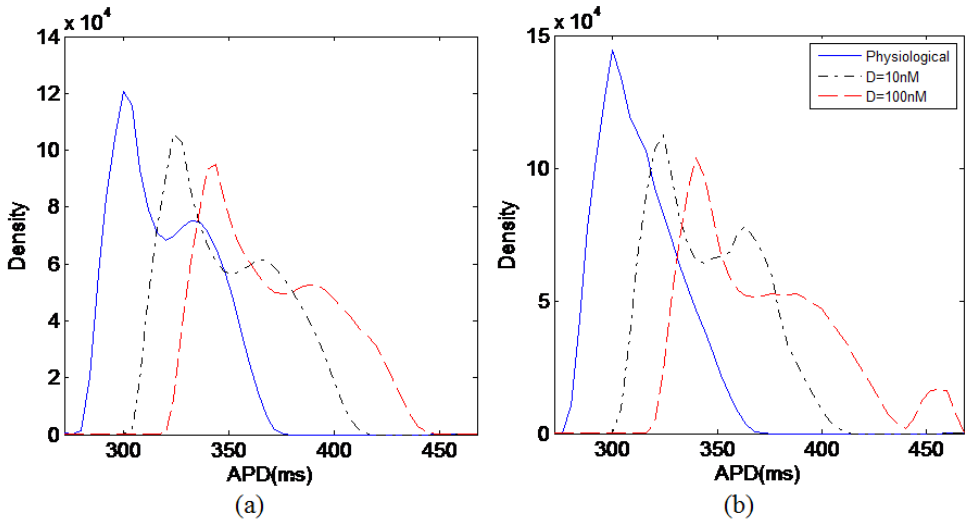

Figure 51. Different behavior of epicardial, endocardial and mid-myocardial cell types. APD dispersion as a function of the dofetilide concentration for (a) ventricular model without the CCS and (b) ventricular model including the CCS.

Pseudo-ECGs were calculate at the six precordial leads (see Figure 27), and were consistent with results obtained at cellular level. The QT interval is defined as the time duration between the onset of the QRS complex and the end of the T wave as it returns to baseline, ideally measured using either lead II or lead V5 of the 12-lead ECG [69]. In this case, we measured the QT interval using lead V5 and defining a common criterion for all the simulations (QT99). We defined the end of the QT interval as the instant were the maximum of the T-wave decreases a 99%. Normal QT values are generally considered to be between 350 and 440 ms [70].

A QT interval of 425 ms was measured under normal conditions in simulations without the CCS, which was in the normal range although near the maximum normal value, probably due to a slow activation time. QT interval measured in simulations with the CCS was shorter, 402 ms, since there is a much higher number of PMJs and activation is faster in this case. Prolongation of QT after dofetilide release is larger in simulations which include the CCS, especially for total I_{kr} block, i.e. D=100 nM. This block (D=100 nM) increases the QT interval up to 75 ms in lead V5 for simulations without the CCS and up to 100 ms when the model includes the CCS. Results in simulations without the CCS are consistent with results obtained by Ten-Tusscher [58] at cellular level. The increase of QT interval (9.65/16.71% without CCS and 11.94%/23.88% with CCS for D=10 nM/D=100 nM) is in agreement to clinical recordings that show the degree of QT prolongation induced by the effect of dofetilide (15.4% ± 6.7%) [71].

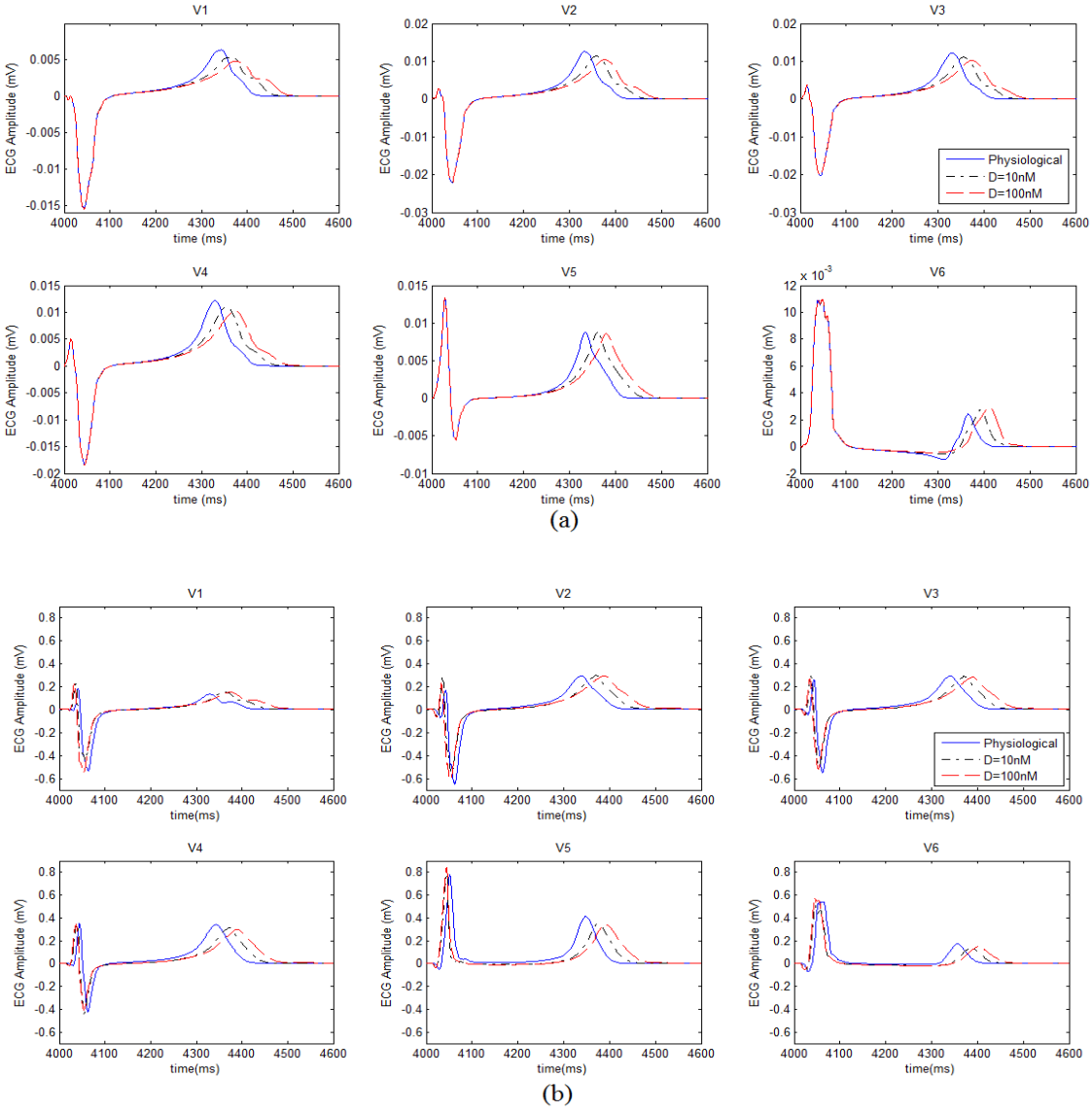

Figure 52. Simulated pseudo-ECGs in the precordial leads for different doses of dofetilide obtained with (a) the ventricular model without the CCS and (b) the ventricular model including the CCS

Is also remarkable that amplitude of pseudo-ECGs obtained when adding the CCS is in the range of millivolts (see Figure 52 (b)), which is the normal range of amplitude values, while the amplitude obtained in the model without the CCS is in the order of microvolts (Figure 52 (a)).This difference might be due to the different number of PMJs used (stimuli nodes) in each model.

Finally, Table 4 summarizes all the results presented in chapters 5 D- and 5E- quantitatively.

Table 4. Differences in activation times, mean APD90, APD prolongation, QT interval and QT interval prolongation in simulations with and without the CCS.

DOFETILIDE		0nM		10nM		100nM	
		Without PK	With PK	Without PK	With PK	Without PK	With PK
Activation (ms)		88	76	88	74	88	76
APD90 mean (ms)	**ENDO**	320.83	309.84	350.71	344.17	372.71	371.86
	M	337.04	328.82	370.45	364.75	395.25	391.42
	EPI	301.78	298.08	328.12	324.11	347.19	343.23
	PK	-	306.71	-	369.20	-	456.53
ΔAPD90 mean (%)	**ENDO**	-	-	9.31	11.08	16.17	20.02
	M	-	-	9.91	10.93	17.27	19.04
	EPI	-	-	8.72	8.73	15.05	15.15
	PK	-	-	-	20.37	-	48.79
QT99 (ms)		425	402	466	450	496	498
ΔQT99 (%)		-		9.65	11.94	16.71	23.88

6. DISCUSSION

A- MULTI-SCALE RESULTS

In this study we have built a computational model of the human heart ventricles and carried out electrophysiology simulations to elucidate the effect of key ventricular structures such as the CCS in the presence of a drug called dofetilide. We compare it with a configuration in which the CCS was reduced to a set of scattered stimuli on the endocardium.

Due to the lack of knowledge regarding the conduction system several models of the CCS with diverse configurations of the HB and characteristics of the distal section (for each ventricle: number of nodes of the network, radius of neighbors searching, starting nodes of growing of the network, regions with higher density of PMJs, probabilities of forming "looping" structures and of defining intermediate PMJs nodes) have been modeled and simulated.

We have found out that the configuration of the HB is critical in order to obtain a correct sequence of activation and properly shaped pseudo-ECGs. Among the configurations of the HB, the one that included more anatomical details from an anatomical study [12] does not produce the expected results regarding ventricles activation and synchronization, giving as a result an incorrect morphology in pseudo-ECGs calculated in the six precordial leads. Better results were obtained with a simpler HB configuration, and this was the critical point to decide the final HB configuration and the PK network used for the complete set of simulations with dofetilide.

We create PK networks with higher number of nodes in LV, considering studies and information by the cardiac anatomist Damián Sánchez-Quintana, who in addition affirms that the number of PMJs is higher in the LV than in the RV. In addition, we observed that pseudo-ECG morphology and amplitude was not significantly modified when varying the number of nodes of the network in each ventricle. Similar pseudo-ECGs were obtained for a PK network with 1500 nodes in the RV and 3000 in the LV, and a PK network with exactly half of them. This indicates that there are a number of terminals from which activation does not change its pattern.

Other parameters, like the radius of neighbors searching, the probability of forming "loops" and the probability of defining extra PMJs from intermediate nodes of the network were chosen mainly to fully cover the endocardium and to get PK branches in the order of millimeters. In the future we will perform a complete sensibility analysis of the model parameters, in order to study how much they affect the results.

Modeling and adding the CCS to the ventricular model improves considerably the activation time. In this case, we obtain an activation time of 76 ms, so activation is faster and in the range of normal activation values reported by Durrer [1]. Nevertheless, we have to consider that obtaining a faster activation time in this case is also due to the higher

number of PMJs, because the ventricular model with scattered activation points has just 100 activation points in the RV and 150 in the LV. The conductivity in PK cells was adjusted to obtain a conduction velocity in the range of 2-3 m/s.

Multi-scale qualitative analysis of the results is consistent with experimental data in both models. From cell to organ level, we observe the effects of blocking I_{Kr} by the effect of dofetilide as i) an APD prolongation in every type of cell (observe in APD90 plots and isochronal APD90 maps), ii) no variation in the activation time and pattern (in isochronal activation time maps) and iii) prolongation of the repolarization time and of the QT interval.

When plotting AP for the different type of cells, i.e. extracting voltage data from a random point of each region, we observed that the typical spike-and-dome configuration of M and EPI cells was not visible. This result is probably due to both the coupling between cells and the temporal resolution used in our simulations. In fact, comparing this observation with results reported by Decker [72] points to this conclusion. Decker shows simulated APs for epicardial dog cells and tissue and reports experimental results from other researchers, showing that at one-dimensional tissue level the spike-and-dome morphology is preserved but smoothed. Probably the absence of the spike-and-dome in M and EPI cells in our simulations is caused by the two-dimensional coupling.

We also noted that PK cells interact with the ventricular model incrementing the APD90 prolongation in a major degree for surrounding cells (ENDO, followed by M and finally EPI cells). Stewart did not presented in his paper on the PK cell modeling [56] quantitative results for the APD90 when blocking I_{Kr}. However, our simulations shown that APD90 of PK cells is highly prolonged when blocking $I_{Kr,}$ which is consistent with experimental results [67].

It is not possible to compare overall activation patterns observed in simulations with experimental data. The reference studies in this sense are those by Durrer [1], but his results show a high variability in the epicardial activation pattern and there is just one example of the endocardial activation pattern. The endo-to-epi activation pattern visible in Durrer's maps is well reproduced by our simulations with the CCS, while the apex-to-base activation pattern is better reproduced by the simulation without the CCS, because activation points were distributed to obtain this pattern. However, activation times between simulations and Durrer measurements are comparable.

Isochronal APD90 maps show that its heterogeneity principally depends on the distribution of the different cell types. Our simulations, with and without CCS, have the same cell distribution (ENDO, M, EPI) in the ventricles and this is visible comparing APD90 maps. These maps are very similar in simulations with and without PK system for the same scenario (D=0 nM, D=10 nM and D=100 nM). I_{Kr} block in the presence of PK fibers has an effect in the prolongation of APD90, but do not modify the APD90 pattern comparing APD90 maps between models for each dofetilide dose (see Figure 47 right and Figure 50 left).

APD90 dispersion plots show a similar morphology for each dose of dofetilide, having two-peak morphology in simulations without PK fibers. This morphology is not observed in simulations with PK fibers. APD90 values of PK cells are similar to APD90 values of ENDO, M and EPI cells in simulations for physiological conditions. For D=100 nM the pronounced prolongation of APD90 in PK cells causes a third peak. In addition, plotting of APD dispersion for the 5 simulated consecutive pulses clearly shows the necessity of stabilizing the model and suggests that PK cell model needs a larger number of pulses to reach the steady-state.

The morphology of the calculated pseudo-ECGs was correct for both sets of simulations, while the amplitude was in the normal scale of millivolts for simulations including the CCS. Measurement of QT interval gave a value in the normal range in both simulations for the control conditions and was shorter for the simulation including the CCS due to its faster activation. QT prolongation was in the range measured by Okada [71], although it is significantly higher in simulations including the PK fibers.

A complete sensibility analysis of the configuration of the HB and its proximal bundles is still needed in order to obtain a more realistic morphology and amplitude in the simulated pseudo-ECGs.

B- LIMITATIONS

First, we want to mention limitations associated with the main part of this work, which is the development of an anatomical model of the CCS. Main limitations are due to limited available data. The PK network is a certainly unknown anatomical structure, especially in humans. There is no consistent anatomical data available, so its modeling is principally based in observations done in animal hearts and oriented to obtaining adequate simulation results (activation maps, APD maps, pseudo-ECGs). It is not possible to know how much real the created PK network is, and even to know if a more realistic network would give better results. In fact, as we have seen in this study, the more anatomically detailed HB that we created do not obtain better results in the activation sequence and pseudo-ECGs.

Parameters used for creating networks were tested observing the results of electrophysiology simulations and were not based in anatomical studies, although we limited some parameters such as the radius of neighbors searching and create “looping” structures to reproduce the PK structure observed in animal hearts (dog and calf). There is no information on the real number of PMJs in human hearts, so this number has also been established observing the results of test simulations.

The CCS model has been added to a ventricular model which considers transmural heterogeneities (M, ENDO and EPI cells), but not variations in ionic currents from apex-to-base. The anatomical models of the ventricles and the CCS have been associated to cellular models. In this case, simulations have been done with the model of Ten-Tusscher [58] for ventricular cells and the model of Stewart for PK cells [56]. Consequently, there

are limitations inherent to the use of these cellular models, which are greatly conditioned by the limited availability of data, the variability of data and experimental conditions and the potential deleterious effects of cell isolation.

For example, Stewart model of PK fibers is based on modifications of the Ten-Tusscher ventricular cell model taking into account experimental data of hearts affected by heart-failure [59]. Several assumptions have to be done to develop the model, as considering that heart-failure ion channel remodeling in PK fibers is consistent with remodeling in ventricular myocytes in order to adjust some channel parameters to reproduce a normal PK cell model. Due to the mathematical models used differences in APD90 between the different types of cells, especially when comparing PK cells with ventricular cells, are not what experimental studies mention. APD90 in the PK cell model does not have a larger value than APD90 in ventricular cells. Ten-Tusscher values for APD90 [57, 58] are 282 ms for ENDO cells, 336 ms for M cells and 306 ms for EPI cells at BCL=1000 ms, while the computed value of PK cell model of Stewart [56] is 293 ms (lower than experimental APD90), which is shorter than the computed APD90 for M and EPI cells. Differences in APD90 between ventricular cells are lower than differences observed experimentally. However, when blocking I_{Kr} the APD90 of PK cells overcomes APD90 of ventricular cells since its prolongation is more pronounced. In addition, Ten-Tusscher model for ventricular cells has an inaccurate behavior when blocking I_{Kr} or I_{Ks}.

Furthermore, the model of dofetilide that has been used in these simulations is also very simple. We have applied a factor multiplying $I_{Kr,}$ current. This factor is inversely related to the dose of dofetilide. Other simplification that has been assumed is the application of the same blocking factor in PK cells than in ventricular cells, although it is not clear if the effect of dofetilide is equivalent for this cell type.

At organ level, we have obtained pseudo-ECGs, which are comparable with real ECGs in morphology but not in amplitude. To obtain simulated ECGs it is necessary to introduce the heart model in a complete torso model, taking into account different tissue heterogeneities between the heart and the torso.

There are also computational limitations. We have simulated 5 stimuli with a BCL=1000 ms (a total of 5000 ms). Approximately 24 hours have been necessary to perform every simulation using 48 cores. Therefore, it is not possible to launch the number of stimuli probably needed to stabilize the model (maybe 1000 stimuli).

Finally, it is difficult to validate cell and tissue results with experimental data, especially for PK cells, and quantitative comparisons are limited by the lack of experimental values and its variability. There are also difficulties for validating these results at organ level (by pseudo-ECGs), cause there are no much experimental studies. In addition, it is obvious that this kind of studies cannot be tested in-vivo because it would be highly invasive and it is not ethical to administrate dofetilide or other drugs to test their effect.

7. CONCLUSIONS

We have modeled several configurations of the HB and PK networks, which have been incorporated in a 3D model of a human subject including the main anatomical and functional components required to perform in-silico electrophysiology studies.

Results of simulations with different models of the CCS were tested, showing that the configuration of the HB and its proximal branches is critical in order to obtain right activation patterns and simulated pseudo-ECGs. Surprisingly, better results were obtained with simpler HB models, than with the most anatomically detailed one.

We designed a simulation study to analyze the multi-scale effects of drug-induced ion channel block in ventricular electrophysiology at the cellular, tissue and whole ventricular levels for two different models, one of them programming activation with scattered activation points and the other including a model for the specialized cardiac conduction system. A well-known drug called dofetilide which affects specifically I_{Kr} channels was chosen to study the effect of current block in these 3D heart models. Results showed the effect of dofetilide in cardiac cells, as a prolongation of APD and QT in both models. Average APD as well as APD distributions were obtained for each drug concentration in each model. The model including the CCS produced the more realistic results in activation times. The presence of PK cells has effects over the APD90 of ventricular cells increasing their original values. Pseudo-ECGs confirmed the results observed at cellular level regarding the prolongation of repolarization phase. QT prolongation was significantly higher when including PK fibers, but was also in the range of experimental results.

Incorporating a model of the specialized cardiac conduction system introduces new possibilities in simulation studies. Particularly, it allows studying the role of this system in normal and abnormal activation of the ventricles. Cardiac diseases as left or right bundle branch block and other abnormalities involving the CCS (micro-reentry, abnormal automaticity, triggered activity, etc. and their influence in tachyarrhythmia) can be simulated and analyzed. These studies can contribute to a better knowledge of cardiac diseases and, therefore, to the development of new strategies for their treatment.

Results confirmed the importance of structural personalization since the response to the drug block varies as a function of the cell type. In contrast to the configuration of the HB, the overall ventricular geometry should not have a great impact on the results or the effects of the drug. Nonetheless, differentiated models for dilated, normal or hypertrophied hearts might have an impact. Computational modeling and simulation tools might help in the understanding of complex drug to cell and organ interactions, as well as help for the assessment of drug safety pharmacology.

8. APPENDIX

A- ANATOMY OF THE HEART

The heart is located in the torso, between the lungs and behind the sternum and the diaphragm (see Figure 53). Over the heart are the superior and inferior vena cava, the pulmonary artery and the aorta. The heart has four chambers: right and left atria, and right and left ventricles. The atria form a unit and the ventricles another, a fact particularly important for the electrical function of the heart, described below.

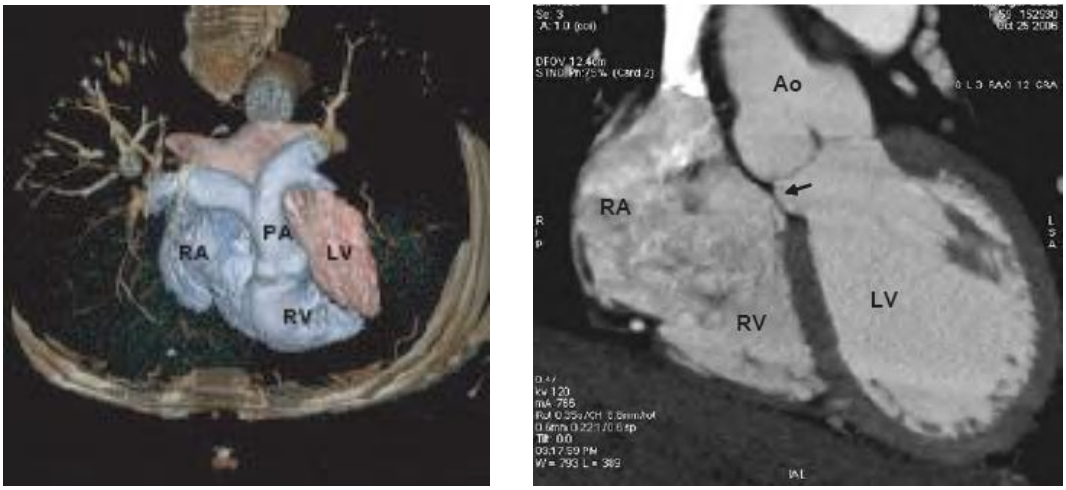

Figure 53. (a) 3D volume rendering from CT and (b) multiplanar reconstruction. An oblique view aims to visualize the membranous septum (arrow). RA = right atrium; RV = right ventricle; Ao = aorta; LV = left ventricle.

In a normal heart there are four valves. Atrio-ventricular valves (tricuspid and mitral) separate atria from ventricles, while semilunar valves (pulmonary and aortic) separate ventricles from the main arteries. The surface of these valves and the internal surface of the chambers are covered by a single layer of cells which form the endocardium. The mid-myocardium is the thickest layer and it is formed by several layers of muscular cells. The most external layer is called epicardium.

Several terms are used to describe the different heart surfaces. The apex is formed by the inferior wall of the LV. The posterior wall is formed by atria, specially the left atria. Right atria and ventricle form the anterior wall. The inferior face is formed by both ventricles. Figure 54 shows the anatomy of the heart described here.

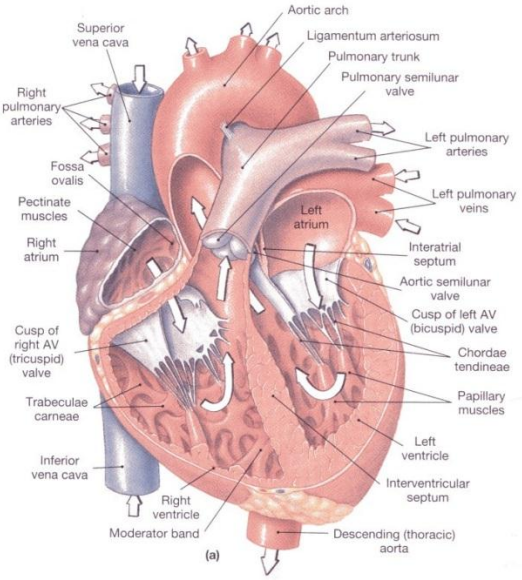

Figure 54. Anatomy of the heart and associated vessels

B- DIFFUSION TENSOR MAGNETIC RESONANCE (DTMRI)

Diffusion MRI is a magnetic resonance imaging (MRI) method that produces in vivo images of biological tissues weighted with the local microstructural characteristics of water diffusion. The field of diffusion MRI can be understood in terms of two distinct classes of application—diffusion weighted MRI and diffusion tensor MRI.

Diffusion tensor imaging (DTI) is important when a tissue—such as muscle fibers in the heart—has an internal fibrous structure analogous to the anisotropy of some crystals. Water will then diffuse more rapidly in the direction aligned with the internal structure, and more slowly as it moves perpendicular to the preferred direction. This also means that the measured rate of diffusion will differ depending on the direction from which an observer is looking. Traditionally, in diffusion-weighted imaging (DWI), three gradient-directions are applied, sufficient to estimate the trace of the diffusion tensor or 'average diffusivity', a putative measure of edema.

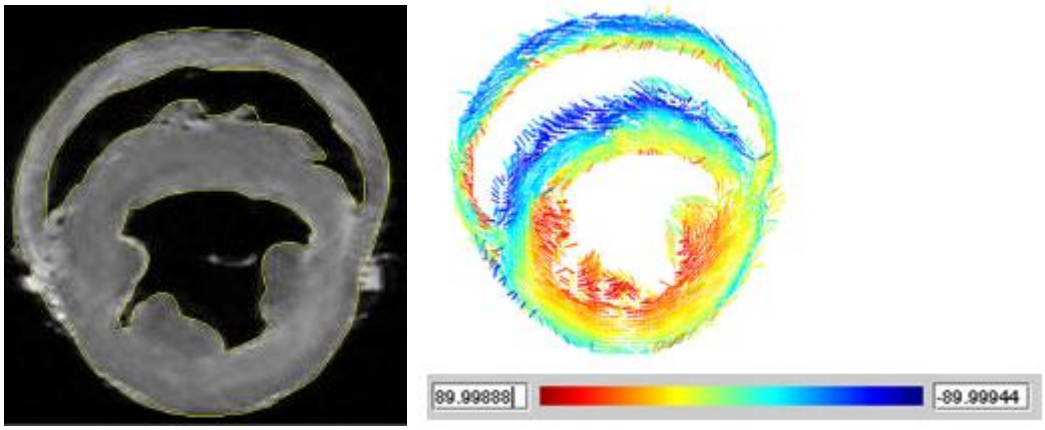

Figure 55. DTMRI short axis cut showing RV and LB. (a) Gray level image from DTI and (b) reconstruction of fiber orientation in plane.

C- COMPUTATIONAL SIMULATION

PRE-PROCESSED

The pre-processed is implemented in MATLAB. The previous step to execute the algorithm is to select endocardial nodes from those which form the whole ventricular model. After this selection, we run the algorithm that creates the PK network. In the execution we must specify the HB configuration that is used and the matrix of endocardial nodes from which PK network nodes are selected (whole endocardial, not nodes in the basal region…).

Before running the algorithm, we have to indicate the value of the following parameters for each ventricle: index of the nodes where the net starts its growing, distance that will be used to compute the searching radius, regions with predefined terminals (index of the central node, radius of the region and percentage of predefined terminals), probability of a intermediate node to be the origin of a little bundle ended in a terminal, probability of forming "elliptical structures" (it is related to the probability of connect again a node that is already connected with a neighbor).

After running the algorithm we indicate the number of nodes that will form the PK network in each ventricle. With these parameters, the algorithm computes the network and gives the next outputs:

1) .dat intermediate outputs:

- PKpoints_RV, PKpoints_LV: candidate node that form the PK network (its number is set by the user).
- endoRV, endoLV: final nodes of the PK network in each ventricle. Composed of PKpoints plus the additional nodes that the algorithm may define as terminals.

- conneRV, conneLV: connectivity between the nodes of the PK network (endoRV, endoLV) in each ventricle.
- hisnodes: nodes that form the HB.
- conneHis: connectivity between the nodes that form the HB.
- termiRV, termiLV: indices of terminal nodes (PMJs) in each ventricle.

2) .dat final outputs (inputs for EMOS processed):

- CS2H05_nod_PK: specifies the PK network nodes.
- CS2H05_elm_PK: specifies the PK network elements.
- nodesPK_vsim: nodes for the whole ventricular simulation, including the CCS.
- elemPK_vsim: elements for the whole ventricular simulation, including the CCS.
- elemPKTer_vsim: elements indicating PK network terminals (PMJs).

PROCESSED (EMOS)

To compute the results of simulation of the CCS in the ventricular model we used a solver called EMOS [52].

EMOS is a finite element solver to compute the resolution of the monodomain equation based in the technique of operator splitting. It allows parallelization to optimize the computational efficiency by using METIS libraries to divide the domain and uses PSBLAS libraries to solve the linear systems. Integration of temporal equations is compute semi-implicitly (implicit to parabolic equation and explicit to ionic equations) or explicitly. Several types of elements can be used (linear, triangular, quadrilateral, tetrahedrons and hexahedrons) and it is possible to work with meshes with different types of elements. The electrical models that are support by EMOS are:

1) Roger and McCulloch (phenomenological)
2) Bueno-Orovio (modification of Fenton-Karma model, phenomenological)
3) Luo-Rudy (guinea pig ventricles)
4) Ten-Tusscher (human ventricles)
5) Nygren (human atria)
6) Stewart (human PK cell)
7) Grandi (human ventricle)

There are some common .dat files that are used for running the simulation process:

- CS2H05_PK: specifies the model geometry and analysis conditions.
- CS2H05_stm: specifies the stimulus that is applied to the system to perform the simulation.
- CS2H05_pel_PK: specifies the cellular models that are used and nodal properties as fiber direction.

Figure 28 shows CS2H05_PK.dat file, that is the file which contains specifications of the model geometry and the simulation analysis that is perform.

GEOMETRY

-*analysistype* label, value 1 indicates an electrophysiological analysis.

-*material*. As is indicate, we use three materials. The first column is the number of the material, the three following columns are not used and the fourth column indicates the number of data that define the corresponding material. There are three data (longitudinal conductance, ratio between transversal en longitudinal conductance, and capacitance) for myocardial and PK materials, and one data (longitudinal conductance) for the Purkinje-muscle junction. PK longitudinal conductance has been set to 0.180, giving this value a conduction velocity of 2.68 m/s in the PK network.

-*prop_nod*, specifies the type of the cellular model that is used in each node. In these simulations, there are four types of nodal properties. The first column refers to the number of the property and the second column refers to the type of property that is pointed. The third column is always 1 in electrophysiological simulations, indicating the number of integer data to be defined. The fourth column is the number of real data to be defined, that is 0 in our case. The last column is the integer defined data and indicates the cellular type: 1, 2 and 3 are endo, mid and epi cellular Ten-Tusscher models and 11 indicates PK cell Stewart model.

-*prop_elem* loads a file that contains fiber direction of each element.

-*nodes* loads a file containing all the nodes of the PK network. The first line indicates the total number of nodes, its type (this value is not used) and its dimension (3D in this case). The second line indicates the number of nodes to be defined. Following rows indicate for each node its identification number, its nodal property (associated cellular model) and nodal coordinates (x,y,z). An extract of a nodal file example is shown in Figure 56.

```
1467112 1 3
1467112 NODETYPE
      1    3  4.450000  5.550000  0.100000
      2    3  4.500000  5.550000  0.100000
      3    3  4.500000  5.600000  0.100000
      4    3  4.450000  5.600000  0.100000

                      ...
1467106    4  4.525000  4.675000  5.850000
1467107    4  5.525000  1.475000  5.900000
1467108    4  2.875000  6.225000  5.950000
1467109    4  4.025000  5.100000  6.025000
```

Figure 56. File #NODES in CS2H05_PK.dat

-*elements* loads a file containing elemental connectivity and elemental properties. The first line indicates the total number of elements and the number of element types of the file. In the second line it is shown the total of elements of the first type and its type. In the case of the example Figure 57 there are 1289030 elements of type HT3DH08 (trilinear hexahedra, 8 nodes), 34389 elements of type HT3DL02 (1D element in a 3D space, linear, 2 nodes) that is used to define PK trees, and 2388 elements of type HT0DC (connection elements, 0D). For each element it is specified its identification number, its elemental property and the nodes that composed its elemental connectivity.

```
1325807 3
1289030 HT3DH08
      1       1       1       2       3       4       5       6       7       8
      2       2       2       9      10       3       6      11      12       7
      3       3       9      13      14      10      11      15      16      12
      4       4      13      17      18      14      15      19      20      16
                                        ...
1289028 1289028 1419845 1419846 1419859 1419860 1434112 1434113 1434126 1434127
1289029 1289029 1419846 1419847 1419861 1419859 1434113 1434114 1434128 1434126
1289030 1289030 1419847 1419848 1419862 1419861 1434114 1434115 1434129 1434128
  34389 HT3DL02
1289031 1289031 1434130 1436250
1289032 1289031 1434131 1436255
1289033 1289031 1434131 1436261
                  ...
1323418 1289031 1467111 1436248
1323419 1289031 1467112 1436249
   2388 HT0DC
1323420 1289032 1434160   23275
1323421 1289032 1434160   23276
1323422 1289032 1434160   23341
1323423 1289032 1434160   23342
                  ...
1325806 1289032 1436249  784359
1325807 1289032 1436249  784360
```

Figure 57. File #ELEMENTS in CS2H05_PK.dat

ANALYSIS

-*step*, describes the type of the analysis that is executed.

-*restart*, depending on its value, a binary file is generated with data needed to continue the simulation from a particular time instant. Potentials and variables of the electrical model are saved for that time. In this case, *restart, -1* indicates the no restart binary file is created.

-*param_node* specifies nodal parameters that are used in the calculation. It is used, for example, to specify masks that are used to change parameters in the electrical model in some specific regions, i.e., for simulating pathologies like ischemia. At the moment, this parameter is not used in our simulations.

-*param_elem*, is the same as *param_node* but it works with elements. It is used when the calculation is done using bubble functions. At the moment, this parameter is not used in our simulations.

-*integ_scheme*, indicates the scheme of temporal integration that is used in the calculations. It can take different values: 0, explicit integration without temporal optimization; 1, explicit integration with temporal optimization; 2, implicit integration without temporal optimization; 3, explicit integration with temporal optimization. In our simulations we have used the integration scheme 3.

-*solver*, indicates the type of solver to use with PSBLAS libraries. It can be: 1, conjugate gradient method; 2, conjugate gradient stabilized method; 3, bi-conjugate gradient method; 4, bi-conjugate gradient stabilized method; 5, bi-conjugate gradient stabilized method with restarting; 6, generalized minimal residual method with restarting. We have used the conjugate gradient method.

-*time_inc*, indicates the time step, the maximum time of simulation and the maximum number of iterations. The example (Figure 28) indicates a simulation with the same initial and minimal time step (0.02) and a simulation time of 600.00ms. The last two values, that indicate the maximum time step and the maximum number of iterations in non-linear problems, are not used.

-*stimulus* loads a file with the sequence of stimulation and the nodes to be stimulated. The first line indicates the number of stimuli sequences (Figure 58). The second line identifies the stimuli sequence (1), the number of stimuli in that sequence (1) and the characteristics of the stimuli: time of application (0.0 ms), duration (2.0 ms) and amplitude (850.00 nA). The third line indicates the number of nodes to be stimulated (1) and the fourth indicates the stimulated node (1434130) and the stimuli sequence to apply (1).

```
      1   !.number of stimuly histories;   {id_stm, nr of stm, 3*[t_ini, duration, current]}
      1    1    0.0  2.0  850.0
      1    0
1434130    1
```

Figure 58. File #STIMULUS in CS2H05_PK.dat

-*nodeoutput* and *elemouput*, specify the nodes and the frequency of saving results at nodal and element levels. If there are not specifications, all variables of the electrical model are saved for each node and each element in electrophysiological simulations.

-*g_output*, indicates the variables that are written for all the model and its frequency. This data is used to generate visualization files in VTK or Ensight format. The first line indicates the number of variables to specify and the second line indicates the output

variable (2 indicates potential, it generates binary files to calculate pseudo-ECG and visualization files) and the frequency in which results are saved.

To run a simulation using parallelization technique, it is necessary to indicate the nodes of the cluster that will be used in the calculation and the number of cores that will take part in each node. This is done in the "machines" file. As an example, if the simulation is run in nodes 26, 27, 28 with 8 cores in each one, machines file will be:

```
nodo26:8
nodo27:8
nodo28:8
```

Then we have to create the ring of cores to perform the simulation:

```
mpdboot –n 3 – f machines
```

where 3 indicates the number of nodes that take part in the ring and machines specifies the file that include the computational ring properties.

Supposing that the CS2H05_PK.dat file is in the path /vdisk1/Simulations/data/24Nov2010 and that the directory in which we want to save the ouputs is /vdisk1/Simulations/post/24Nov2010, the order to execute the simulation in this example will be:

```
./runelv 24 /data/24Nov2010/CS2H05_PK.dat post/24Nov2010/PK_24Nov_
```

Being /vdisk1/Simulations the actual path. 24 is the total number of cores, CS2H05_PK.dat is the simulation file and post/24Nov2010/PK_24Nov_ indicates the output directory and the common part of the name of the output binary files.

The result of the execution is a total of 24 binary files (one file for each processor) in the /post/24Nov2010/. These files contain the results that can be post-processed in order to generate the VTK or Ensight outputs and the pseudo-ECG .dat files.

POST-PROCESSED

EMOSpost is a Fortran code for postprocessing the binary output generated by EMOS during execution. It generates output files in VTK format and also output files for Ensight format that can be visualized with the free visualization software ParaView. The basic capabilities of EMOSpost are:

1) Generation of transmembrane potential maps
2) Generation of activation time maps (isochrones)
3) Generation of APD maps
4) Compute pseudo-ECG or electrograms

In the present work we have used all of these capabilities. As an example, we show the post_config.dat file that is used to generate the outputs (Figure 59):

```
#NODEFILE
CS2H05_nod_PK.dat
#ELEMFILE
CS2H05_elm_PK.dat
#FIBERFILE
CS2H05_pel_PK.dat
#POTENFILE
24
PK_24Nov_ecg_prc_0.bin
PK_24Nov_ecg_prc_1.bin
PK_24Nov_ecg_prc_2.bin
          ...
PK_24Nov_ecg_prc_20.bin
PK_24Nov_ecg_prc_21.bin
PK_24Nov_ecg_prc_22.bin
PK_24Nov_ecg_prc_23.bin
#POSTFILENAME
PK_24Nov_
#FILETYPE
1         (1 Ens, 2 VTK)
#POTENTIAL
50 250 (f1, freq data is saved) (f2, freq data is postproc.)(f2>=f1)
#ISOCHRONE
1
0.0 290.0
#APD
1
0.0 590.0
#ECGPOINT
6
 1.43    -3.47    -0.54
 3.52     0.27    -2.58
 2.64     2.18    -4.19
 2.83     5.76    -5.29
 7.58    14.48    -1.73
11.34    17.60     5.58
#END
```

Figure 59. Post_config.dat file

The first loaded files in post_config.dat are those corresponding to the model geometry using the same format as the one used by EMOS: nodal coordinates, element information and element properties information (element fiber direction).

-*Potenfile* indicates the binary files generated by EMOS during execution.

-*Postfilename* indicates the name of the output files of EMOSpost. Filetype indicates the format of the output that can be Ensight (compatible with the ParaView software) or VTK.

The post-process variables that can be obtained are:

-*Potential*, indicates that transmembrane potential maps will be post-processed by the code. We have to indicate the frequency at which the data has been saved during execution (f_1) and the frequency at which the transmembrane potential maps will be computed for

visualization (f_2), being $f_2 \geq f_1$. Transmembrane potential maps are generated at each node as a function of time.

-*Isochrone*, indicates that isochrones maps will be post-processed by the code. The first line data line indicates the number of isochrones maps to be generated and the remaining lines are composed by an initial time instant and a final time instant, indicating the beginning and end of the time window in which the isochrones map will be generated. The code considers a cell has activated if the transmembrane potential, V_m, is greater than zero.

-*APD*, indicates that APD_{90} maps will be post-processed by the code. The first data line indicates the number of APD maps to be generated and the remaining lines indicate the time window in which APD maps will be generated. APD_{90} is computed as the elapsed time between the maximum upstroke and when $V_m=0.9\cdot(V_{max}-V_{rest})$, where V_{max} is the maximum of the AP of the cell and V_{rest} is potential reached by the cell at rest (without being stimulated).

-*ECGPOINT*, indicates that pseudo-ECGs will be computed at the given points. The first data line indicates the number of points in which the pseudo-ECG will be computed and the remaining lines indicate the global Cartesian coordinates X,Y,Z of the point where the pseudo-ECG will be computed.

Following the example of the PROCESSED paragraph, the order to obtain the processed files would be:

```
./runpost        data/24Nov2010/post_config.dat        post/24Nov2010/
```

9. BIBLIOGRAPHY

1. D. Durrer, R. Van Dam, G. Freud et al., "Total excitaton of the Isolated Human Heart." *Circulation* vol. 41, pp. 899-912. 1970.

2. A. Pollard and R. Barr, "Computer Simulations of Activation in an Anatomically Based Model of the Human Ventricular Conduction System." *IEEE Transactions on Biomedical Engineering* vol. 38 no. 10, pp. 982-996. 1991.

3. K. Ten Tusscher and A. Panfilov, "Modelling of the ventricular conduction system." *Progress in Biophysics and Molecular Biology* vol. 96, pp. 152-170. 2008.

4. R. Myerburg, K. Nilsson, and H. Gelband, "Physiology of Canine Intraventricular Conduction and Endocardial Excitation." *Circulation Research* vol. XXX, pp. 217-243. Feb. 1972.

5. C. Ramanathan, P. Jia, R. Ghanem et al., "Activation and repolarization of the normal human heart under complete physiological conditions." *Proceedings of the National Academy of Sciences of the United States of America* vol. 103 no. 16, pp. 6309-6314. Apr. 2006.

6. J. Purkinje, " Mikroskopisch-neurologische Beobachtungen." *Archiv für Anatomie, Physiologie and wissenschaftliche Medicin* vol. 12, pp. 281-295. 1845.

7. S. Tawara, *The Conduction System of the Mammalian Heart. An Anatomico-histological Study of the Atrioventricular Bundle and the Purkinje Fibers*: Cardiopulmonary Medicine from Imperial College Press, 1906.

8. W. Einthoven, "Weiteres über das Elektrokardiogran." *Pflüger Archiv Ges Physiol* vol. 122, pp. 517-548. 1908.

9. L. Aschoff, "Referat uber die Herzstorungen in ihren Beziehungen zu den Spezifischen Muskelsystem des Herzens." *Verh Dtsch Pathol Ges* vol. 14, pp. 3-35. 1910.

10. J. Mönckeberg, "Beitrage zur normalen und pathologischen Anatomie des Herzens." *Verh Dtsch Pathol Ges* vol. 14, pp. 64-71. 1910.

11. R. Anderson and S. Yen Ho, "The morphology of the cardiac conduction system." *Development of Cardiac Conduction System*. pp. 18-36. 2003. Novartis Foundation Symposium no 250.

12. G. Massing and T. James, "Anatomical configuration of the His bundle and bundle branches in the human heart." *Circulation* vol. 53 no. 4. 1976.

13. D. Sánchez-Quintana and S. Yen Ho, "Anatomía de los nodos cardíacos y del sistema de conducción específico auriculoventricular." *Revista Española de Cardiología* vol. 56 no. 11. 2003.

14. M. Spach, S. Huang, and S. Amstrong, "Demonstration of Peripheral Conduction System in Human Hearts." *Circulation* vol. 28, pp. 333-338. 1963.

15. A. Ansari, S. Yen Ho, and R. Anderson, "Distribution of the Purkinje fibres in the sheep heart." *The Anatomical Record* vol. 254, pp. 92-97. 1999.

16. S. Ryu, S. Yamamoto, C. Andersen et al., "Intramural Purkinje cell network of sheep ventricles as the terminal pathway of conduction system." *The Anatomical Record* vol. 292 no. 1, pp. 12-22. Jan. 2009.

17. V. Christoffels and A. Moorman, "Development of the Cardiac Conduction System. Why are some regions of the heart more arrhythmogenic than others?" *Circulation: Arrhythmia and Electrophysiology* vol. 2 no. 2, pp. 195-207. Apr. 2009.

18. O. Eliska, "Purkinje fibers of the Heart Conduction System." *Casopis Lékarú Ceských* vol. 145 no. 4. 2006.

19. A. Cates, W. Smith, R. Ideker et al., "Purkinje and ventricular contributions to endocardial activation sequence in perfused rabbit right ventricle." *American Journal of Physiology.Heart and Circulatory Physiology* vol. 281 no. 2, pp. 490-505. Aug. 2001.

20. A. Moorman, F. de Jong, M. Denyn et al., "Development of the Cardiac Conduction System." *Circulation Research* vol. 82, pp. 629-644. 1998.

21. D. Dosdall, K. Cheng, J. Huang et al., "Transmural and endocardial Purkinje activation in pigs before local myocardial activation after defibrillation shocks." *Heart Rhythm Society* vol. 4 no. 6, pp. 758-765. June 2007.

22. P. Tabereaux, G. Walcott, J. Rogers et al., "Activation patterns of Purkinje fibers during long-duration ventricular fibrillation in an isolated canine heart model." *Circulation* vol. 116 no. 10, pp. 1113-1119. Sept. 2007.

23. B. Baláti, A. Varro, and J. Papp, "Comparison of the cellular electrophysiological characteristics of canine left ventricular epicardium, M cells, endocarium and Purkinje fibers." *Acta Physiologica Scandinavica* vol. 164 no. 2, pp. 181-190. Oct. 1998.

24. A. Burashnikov and C. Antzelevitch, "Differences in the electrophysiologic response of four canine ventricular cell types to α_{1}- adrenergic agonists." *Cardiovascular Research* vol. 43, pp. 901-908. 1999.

25. G. Schram, M. Pourrier, P. Melnyk et al., "Differential distribution of cardiac ion channel expression as a basis for regional specialization in electrical function." *Circulation Research* vol. 90, pp. 939-950. 2002.

26. F. Persson, B. Andersson, G. Duker et al., "Functional effects of the late sodium current inhibition by AZD7009 and lidocaine in rabbit isolated atrial and ventricular tissue and Purkinje fibre." *European Journal of Pharmacology* vol. 558, pp. 133-143. 2007.

27. R. Robinson, P. Boyden, B. Hoffman et al., "Electrical restitution process in dispersed canine cardiac Purkinje and ventricular cells." *The American Journal of Physiology* vol. 253 no. H, pp. 1018-1025. 1987.

28. G. Tseng, R. Robinson, and B. Hoffman, "Passive properties and membrane currents of canine ventricular myocytes." *The Journal of Physiology* vol. 90, pp. 671-701. 1987.

29. A. Varro, B. Balati, N. Iost et al., "The role of the delayed rectifier component I_{Ks} in dog ventricular muscle and Purkinje fiber repolarization." *The Journal of Physiology* vol. 523, pp. 67-81. 2000.

30. W. Dun and P. Boyden, "The Purkinje Cell; 2008 style." *Journal of Molecular and Cellular Cardiology* vol. 45, pp. 617-624. 2008.

31. P. Boyden, M. Hirose, and W. Dun, "Cardiac Purkinje cells." *Heart Rhythm Society* vol. 7, pp. 127-135. 2010.

32. M. Vassalle, H. u, and I. Cohen, "The pacemaker current in cardiac Purkinje myocytes." *The Journal of General Physiology* vol. 106 no. 3, pp. 559-578. 1995.

33. E. Lakatta and D. DiFrancesco, "What keeps us ticking, a funny current, a calcium clock or both?" *Journal of Molecular and Cellular Cardiology* vol. 47 no. 2, pp. 157-170. 2009.

34. K. Dangman and D. Miura, "Does I_f control normal automatic rate in canine cardiac Purkinje fibres? Studies on the negative chronotropic effects of lidoflazine." *Journal of Cardiovascular Pharmacology* vol. 10 no. 3, pp. 332-340. 1987.

35. M. Vassalle, "The vicissitudes of the pacemaker current I_{Kdd} of cardiac Purkinje fibers." *Journal of Biomedical Science* vol. 14 no. 6, pp. 699-716. 2007.

36. M. Aoki, Y. Okamoto, T. Musha et al., "3-dimensional computer simulation of depolarization and repolarization processes in the myocardium." *Japanese Heart Journal* vol. 27 no. Suppl 1, pp. 225-234. Nov. 1986.

37. S. Abboud, O. Berenfeld, and D. Sadeh, "Simulation of high-resolution QRS complex using a ventricular model with a fractal conduction system. Effects of ischemia on high-frequency QRS potentials." *Circulation Research* vol. 68, pp. 1751-1760. 1991.

38. O. Berenfeld, D. Sadeh, and S. Abboud, "Modeling of the Heart's Ventricular Conduction System Using Fractal Geometry: Spectral Analysis of the QRS complex." *Annals of Biomedical Engineering* vol. 21, pp. 125-134. 1993.

39. A. Pollard and R. Barr, "The Construction of an Anatomically Based Model of the Human Ventricular Conduction System." *IEEE Transactions on Biomedical Engineering* vol. 37 no. 12, pp. 1173-1185. 1990.

40. O. Berenfeld and J. Jalife, "Purkinje-Muscle Reentry as a Mechanism of Polymorphic Ventricular Arrhytmias in a 3-Dimensional Model of the Ventricles." *Circulation Research* vol. 82, pp. 1063-1077. 1998.

41. K. Simelius, J. Nenonen, and B. Horacek, "Modeling Cardiac Ventricular Activation." *International Journal of Bioelectromagnetism* vol. 3 no. 2, pp. 51-58. 2001.

42. E. Vigmond and C. Clements, "Construction of a Computer Model to Investigate Sawtooth Effects in the Purkinje System." *IEEE Transactions on Biomedical Engineering* vol. 54 no. 3, pp. 389-399. 2007.

43. J. Malmivuo and R. Plonsey, *Bioelectromagnetism. Principles and Applications of Bioelectric and Biomagnetic Fields*: Oxford University Press, 1995.

44. A. Guyton and J. Hall, "Electrocardiograma normal." *Tratado de fisiología médica*. vol. 11 no. 11, pp. 123-130. 2006. Elservier España.

45. G. Lande, P. Maison-Blanche, J. Fayn et al., "Dynamic analysis of dofetilide-induced changes in ventricular repolarization." *Clinical Pharmacology and Therapeutics* vol. 64 no. 3, pp. 312-321. Sept. 1998.

46. P. Franzone, L. Guerri, and S. Tentoni, "Mathematical modeling of the excitation process in myocardial tissue: influence of fiber rotation on wavefront propagation and potential field." *Mathematical Biosciences* vol. 101 no. 2, pp. 155-235. Oct. 1990.

47. P. Franzone, L. Guerri, and B. Taccardi, "Spread of excitation in a myocardial volume: simulation studies in a model of anisotropic ventricular muscle activated by point stimulation." *Journal of Cardiovascular Electrophysiology* vol. 4 no. 2, pp. 144-160. Apr. 1993.

48. P. Franzone, L. Guerri, M. Pennachio et al., "Spread of excitation in 3-D models of the anisotropic cardiac tissue. II. Effects of fiber architecture and ventricular geometry." *Mathematical Biosciences* vol. 147 no. 2, pp. 131-171. Jan. 1998.

49. B. Taccardi, R. Lux, P. Ershler et al., "Anatomical architecture and electrical activity of the heart." *Acta Cardiologica* vol. 52 no. 2, pp. 91-105. 1997.

50. C. Henriquez, A. Muzikant, and C. Smoak, "Anisotropy, fiber curvature, and bath loading effects on activation in thin and thick cardiac tissue preparations: simulations in a three-dimensional bidomain model." *Journal of Cardiovascular Electrophysiology* vol. 7 no. 5, pp. 424-444. May 1996.

51. P. Helm, "A novel technique for quantifying variability of cardiac anatomy application to the dyssynchronous failing heart,", John Hopkins University, 2005.

52. E. Heidenreich, J. Ferrero, M. Doblaré et al., "Adaptive Macro Finite Elements for the Numerical Solution of Monodomain Equations in Cardiac Electrophysiology." *Annals of Biomedical Engineering* vol. 38 no. 7, pp. 2331-2345. 2010.

53. C. Antzelevitch, S. Sicouri, S. Litovsky et al., "Heterogeneity within the ventricular wall. Electrophysiology and pharmacology of epicardial, endocardial and m cells." *Circulation Research* vol. 69 no. 6, pp. 1427-1449. 1991.

54. E. Drouin, F. Charpentier, C. Gauthier et al., "Electrophysiologic characteristics of cells spanning the left ventricular wall of human heart: evidence for presence of m cells." *Journal of the American College of Cardiology* vol. 26 no. 1, pp. 185-192. 2005.

55. S. Sicouri, J. Fish, and C. Antzelevitch, "Distribution of m cells in the canine ventricle." *Journal of Cardiovascular Electrophysiology* vol. 5 no. 10, pp. 824-837. 1994.

56. P. Stewart, O. Aslanidi, D. Noble et al., "Mathematical models of the electrical action potential of Purkinje fibre cells." *Phylosophical Transactions of the Reyal Society A* vol. 367, pp. 2225-2255. 2009.

57. K. Ten Tusscher, D. Noble, P. Noble et al., "A model for human ventricular tissue." *American Journal of Physiology.Heart and Circulatory Physiology* vol. 286, pp. 1573-1589. 2004.

58. K. Ten Tusscher and A. Panfilov, "Alternans and spiral breakup in a human ventricular tissue model." *American Journal of Physiology.Heart and Circulatory Physiology* vol. 291, pp. 1088-1100. 2006.

59. W. Han, L. Zhang, G. Schram et al., "Properties of potassium currents in Purkinje cells of failing human hearts." *American Journal of Physiology.Heart and Circulatory Physiology* vol. 283, pp. 2495-2503. 2002.

60. J. Saiz, J. Gomis Tena, M. Montserrat et al., "Effects of the Antiarrhytmic Drug Dofetilide on Transmural Dispersion of Repolarization in Ventriculum. A Computer Modeling Study." *IEEE Transactions on Biomedical Engineering* vol. 58 no. 1, pp. 43-53. Jan. 2011.

61. M. Potse, B. Dubé, J. Richer et al., "A Comparison of Monodomain and Bidomain Reaction-Diffusion Models for Action Potential Propagation in the Human Heart." *IEEE Transactions on Biomedical Engineering* vol. 53 no. 12, pp. 2425-2435. 2006.

62. K. Simelius, J. Nenonen, R. Hren et al., "Implementation of a Conduction System in a Model of Ventricular Myocardium." *Computers in Cardiology* vol. 26, pp. 193-196. 1999.

63. R. Gilmour, J. Heger, E. Prystowsky et al., "Cellular electrophysilogic abnormalities of diseased human ventricular myocardium." *The American Journal of Cardiology* vol. 51, pp. 137-144. 1983.

64. G. Li, J. Feng, L. Yue et al., "Evidence for two components of delayed rectifier K+ current in human ventricular myocytes." *Circulation Research* vol. 78, pp. 689-696. 1996.

65. G. Li, J. Feng, L. Yue et al., "Transmural heterogeneity of action potentials and I_{to} in myocytes isolated from the human right ventricle." *American Journal of Physiology.Heart and Circulatory Physiology* vol. 275, pp. 369-377. 1998.

66. F. Lee, J. Wei, J. Wang et al., "Electromechanical properties of Purkinje fiber strands isolated from human ventricular endocardium." *The Journal of Heart and Lung Transplantation* vol. 23 no. 6, pp. 737-744. June 2004.

67. M. Gwilt, J. Arrowsmith, K. Blackburn et al., "Uk-68, 798: a novel, potent and highly selective class III antiarrhythmic agent which blocks potassium channels in cardiac cells." *The Journal of pharmacology and experimental therapeutics* vol. 256, pp. 318-324. Jan. 1991.

68. N. Iost, L. Virag, M. Opincariu et al., "Delayed rectifier potassium current in undiseased human ventricular myocytes." *Cardiovascular Research* vol. 40, pp. 508-515. 1998.

69. J. Johnson and M. Ackerman, "QTc: how long is too long?" *British Journal of Sports Medicine* vol. 43, pp. 657-662. 2009.

70. I. Goldenberg, A. Moss, and W. Zareba, "QT interval: how to measure it and what is "normal"." *Journal of Cardiovascular Electrophysiology* vol. 17 no. 3, pp. 333-336. Mar. 2006.

71. Y. Okada, S. Ogawa, T. Sadanaga et al., "Assessment of Reverse Use-Dependent Blocking Actions of Class III Antiarrhythmic Drugs by 24-Hour Holter Electrocardiography." *Journal of the American College of Cardiology* vol. 27 no. 1, pp. 84-89. Jan. 1996.

72. K. Decker, J. Heijman, J. Silva et al., "Properties and ionic mechanisms of action potential adaptation, restitution, and accommodation in canine epicardium." *American Journal of Physiology.Heart and Circulatory Physiology* vol. 296, pp. 1017-1026. 2009.